Synchrotron Based Studies of III-V Semiconductor Materials

Philip Ryan (B.Sc.)

School of Physical Sciences

Dublin City University

A thesis submitted to

for the degree of

Doctor of Philosophy

Research Supervisor

Dr. G. Hughes

March 2001

Declaration

I hereby certify that this material, which I now submit for assessment on the programme of study leading to the award of Doctor of Philosophy is entirely my own work and has not been taken from the work of others save and to the extent that such work has been cited and acknowledged within the text of my own work.

Signed: _____ ID Number: 96970405

Date: 4/4/01

Contents

Abstract

Core level photoemission spectroscopy based studies investigated the deposition of thin layers of manganese and iron on the S-terminated InP(100) surface. The sulphur treatment was carried out in vacuum with an electrochemical sulphur source. During the deposition there was strong evidence of chemical interactions between the deposited metal and the sulphur terminated surface. Both indium and phosphorous diffuses through the metal overlayer and the sulphur segregates to the top of the overlayer.

Angle resolved photoemission was employed to investigate the surface electronic structure of MOCVD and MBE grown wurtzite GaN(0001)1x1. Several discrete surface states on both materials were identified and characterised. All the states were removed by exposure of the surface to atomic hydrogen, signaling their surface localisation. Three previously unobserved surface states were identified on the MOCVD grown n-GaN, one of which was highly non-localised, dispersing throughout much of the valence band. Four states were identified on the MBE grown p-GaN surface, three of the states were of p_z orbital character, while the forth is derived from s-orbitals. Three of the surface states lie below the bulk valence band maximum throughout the surface Brillouin zone, and one surface state was observed to disperse into the bulk optical band gap. Comparison to theory suggests that this surface state is Ga-derived, consistent with a model of Ga terminated, but N polar GaN.

The bulk electronic structure of a series of $In_xGa_{1-x}N$ ($0 \leq x \leq .3$) alloys were also studied. Using linearly polarised synchrotron radiation excited soft x-ray emission and absorption spectroscopies, the occupied and unoccupied partial density of states were measured. The analysis of the N 2p derived band evolution shows a non-agreement with Vegaard's law, in contrast with previous studies of the $Al_xGa_{1-x}N$ alloy system. There is evidence that the conduction band severely broadens with increasing indium incorporation in both Ga L and N K absorption spectra. Evidence of a possible In 4d - N 2p hybridisation resonant feature is reported along with previously reported Ga 3d - N 2p hybridisation. The thermal stability of the valence and conduction bands of an $In._{11}Ga._{89}N$ crystal was investigated. Both emission and absorption spectra were found to have a temperature dependent shift in energy, but the overall definition of the spectra was unaltered even at annealing temperatures well beyond the growth temperature of the crystal.

Chapter 1

1.1 : Introduction

Semiconductors were identified as a class of materials as far back as 1826 and labeled as such in a text book by Dvigubsky [1]. Classification of the different materials was dependent on its ability to conduct electricity. The original definition of a semiconductor was those materials which fell into the category between metals and insulators. Unfortunately there were 22 orders of magnitude between the two conductivities. It was found that these materials exhibited many characteristics such as thermoelectricity, piezoelectricity, photoconductivity and a large Hall effect.

The advent of band theory which used quantum mechanics to describe the electronic structure of solids introduced the concept of discrete electronic energy levels as was previously familiar in atomic models. In the solid state, these levels may be divided into core states which are localised to each individual atom and low-lying non-localised electronic states (valence states) which share energy states from atom to atom. The valence states are broadened and may form two distinct bands with a forbidden energy gap between them. Depending on the position of the Fermi level in relation to these bands a material can be classified as an insulator, semiconductor or metal. Band theory readily explained many attributes of semiconductor materials, such as why they become more conducting with increasing temperature and why upon illumination by photons can be configured to conduct electricity.

It was of course the transistor invented by Bardeen, Schottky and Brattain in 1947 which propelled semiconductor materials into the scientific and industrial limelight. This first transistor was made of a poly-crystalline germanium sample and was not good enough to replace the vacuum tube based triodes at the time. Although by using fully crystalline material, replacing Ge with silicon and by integrating several transistors together on a single Si chip, semiconductor technology was here to stay.

Silicon was seriously established during the 1960s as the material of choice due to the ability to produce metal oxide semiconductor(MOS) structures by growing silicon oxide which was used to integrate the transistors. Silicon is still by far the most popular material in the industry with 0.13 micron technology and ultra large scale integration where millions of transistors share a single chip of several cm^2.

The fastest transistors use epitaxially strained layers of III-V semiconductors based on GaAs and InP. But the main reason they have not been used to the same extent is primarily cost and the inability to control the electronic surface characteristics. GaAs is ten times as expensive as Si and InP is a thousand times, although they have become very important in specific markets such as microwave based telecommunications [2].

Another semiconductor based device is the light emitting diode (LED). This device converts electrical current into light when electrons and holes combine across the band gap of the material. III-V s are the predominent material used due to the fact they have a direct band gap. Si on the other hand has an indirect gap. The emission of a photon is due to the relaxation of an excited electron from the conduction band to the valence band, but in Si the electron relaxes into a state which has a different momentum (k) from the relaxed hole. Thus an unassisted recombination between an electron and hole is unlikely. Phonons with high momentum and low energy can assist recombinations in such a material in the form of a three particle interaction. The electron is mobile in the conduction band and may de-excite in some other fashion such as a defect in the crystal before a phonon comes along to assist in the recombination process. Such de-excitations are called non-radiative recombinations. Indirect semiconductors have a slow response i.e they have a long carrier lifetime, and are inefficient light emitters. III-V semiconductors such as InP, GaAs and GaN based alloys, have direct band gaps. Here the carrier lifetime is far shorter, of the order of a nanosecond. Thus the electron-hole recombination happens before any defect induced de-excitation interferes. The quantum efficiency may approach 100% internally for GaAs i.e. the ratio of

radiative to total recombination [2].

The width of the gap defines the wavelength of the emitted light. GaAs for instance has a band gap of 1.31eV which emits in the infrared regime, while invisible to human eyes is well matched silicon photodetectors. GaN on the other hand has a wide band gap of 3.4eV in the near ultra violet region. The introduction of working LEDs based on GaN in 1994 certainly took the semiconductor world by surprise as most research at the time was focused on II-VI materials such as ZnSe [3]. Nitrides are not new and have been seriously studied since the 1960s. The rapid development and commercialisation of nitride based devices demonstrates how the scientific community particularly in material science works very closely with industry. The physical requirements for the next generation devices are well known although not yet accomplished but because of these close working links it is almost guaranteed that solutions will be found.

1.2 : Motivation

All three experimental chapters in some fashion were motivated by the industrial application of solid state devices. Chapter 3 discusses the deposition of thin magnetic films on InP. The application of interface technology with respect to III-V semiconductors has been a stumbling block to the progress of these materials. Thin magnetic films have also been intensely studied particularly for their application to memory technology such as GMR (Giant Magneto-Resistance). Chapter 4 investigates the surface electronic structure of clean GaN. III-nitride materials, in particular GaN have had a phenomenal impact on the optoelectronic industry since 1994 with the full scale production of commercial blue light emitting diodes. Decreasing device sizes has increased the relative importance of surface and interface effects and in some cases completely dominate the device behaviour. Within this context, both investigations of the surface electronic structure of GaN and of the chemical analysis of the Mn/ Fe : S-InP interface were undertaken. It is interesting that very

little is known about the surface structure or chemical composition of GaN despite the success of its device application.

Chapter 5 investigates the bulk electronic characteristics of InGaN, which has been successfully used as the optically active layers within multi-quantum well laser diode devices. The luminescence qualities are slowly being explained as more studies try to understand the materials successful application.

Synchrotron radiation has been a common theme throughout the thesis and reflects the increasingly important role high resolution techniques have in modern material characterisation studies. Its wide ranging ability to be used as a probe of both bulk and surface electronic structures and surface chemical composition as illustrated in the work presented in this thesis indicates its importance in the future of material science.

1.3 : Thesis Layout

The thesis has three main experimental chapters(3-5) and each of these chapters was written to be somewhat 'stand alone'. Prior to these, chapter 2 discusses the background theory of the primary techniques used throughout the thesis.

While several experimental techniques are used, the most relevant have been low energy electron diffraction, LEED, used to indicate the surface structure, core level and angle resolved photoemission to study the surface chemical bonding and the surface electronic structure and finally soft x-ray emission and absorption spectroscopies, XES and XAS, to investigate bulk electronic structures of solids.

Chapter 3, presents a surface chemical analysis of the deposition of transition metals, Mn and Fe on S terminated InP(100) using core level photoemission spectroscopy. Chapter 4 investigates the surface electronic band structure of clean GaN(0001) using angle resolved photoemission. And chapter 5 investigates the occupied and unoccupied bulk band structure of the InGaN ternary alloy using both XES and XAS.

Chapter 6 brings the thesis to a close by briefly discussing some after-thoughts of the experimental results.

1.4 : References

1. Levinshtein, M.E. and G.S. Simin, *Getting to know Semiconductors*. 1992, Singapore: World Scientific.
2. O'Donnell, K.P., *Beyond silicon : the rise of compound semiconductors*, in *Group III Nitride Semiconductor Compounds*, B. Gil, Editor. 1998, Oxford Science Publications.
3. Nakamura, S. and G. Fasol, *The Blue LED*. 1997, Berlin-Heidelberg: Springer.

CHAPTER 2

Review of Experimental Techniques

2.1 : Introduction

Studies of surface and bulk electronic structure of wide band gap nitrides and the chemical interactions of transition metal deposition on S terminated InP are discussed within the thesis. Core level and angle resolved photoemission studies provide information on the surface chemical composition and the surface electronic structure respectively, while x-ray emission and absorption spectroscopies probed the bulk electronic structure of both occupied and unoccupied states. Low energy electron diffraction (LEED) provides information on the surface structure. Valence band photoemission studies can be used to investigate the low binding energy valence band states, and angle resolved photoemission has the ability to map the materials electronic structure. Chapter 4 discusses the surface electronic structure of GaN and LEED is used to orient the sample along the symmetry lines.

To investigate the bulk electronic structure of InGaN, both soft x-ray emission and absorption techniques were employed. Due to the x-ray based nature of these techniques they are bulk sensitive, and do not require the extreme surface cleanliness that is necessary for high quality photoemission studies, nevertheless because they use very soft x-rays, the experiment still requires high vacuum conditions.

2.2 : Surface Reconstructions

The translational invariance of a bulk crystal is removed at the surface and the net resulting force on the surface atoms is normally into the crystal. A relaxation of the surface plane occurs in order to obtain an equilibrium. This relaxation can result in a reconstruction of the surface atoms occurring with structures often more complex than the ideal surface

termination.

At the surface, assuming a clean flat 2-D terminating layer, and therefore a 2-D periodic structure, every lattice point can be labeled from an origin by translation vectors: $T = ma_s + nb_s$, with n and m integers and a_s and b_s the crystal primitive vectors defining a mesh or surface net. Ideal or relaxed surfaces are noted by the periodicity and orientation of the surface structure as being the same as the bulk, and are denoted as 1x1 structures. If the primitive translation vectors differ from the ideal surface, so that a_s=Za and b_s=Yb, thus indicating a reconstructed surface, then the surface structure will be noted as a ZxY surface reconstruction. If the surface net is rotated by an angle θ, then the angle is also noted ZxY-θ.

2.3 : 'Universal Curve'

Figure 2.1 shows the mean free path of electrons in a solid as a function of electron energy above the Fermi level. The escape depth is determined by electron-electron and electron-phonon interactions, generally electron-phonon scattering plays a role only at lower energies. Above ~10eV collective oscillation (plasmon) losses lead to a decrease in the mean free path, with a minimum around 50eV. It is noted that most materials do not stray too far from the universal curve, and this can be explained by the fact that the dominant electron energy loss mechanism in solids is the excitation of valence band electrons. The electron density in the valence band is similar for most elements, about 0.25 electron $Å^{-3}$ [1]. With this density used to calculate the mean free path of electrons in a solid using the free electron gas theory (dashed line in figure 2.1) the result as shown compares well to the experimental results [1-3].

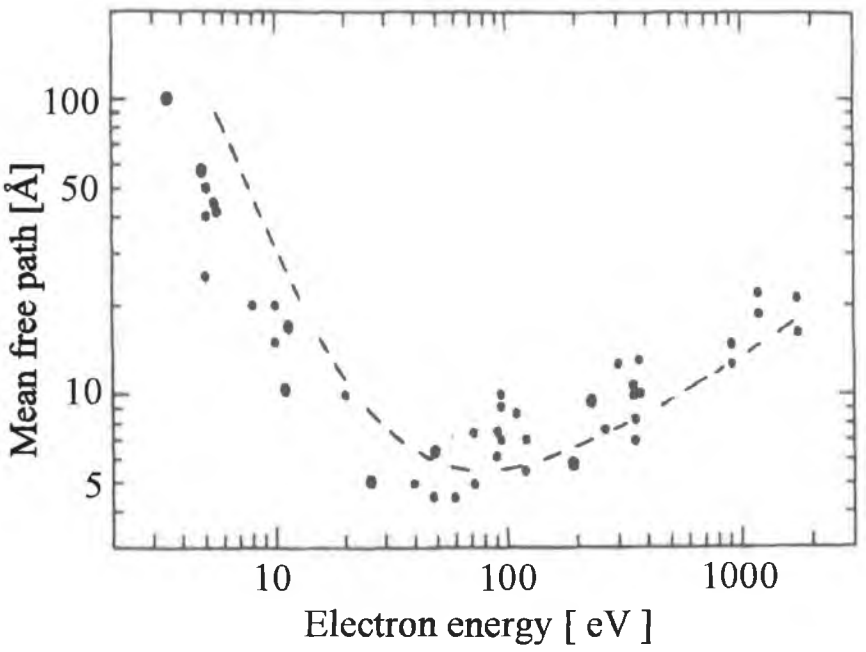

Figure 2.1 : The Universal Curve shows the electron inelastic mean free path in solids as a function of the electrons energy. (Measured with respect to the fermi level). The dashed line indicates a Golden Rule calculation of the inelastic mean free path of electrons [1].

2.4 : Low energy electron diffraction (LEED)

In order to investigate the surface structure, to reproduce well known clean surface structures or to orient samples along certain symmetry lines for angle resolved photoemission, LEED was the technique of choice. X-ray diffraction is the most used technique in understanding the atomic structures of crystalline solids, but because of the low cross-section between x-rays and matter, it is inherently a bulk sensitive probe. To investigate the surface atomic structure of crystalline solids, an electron based diffraction is needed. The de Broglie wavelength of an electron with kinetic energy of 150eV is of the order of 1Å which is comparable to typical interatomic spacings. This kinetic energy is close

to the minimum of the Universal Curve, i.e. a very short probing depth and is thus very surface sensitive having a penetration depth of < 10Å.

The extreme surface sensitive nature of electrons with energy ranges of 50eV-500eV is described by the Universal Curve. Using these electrons as a probe for a surface diffraction experiment will result in a Fraunhofer diffraction pattern from the elastically backscattered electrons. This pattern will be the Fourier transform of the surface atomic structure. The first experiment to investigate the wave nature of the electron was performed by Davisson and Germer [4].

The LEED optics are shown by figure 2.2. The LEED pattern is an image of the surface 'reciprocal' net when viewed along the surface normal at a relatively long distance from the crystal. The distance between adjacent points in a reciprocal lattice is inversely proportional to the distance between the atomic planes. The periodic distance perpendicular to the surface, in the z-direction may be considered to be infinite. The reciprocal lattice points will then be infinitely dense and may be said to form rods in reciprocal space. 2-D translational invariance holds that diffraction will occur if the 2-D Laue conditions are satisfied :

$$(1) \qquad (k_i - k_f)\cdot a_s = 2\pi m \qquad \text{and} \qquad (k_i - k_f)\cdot b_s = 2\pi n$$

where k_i and k_f are the wave vectors of the incident and scattered electron and m and n are integers. Figure 2.3 illustrates the Laue conditions using an Ewald sphere construction. A reciprocal lattice 'rod' passes through every point of the surface reciprocal net, $g_s = hA_s + kB_s$, where h and k are the Miller indices and the general reciprocal lattice vector g_s lies in the plane of the surface. The diffraction is satisfied for every beam the direction of which coincides with the intersection between the Ewald sphere and a reciprocal rod. The diffraction spots are normally labeled by the Millar indices (hk) causing it.

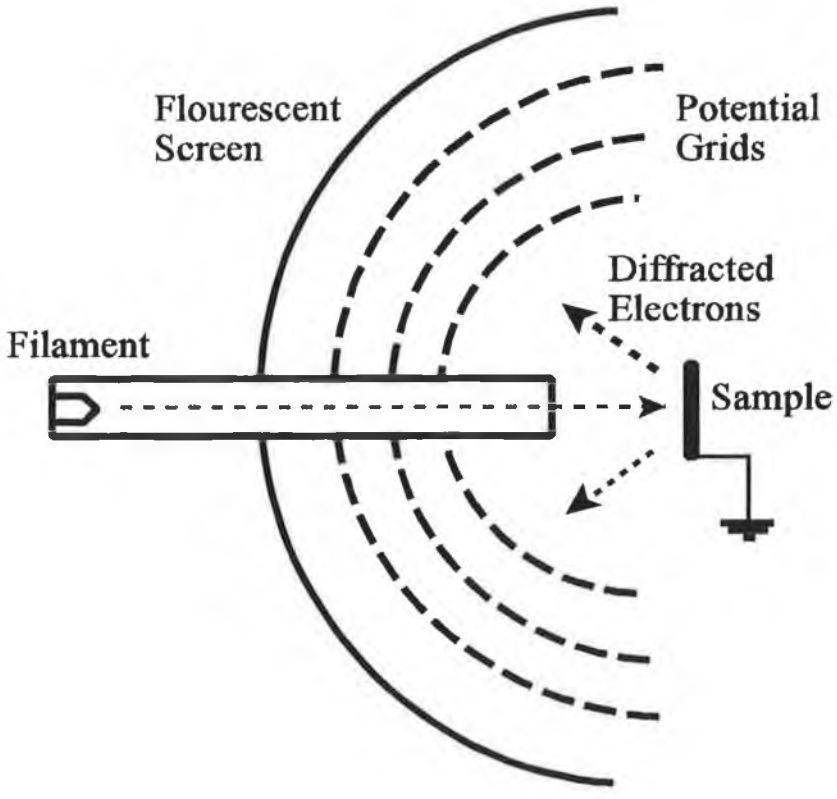

Figure 2.2 : Low energy electron diffraction optics to produce a diffraction pattern. The filament emits a large number of electrons which are accelerated to energies from 50eV to 1000eV. The beam is focused onto the sample, which is placed at the common focal point of the spherical potential grids and flourescent screen.

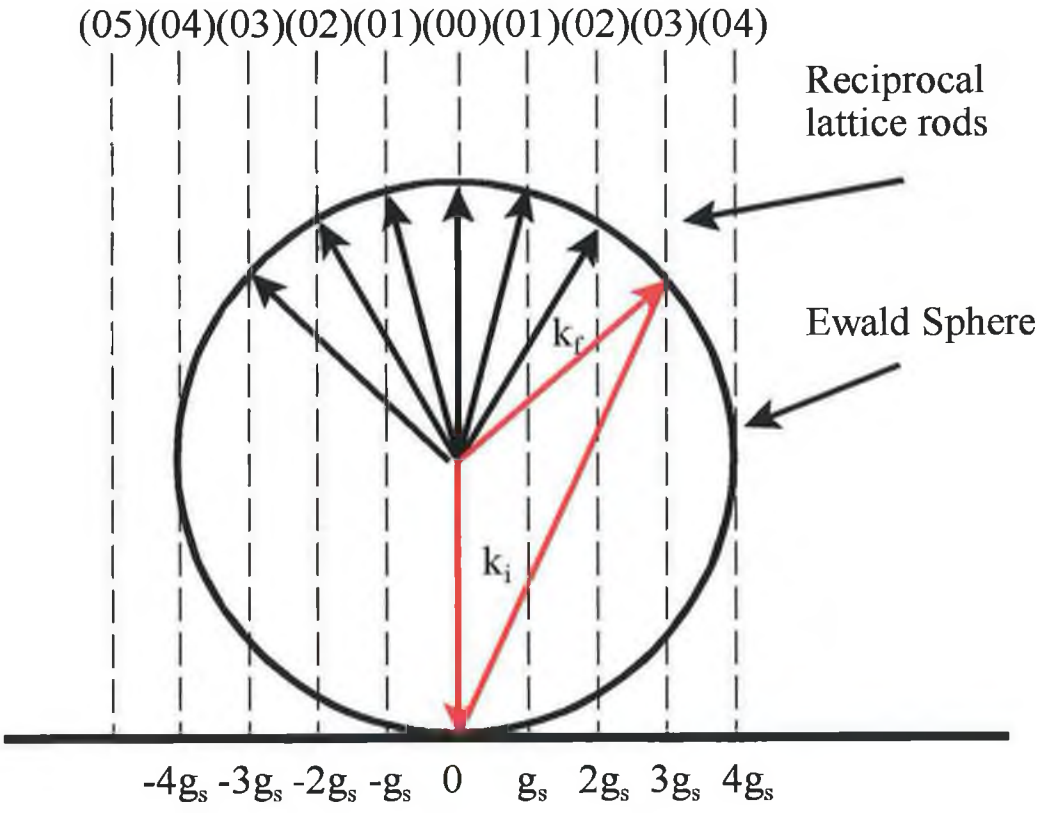

Figure 2.3 :An Ewald sphere construction, showing several reflected beams generated by an incident wavevector k_i and where k_f is a typically scattered electron. The diagram only shows reflected beams and within plane diffracted electrons.

2.5 : Photoemission

While the first documented evidence of what became known as the 'photoelectric effect' was reported by Hertz [5], in 1887, it was not until 1905, that Einstein [6] explained the emitted electron velocity dependence on the frequency of the incident light with the simple relationship

$$(2) \qquad E_{kin} = h\nu - \phi,$$

The maximum kinetic energy (E_{kin}), of a photoemitted electron is equal to a 'quantum' of energy $h\nu$, related to the classical frequency of the incident light, minus the work-function energy ϕ which is defined as the minimum energy necessary to emit an electron from a solid.

The single particle approximation may for most cases be used to interpret photoemission spectra. This model is a natural extension of Einstein's equation so that all emitted electrons may be described.

$$(3) \qquad E_{kin} = h\nu - \phi - E_i ,$$

such that the energy of the incident photon is completely transferred to a single electron with a binding energy of (E_i).

The transfer of the incident energy $h\nu$ to electrons allowing some to escape the solid into the vacuum, where their kinetic energy is measured by a detector to form an observable spectrum. This excitation requires a transition from an occupied 'state' below the Fermi level E_F to an unoccupied state above the vacuum level. Therefore the number of possible transitions depends on the 'density' of these respective states. The fine structure of photoemission spectra reveal information about the product of the 'initial' and 'final' density of the states of the solid under investigation. This is illustrated in figure 2.4 where the shallow states are indicated by the valence band and the deeper core level states are indicated by the core level states.

An important characteristic of the photoemission process is its surface sensitivity.

While the wavelength of incident light may penetrate several tens of atomic layers, because of multiple scattering of photoexcited electrons, only those electrons close to the surface will be elastically emitted. The energy dependence of the escape depth of the excited electrons is described by the 'Universal Curve', as previously discussed.

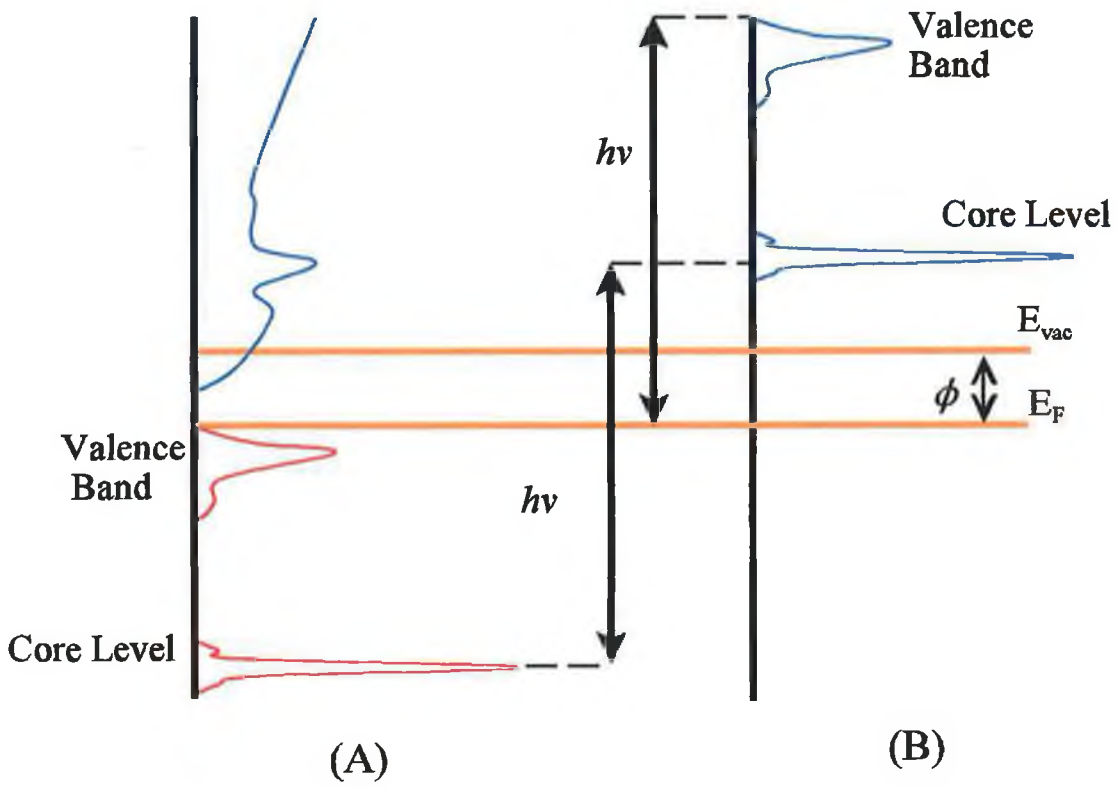

Figure 2.4 : Illustration of how the distribution of electronic states within the sample (A) is reflected in the photoemission spectral fine structure. (B) The gap in the distribution of the energy states straddling the E_F indicate this example is a semiconductor.

X-ray and UV photo-electron Spectroscopy,(XPS and UPS), are widely used to obtain characteristic electron structure of solids. Excitation processes which contribute features in the photoemission spectrum are illustrated in figure 2.5.

Emitted electrons originate from three main separate processes. Core level spectral features occur as a direct optical excitation from highly localised core shells and broad valence band features from highly de-localised valence band states. These regimes define the differences between XPS, used to investigate core electronic levels and UPS, which is used to probe the valence states. The development of synchrotron radiation based photoemission has succeeded in bridging these traditional regimes, but the terms are still used.

The removal of an electron from an inner shell results in a strong 'perturbation' of the remaining 'ionic levels', which relax to screen the core-hole. The energy gain from this relaxation process is absorbed by the photoemitted electron, which will show a higher kinetic energy than predicted by Einstein's equation. The shift is referred to as the 'intra-atomic relaxation shift'. The creation of the hole happens much faster than the relaxation process, thus the emission of an electron from an atom leaves the atom in an excited state, this effect creates 'satellite' features corresponding to these excited states of the atom.

Valence band states also react to changes in atomic potentials. The difference here is they react collectively and appear as loss peaks due to collective electron oscillations or 'plasmons'. This 'extra-atomic relaxation' contributes to the overall core-level spectral shape. The emitted electrons also affect the equilibrium valence charge density as they leave the solid and thus suffer additional bulk and surface plasmon energy losses, these effects are often referred to as 'extrinsic' processes as to distinguish from the previous 'intrinsic' processes. Figure 2.6 illustrates a plasmon loss series from the Al 2s core level [7].

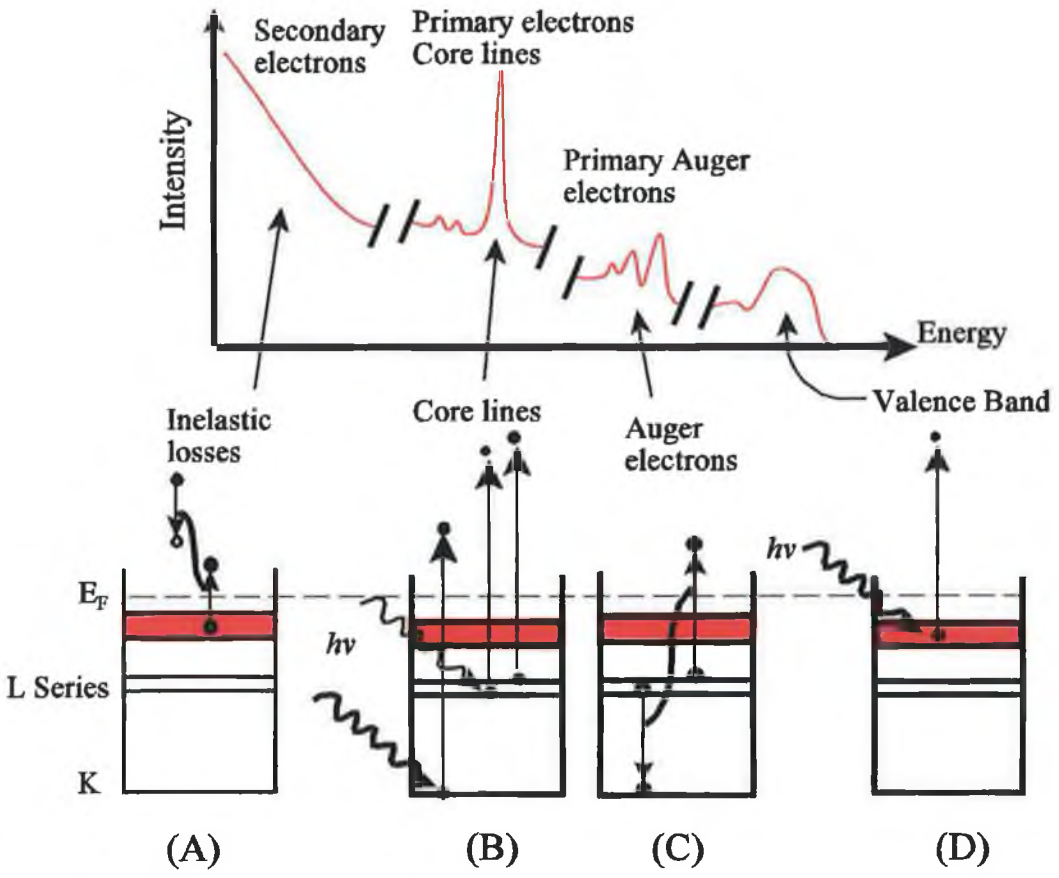

Figure 2.5 : Several processes contribute to a photoemission spectrum. B :The direct optical excitation of core electrons, C : Auger electrons from hole de-excitations, D : direct photoexcitation of valence electrons and A : inelastic losses giving rise to secondary electrons and plasmon satellites [2].

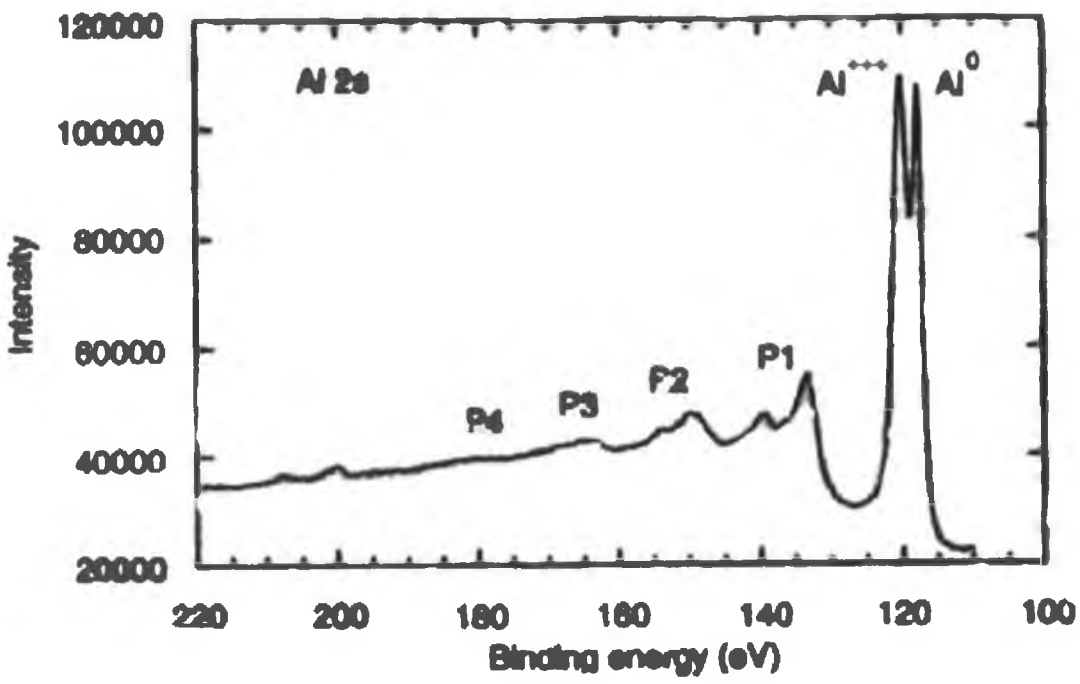

Figure 2.6 : The emitting photoelectron may couple with plasmon vibrations leading to periodic losses. This spectrum from Vickerman [7], shows an example of a plasmon loss series for Al 2s.

The binding energy of the core level electrons may be modified by the local bonding environment of the atoms. This feature is used extensively, to supply surface chemical analysis (chapter 3). Once an electron is emitted leaving a core hole state, this may be reoccupied either by a radiative de-excitation, producing x-ray emission or by a non-radiative Auger process. X-ray emission and absorption will be dealt with in later sections. The Auger process shows a relatively broad spectral structure and is the dominant de-excitation mechanism for elements lighter than Z ≈35 [1]. It is also element specific and surface sensitive. The process is the basis of Auger electron spectroscopy (AES), this technique was used in the studies presented within the thesis to identify surface contaminants, most typically carbon and oxygen.

Electrons emitted from the valence band are not significantly perturbed by holes created within the valence band. The mobility of these holes is greatly increased due to the de-localised nature of its wavefunction. A valence band hole state can be generated either from direct photoemission 'primary' or by 'secondary' electron emission. In the latter process electrons which reach unoccupied states above the vacuum level within the solid, may loose their energy by scattering off other electrons in the valence states producing electron - hole pairs. These inelastic 'secondary' electrons contribute to the high intensity, broad emission feature at low kinetic energies, and relate to the distribution of unfilled states located above the vacuum level of the solid.

2.6 : Photoemission Theory

Models to describe photoemission are generally divided into microscopic and phenomenological theories, i.e. the one step and three step models respectively.

The beginning to all calculations start with Fermi's Golden Rule, which expresses the total photoelectric current with respect to the square of the 'perturbation matrix element' $\langle\psi_f|\, H' \,|\, \psi_i\rangle$ where H' is the interaction of the electron with the incident photon, $|\psi_i\rangle$ and $|\psi_f\rangle$ are the initial and final states of the photoemission process. Fermi' Golden rule describes the transition probability per unit time between the initial and final states of an N electron system if the perturbation H' is small,

$$(4) \qquad \frac{d\omega}{dt} = \frac{2\pi}{\hbar}\left|\langle\psi_f|H'|\psi_i\rangle^2\right|\delta(E_f - E_i - h\nu)$$

where $h\upsilon$ is the incident photon energy, and E_i and E_f are the initial and final energies of the N-electron states respectively. The Hamiltonian H' for the interaction between an electron and a photon with several assumptions may be given by:

$$(5) \qquad H' = \frac{1}{2mc}\left(A.p + p.A\right)$$

where A is the vector potential of the incident light and p is the momentum operator of the electron.

2.6.1 : The one step Model

Many microscopic theories of photoemission within the one step model have been formulated such as the steady state scattering and response theory, Green function methods and multiple scattering or dynamic approaches. Mahan [8] uses the steady state scattering theory, which is applied to the many body scattering processes that the photoexcited electron experiences before it leaves the solid. The surface crossing effect was calculated by assuming the free electron gas theory for the electrons in the solid and using a step potential across the surface barrier. The steady state scattering theory is reviewed by Schiach [9].

These calculation techniques may be termed as static, where stationary Bloch initial and final electron states are used. The alternative 'dynamic approach' [10-13], where multiple scattering effects are properly included for both initial and final state electron wave-functions. While several versions were developed, Pendry' single 'dynamic' theory includes the important elements for photoemission, such as band structure, surface effects, and scattering of the outgoing wave. A more fully developed dynamic one step single particle theory of photoemission [14], extends Pendry' method by including relativistic effects to account for the spin-orbit interactions. The details of one step models are beyond the scope of the thesis, although the basic concepts are introduced here.

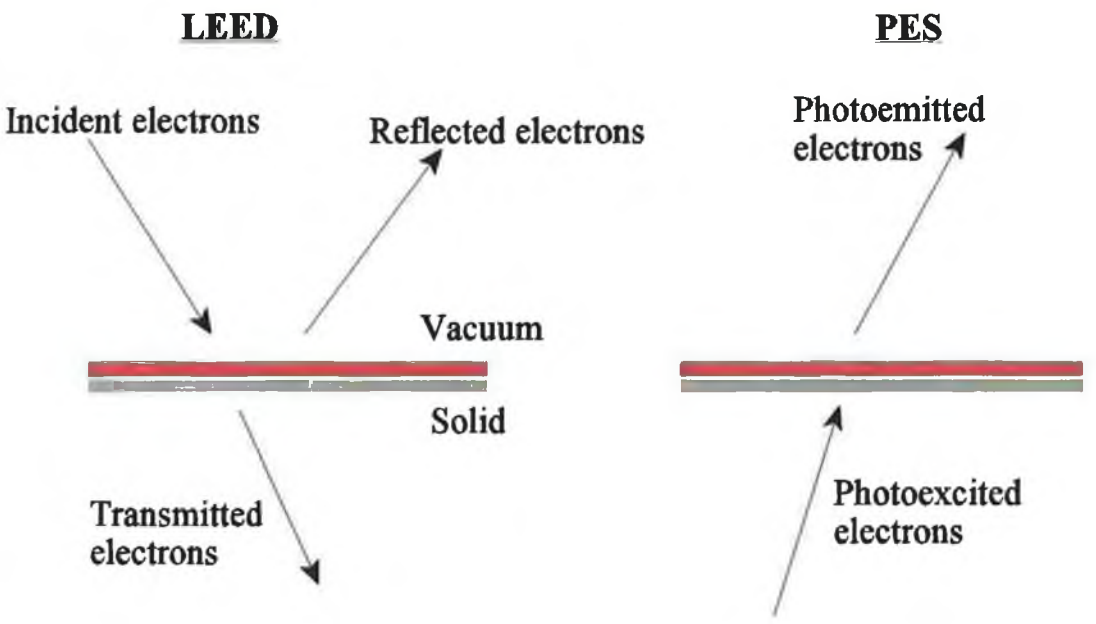

Figure 2.7 : Illustrates the 'asymptotic' form of the wavefunction within the LEED and PES processes. In LEED there are incoming, reflected and transmitted beams, and in photoemission only incoming and transmitted-time reversed beams.

The Golden Rule of equation (4) is in principle the correct one-step treatment for photoemission although, in this form it cannot be solved rigorously. Calculation procedures generally split the problem into a surface and bulk part. The surface will affect the initial and final wave-functions $|\psi_i\rangle$ and $|\psi_f\rangle$ by introducing new surface states and resonances [1]. This effect requires the continuity of the wave functions through the surface boundary. The problem of wave-function matching at the surface is the same as that involved in the theory of LEED [15]. Within the LEED process the incident electron beam produces transmitted and reflected beams, whereas in photoemission only 'time reversed' transmitted and incident beams occur as illustrated in figure 2.7. Thus, often the final state in Fermi's Golden Rule matrix element is referred to as a time-reversed LEED state. The total photocurrent is then written as a sum of the surface and undisturbed bulk photocurrents and is therefore in practice, a two step model [1].

2.6.2 : Three Step Model

Due to the cumbersome nature of the one step model calculations, a more practical model is usually employed to interpret photoemission results, i.e. the phenomenological three step model. The three steps describing the photoemission process include the optical excitation of the electron in the solid, transport of the electron to the surface and the crossing of the surface boundary to the vacuum [3]. Optical excitation occurs with the absorption of the incident photons. If the momentum of the photon is neglected we then have a direct (momentum conserving) transition in the reduced zone scheme, described by the free electron final state model in figure 2.8. The model uses the energy dispersion of a free electron to estimate the final state bands within photoemission. The model is based on the assumption that the crystal potential effect on final states with sufficiently high energy is small so that the photoelectron in the crystal can be treated as a free electron in a typical potential well.

The internal energy distribution of the photoexcited electrons $N_{int}(E_{kin},h\upsilon)$ is given by [16],

$$N_{int}(E_{kin},h\nu) \propto \sum_{f,i} d^3k|M_{fi}|^2\delta(E_f(k)-E_i(k)-h\nu)\delta(E_{kin}-E_f(k)+\phi) \qquad (6)$$

where E_{kin} is with respect to the vacuum level. M_{fi} is the transition matrix element of the interaction Hamiltonian H' as given,

$$M_{fi} = \langle f,k|H'|i,k\rangle \qquad (7)$$

and $|f,k\rangle$ and $|i,k\rangle$ are taken as Bloch states of the initial and final bands inside the crystal. $E_i(k)$ and $E_f(k)$ denote their respective wave vector energies within the reduced zone scheme. The first delta function imposes energy and k-conservation for the direct transition, $E_f(k)- E_i(k) = h\upsilon$. The second delta function ensures that the measured kinetic energy of the

photoemitted electron equals the final state energy inside the solid minus the work function(ϕ).

The second step, describing the electronic transport to the surface, deals with the scattering of the electrons both by phonons and other electrons. Electron-electron inelastic scattering inhibits the vast majority of electrons from reaching the surface, unless the electron energy is very close to the threshold where phonons dominate. Assuming the scattering frequency, given by $1/\tau$, where τ is the photoelectron lifetime, is isotropic and only depends on its kinetic energy, the electron inelastic mean free path, $\lambda(E,k)$ is given by,

$$(8) \qquad \lambda(E_{kin}, k) = \tau v_g = \frac{\tau}{\hbar}\frac{dE_{kin}}{dk}$$

where v_g is the group velocity in the final state. A transport coefficient $D(E_{kin},k)$[17], describing the fraction of the total number of photoelectrons created within the mean free length from the surface is written as :

$$(9) \qquad D(E_{kin}, k) \approx \frac{\alpha\lambda}{1+\alpha\lambda}$$

where α is the optical absorption coefficient of the light, (α^{-1} indicates the penetration depth of the incident light). 'D' is primarily that fraction of escaped electrons which were not involved with scattering.

Figure 2.1 showed the universal curve which depicts the mean free path of electron as a function of their energy. The region of strong damping where the mean free path is at a minimum indicates where photoemission is most surface sensitive, and the ability to tune the photon energy of synchrotron radiation means that the kinetic energies may be selected so as to obtain the highest surface sensitivity.

The final step describes the emission process of the electrons from the solid. For electrons to cross the surface, they must have sufficient momentum normal to the surface to overcome the surface potential barrier, otherwise they will be reflected from the surface back into the bulk. Within the crystal the electron travels in a potential of E_{vac}- Eo, as shown in figure 2.8. To escape the solid the electrons must satisfy,

$$(10) \quad (\hbar^2/2m)\, K_{\perp}^2 \geq E_{vac} - Eo,$$

where Eo is the energy of the bottom of the valence band and $K_{\perp}$ is the component of the wavevector of the excited electron K normal to the surface. The transmission of the electron through the surface into the vacuum leaves the parallel component of the wave vector conserved, as illustrated in figure 2.9 and 2.10, such that

$$(11) \quad p_{//}/\hbar = K_{//} = k_{//} + G_{//}$$

where p is the electron momentum in the vacuum, and $K_{//}$ is the parallel component of the wavevector K of the photoelectron. In the free electron model, the excited electrons simply reflect Snell's law,

$$(12)\ k_{f//} = \sin\theta\left(\frac{2m}{\hbar^2}E_{kin}\right)^{1/2} = \sin\theta'\left(\frac{2m}{\hbar^2}(E_f - E_0)\right)^{1/2}$$

where θ represents the angle outside the crystal and θ' is the angle within the crystal, both with respect to the surface normal.

Equation (12) indicates that the electron emission makes a larger angle than the impinging angle within the crystal. Therefore for every final state energy there is a maximum angle $\theta'_{max} < 2\pi$ inside the sample that can cross the surface.

$$(13) \qquad \sin\theta'_{max} = \left(\frac{E_{kin}}{E_f - E_o}\right)^{1/2}.$$

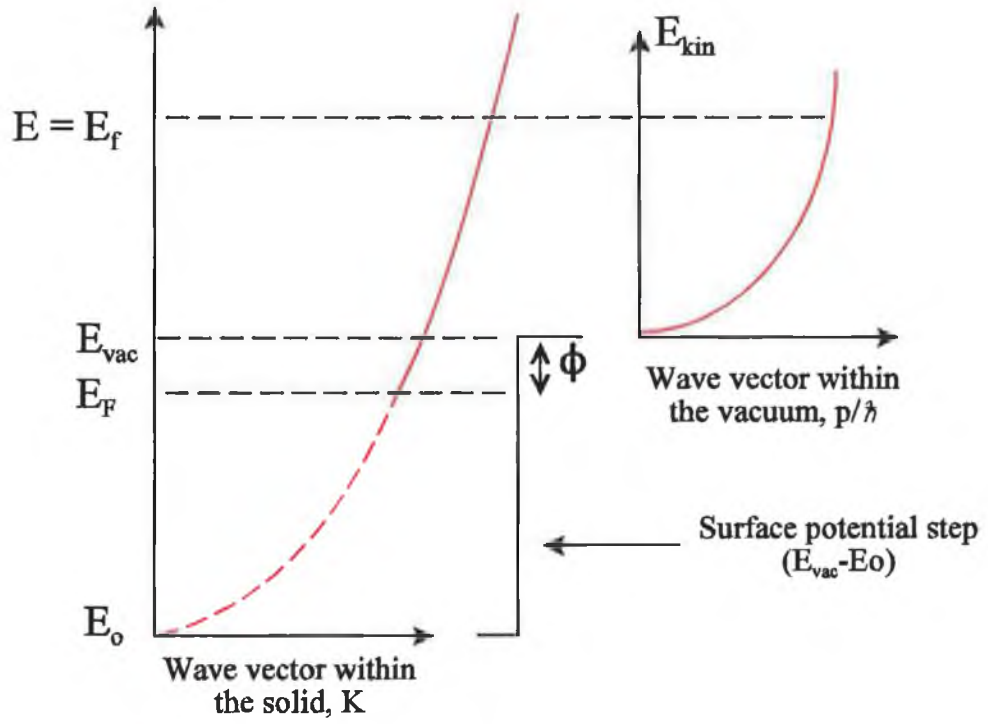

Figure 2.8 : The free electron final state model for the photoemission process. Within the crystal the final state wave vector is determined by the intersection of a free electron parabola with a minimum at Eo, at the bottom of the valence band, and the final state energy, E_f [3].

This angular region $\theta' \leq \theta'$max is called the 'escape cone', as is illustrated in figure 2.9. The kinetic energy of the photoemitted electron is determined by,

$$(14) \quad E_{kin} = \frac{\hbar^2}{2m}\left[K_{//}^2 + \left(\frac{p_\perp}{\hbar}\right)^2\right] = E_f(k) - E_{vac},$$

where $p_\perp/\hbar$ is the perpendicular component of the electron wave vector in the vacuum.

The perpendicular component of the wave vector inside the crystal $K_\perp$ remains undetermined. The free electron final state model coupled with a surface step function is not accurate enough to determine $K_\perp$.

The final state wave function $|f,k\rangle$ within the solid is not a single plane wave but is represented by a Bloch wave comprising of a number of plane wave contributions with a number of reciprocal lattice vectors,

$$(15) \quad |f,k\rangle = \sum_G u_f(k,G)e^{i(k+G).r},$$

where u_f possesses the periodicity of the lattice. Each component may be matched to a free electron plane wave outside the solid therefore the photoemitted electrons can emerge from the crystal in a number of possible directions determined by equations 11 and 12.

The plane wave components of a single Bloch wave of energy E with the same value of $k_{//} + G_{//}$ leave the crystal in the same direction and are treated coherently. The total transmission factor $|T(E_f,k_{//})|^2$, for such a $(k_{//}+G_{//})$ beam at a particular final state energy E_f, across the surface is written as the sum of the transmission factors for each plane wave $|t(E_f,k_{//})|^2$ $|u_f(G,k)|^2$ moving towards the surface i.e. $(K+G)_\perp > 0$, as

$$(16) \quad |T(E_f,k_{//})|^2 = |t(E_f,K_{//})|^2 \left| \sum_{(k+G)\perp>0} u_f(k,G) \right|^2,$$

where $t(E_f,k_{//})$ uses the following criteria whether the final state energy is greater than the vacuum level:

$$(17) \quad t(E_f,k_{//}) = \begin{cases} 1 \text{ if } E_f(k) > E_{vac} \\ 0 \text{ if } E_f(k) \le E_{vac} \end{cases}$$

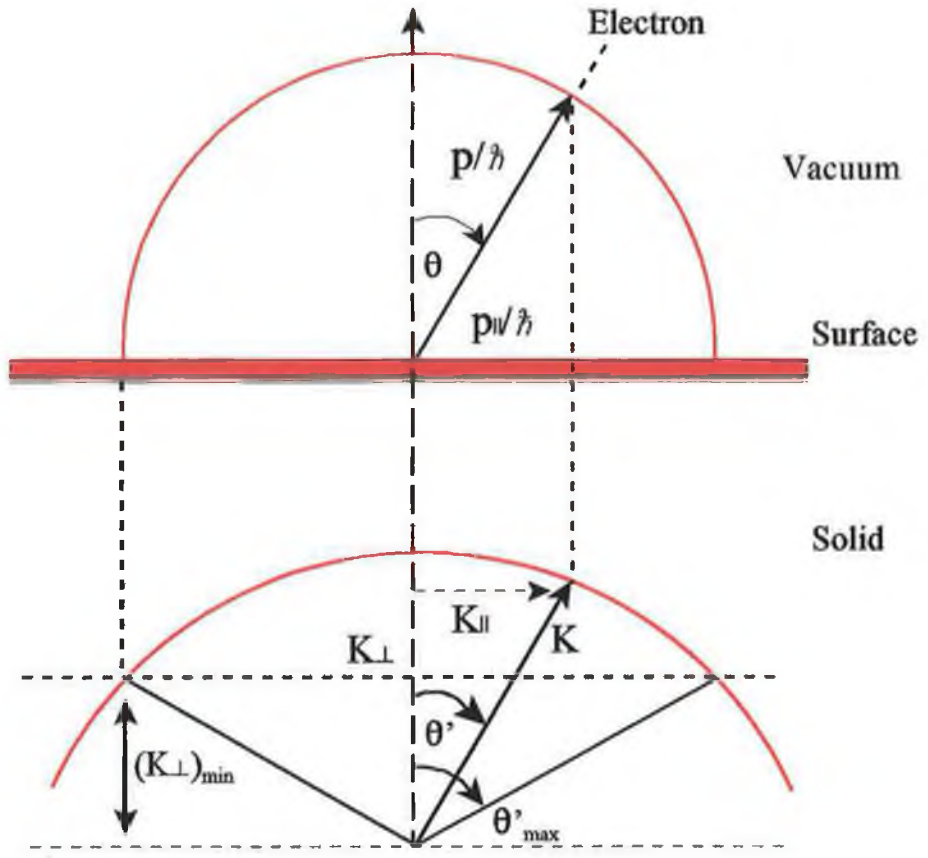

Figure 2.9 : The escape condition within the free electron final state model. The two red solid curves indicate the internal and external escape cones for the photoexcited electrons with momentum K and p/ħ respectively [3].

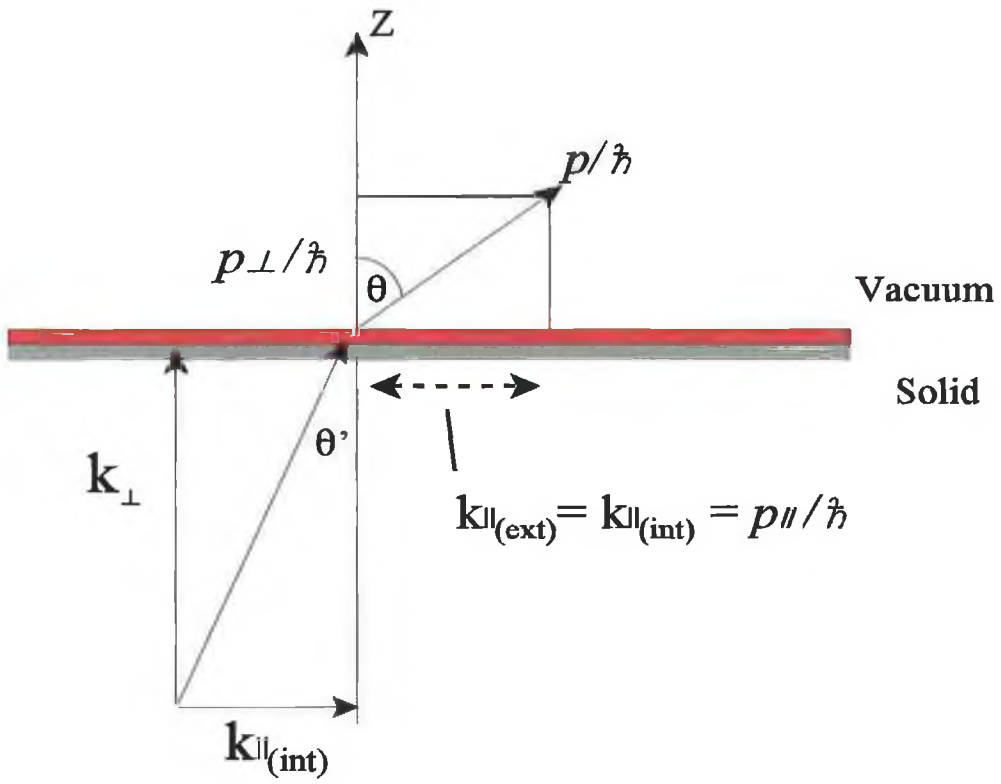

Figure 2.10 : The photoelectron emitted from the solid is refracted by the surface potential step. The parallel component of the momentum is conserved during the transition, but the perpendicular component is not conserved due to the loss of crystal periodicity along the surface normal [3].

Putting the three steps together the final expression for a fully angle resolved photoelectron energy spectrum from the bulk is given by :

$$N(E_{kin}, K_{//}, h\nu) \propto \sum_{f,i} \int d^3k |M_{fi}|^2 D(E_{kin}, k) \left| T(E_f, k_{//}) \right|^2 x$$

$$\delta(E_f(k) - E_i(k) - h\nu)\delta(E_{kin} - E_f(k) + \phi)\delta(k + G - K)\delta\left(K_{//} - \frac{p_{//}(\vartheta, \phi)}{\hbar} \right) \quad (18)$$

where $\delta(k + G - K)$ indicates the momentum conservation for direct transitions in the extended zone scheme, and $\delta(k_{//} - p_{//}(\theta,\phi)/\hbar)$ gives the conservation of the parallel components of the photoelectron momentum across the crystal surface.

2.6.3 : Angle Resolved Photoemission (ARP)

The optical transition that occurs between an initial state $E_i(k_i)$ and a final state $E_f(k_f)$ conserves both energy and momentum within the solid,

$$E_f = E_i + hv, \qquad (19)$$

and

$$k_f = k_i + G \qquad (20)$$

where G is the bulk reciprocal lattice vector. In the reduced zone scheme the bands outside the first Brillouin zone are folded back onto the first Brilloiun zone by adding an appropriate G. Within this model every transition is a 'direct' transition. The direct transition is depicted as vertical because $k_f = k_i = k$, where k denotes the wave vector of the crystal states within the first Brillouin zone, as depicted in figure 2.11. As mentioned, the photoelectron in the crystal is treated as a free electron in a typical potential well, V_s. The final state energy is then given by the free-electron parabola with an inner potential, $V_0 = e V_s$:

$$E_f(k) = \frac{\hbar^2}{2m}(k+G)^2 - V_0 \qquad (21)$$

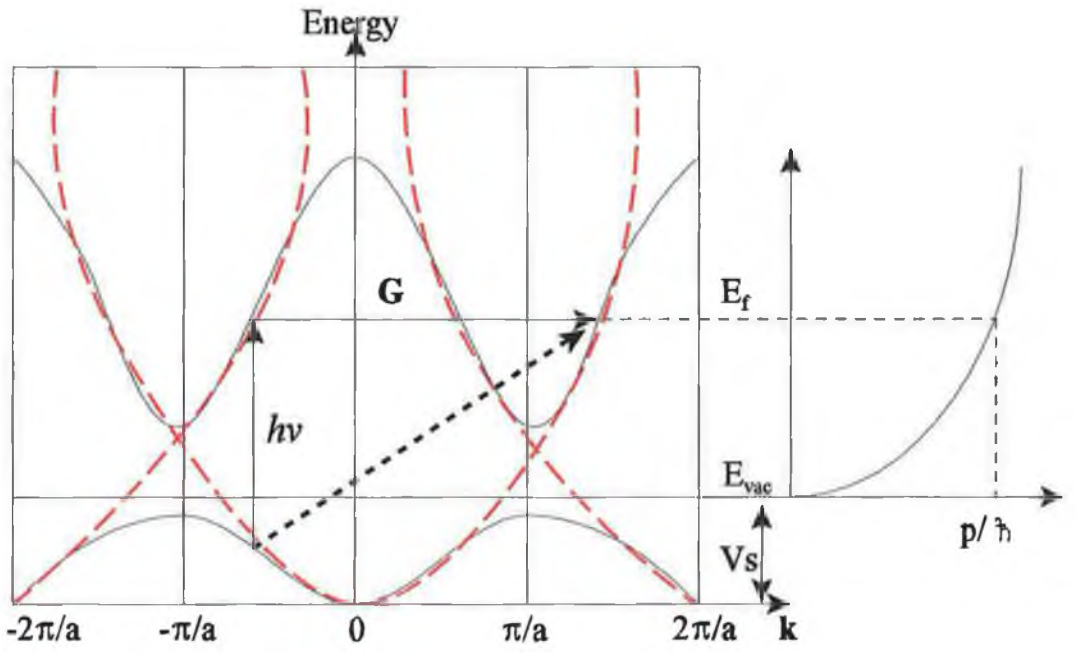

Figure 2.11 : Illustrating a direct transition within the free electron final state model. A non vertical transition in the extended zone scheme is represented as a vertical transition in the reduced zone scheme with the aid of a bulk reciprocal lattice vector G. The final state of the electron within the photoemission process may be approximated by a free electron parabola with a zero reference at the bottom of the valence band. The wave vector of the photoelectron in vacuum is given by the intersection of the free electron parabola and the final state energy E_f [3].

The inner potential of the material is required to fully determine momentum dispersion of the photoemitted electrons. Several techniques have been devised but the most common technique is to compare experimental results with theoretical band structure [3].

The angle resolved photoemission experiment is conducted by measuring the energy distribution of the photoelectrons emitted at a polar angle θ within a selected crystal plane defined by an azimuthal angle ϕ, as illustrated in figure 2.12. Within the reduced zone scheme, the conservation relations is expressed as :

(22) $E_f(k) - E_i(k) - h\nu = 0,$

which describes both energy surfaces $E_f(k)$ and $E_i(k)$ within k-space between which 'vertical' transitions are connected by $h\nu$.

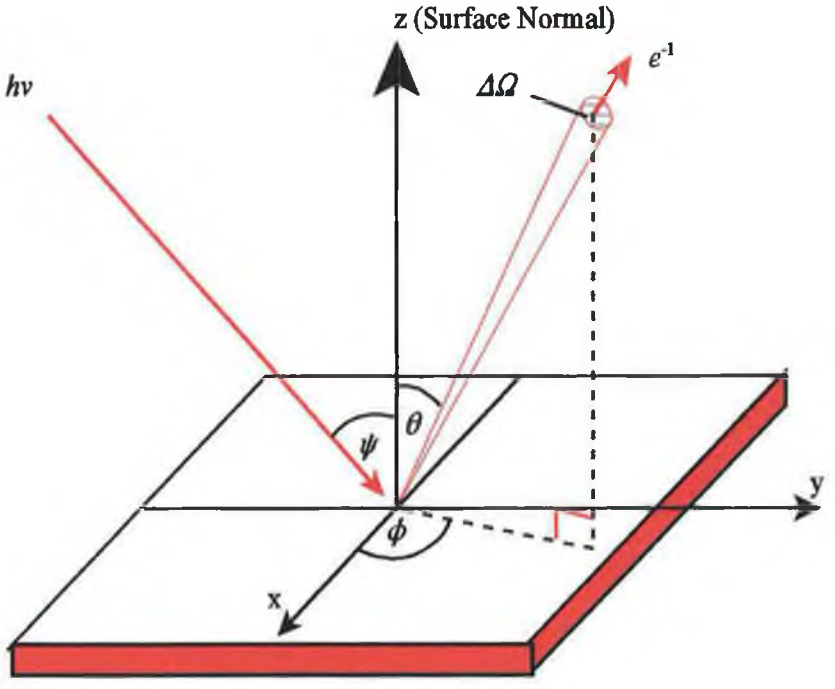

Figure 2.12 : Schematic illustration of a typical angle resolved photoemission experiment. The incident photons of energy hv impinge on the surface at an angle ψ to the surface normal and the photoexcited electrons emitted at an azimuthal angle ϕ and polar angle θ are detected by an electron analyser over an acceptance aperture ΔΩ.

Once the photoelectrons have escaped the solid they are detected as free electrons whose component of momentum parallel to the surface is given by,

(23) $$p_{//} = \sqrt{2mE_{kin}}\sin\theta\ ,$$

where θ is the emission angle of the detected photoelectron with respect to the surface normal and E_{kin} is the kinetic energy measured with respect to the vacuum level of the

spectrometer. The conservation of the parallel component of the momentum of the photoelectron crossing a well ordered surface is illustrated in figure 2.10.

2.6.4 : Parity Selection Rules

Electronic states may be assigned either odd or even symmetries depending on the reflection of the respective wave function across a specific mirror plane, therefore the symmetry of specific states may be determined. The transition operator of Fermi's Golden Rule equation, $\langle \psi_f | A.p | \psi_i \rangle$, determines both the photo cross-section intensity and the symmetry of the probed states, where A is the external vector potential of the photon, and p is the momentum operator of the orbital electron.

Figure 2.13 shows a typical angle resolved photoemission geometry and showing polarisation orientation of the incident photon vector, A, parallel to the plane of reflection, (y-z), which forms a mirror plane normal to the surface. It is possible to classify all electronic states as either even or odd with respect to reflections in this plane.

The final plane wave continuum state ψ_f, of the photoemitted electron must have 'even' reflection symmetry in the mirror plane. This is a condition of electron detection, as an anti-node at the position of the detector is required to detect the state. The total matrix element $A \cdot \langle \psi_f | p | \psi_i \rangle$, must also have even symmetry. Thus the orientation of A determines which initial states are excited. 'A' will have an even symmetry when parallel to the mirror plane and an odd symmetry perpendicular to the mirror plane. 'A' parallel to the selected mirror plane, will require initial and final states to be either both even or odd, and the final state is required to be even, thus the initial state is even. 'A' perpendicular to the mirror plane, requires both initial and final states to be different, thus the initial state is odd [1].

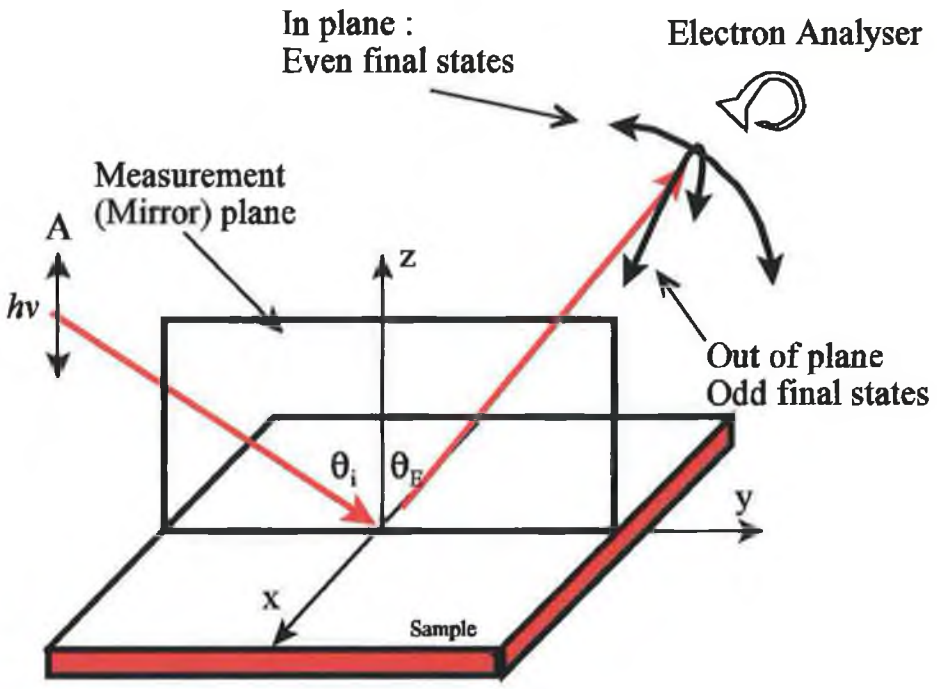

Figure 2.13 : Schematic illustration indicating how with the use of polarised incident light to probe the wavefunction symmetry (Parity) of states with angle resolved photoemission. With the incident polarisation parallel to the mirror plane, as shown, rotating the analyser parallel to and within this plane will indicate the states to have even parity. To detect states of odd parity, the analyser is rotated perpendicular to this plane.

2.7 : Interpretation of Photoemission

The interpretation of photoemission spectra has two primary functions, firstly the determination of the occupied electronic band structure of a crystal through the investigation of valence electrons with angle resolved photoemission (ARP), and the interpretation of core level spectra which reveals information about chemical bonding of the constituent elements.

2.7.1 : Core level photoemission

Koopmans' theory suggests that the binding energy E_B of a specific core level is roughly equal to the negative orbital energy ϵ_k, which can be calculated using the Hartree-Fock method. But as previously discussed, the screening effects due to the removal of the electron from both the specific atom and also the surrounding atoms affects the kinetic energy of the detected electron. These effects are termed screening or relaxation effects and are described as final state effects. Both initial and final state effects contribute to the observed energy of the photoemitted electron. The initial state is the ground state of the atom before the photoemission process. The binding energy of the electrons are affected by chemical bonds with other atoms, these changes are called chemical shifts. As the formal oxidation state of an element increases so too does the binding energy of the core level. For most samples this interpretation of changing E_B suffices.

Relaxation or final state effects can have a large impact on the binding energy, as discussed in section 2.5. The relaxation energy is comprised of atomic relaxation, from the specific atom, and extra-atomic relaxation, from the surrounding atoms. Most of the atomic relaxation component is due to the rearrangement of outer shell electrons, while the inner shell electrons have a much smaller contribution.

Surface atoms have a different stoichiometric environment than the equivalent bulk atoms, and result in chemical shifts. Specific surface chemical bonding may be attributed to different chemical shifts. Figure 2.14, shows S 2p core level spectra, where spectra (a) has been fitted with two spectra showing sulphur in two separate chemical environments due to the chemical shifting between the two, (b) indicates a change in the intensity ratio of the two bonding arrangements with the deposition of a submonolayer of manganese and (c) indicates the complete removal of one of the chemical bonding states. This data is discussed in detail in chapter 3.

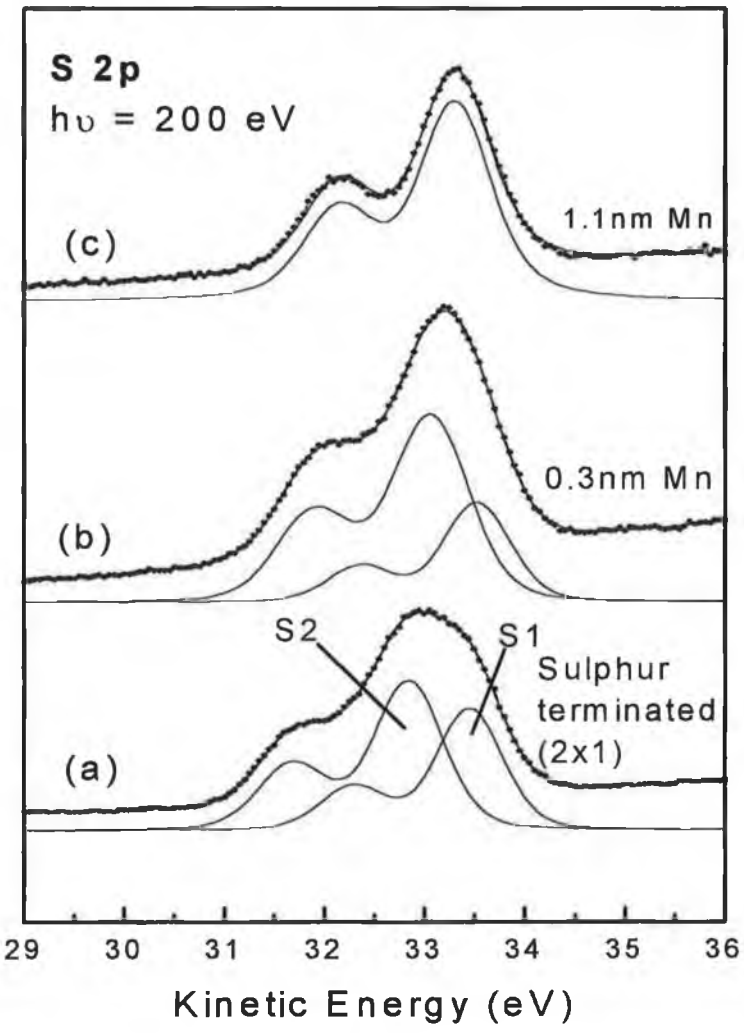

Figure 2.14 : S 2p core level spectra, where (a) has been fitted with two components showing that the S has two separate chemical environments, (b) indicates a change in the intensity ratio of the two bonding arrangements with the deposition of a sub-monolayer of manganese and (c) indicates the complete removal of one of the sulphur states [18].

2.7.1.1 : Fitting Core levels

Several effects contribute to the shape of core level spectral features. The spectrum primarily corresponds to the density of states of the atomic level, defined by the principle and orbital angular momentum quantum numbers, n and l. States with $l \neq 0$ (p,d and f) observe state splitting due to the coupling of the orbital and spin angular momenta of the electrons. The spin-orbit coupling results with total angular momentum $j = l \pm s$, signifying both parallel and anti-parallel coupling of the spin and orbital momenta. The two states have a different degeneracy by $m_j = 2j+ 1$, and the ratios of their intensities is the ratio of their respective degeneracies.

The line shape used to fit the core level is called a Voigt function, which is a Gaussian function convoluted with a Lorenztian function. The Lorentzian distribution is determined by the finite lifetime of the core holes. The Gaussian distribution is a combination of other broadening effects such as instrumental resolution limits, phonon excitation broadening, disorder or in-homogeneity effects. In addition when a system has a metallic character, the line shape assumes an asymmetry identified by a tail with lower kinetic energies and is as a result of plasmon losses. In the curve fitting procedure the energy position and intensity of each component is selected, along with the FWHM, spin orbit split and branching ratio of each component. These parameters may be allowed to move within limited degrees until the sum of the squares of the deviations is minimised, (χ^2), and in order to obtain a reliable fit, the core fitting parameters used must be mutually consistent. The background is also removed within the fitting procedure. The surface core level shifts are relatively small, tenths of an eV, and therefore obtaining structural information from the spectra demands high energy resolution. The intense nature of synchrotron radiation is ideal, as increasing resolution is accompanied by a significant loss of intensity.

Further information can be obtained by studying the spectra recorded at different

photon energies, and emission angles. Both effects change the surface sensitivity of the technique and thus information regarding the origins of the individual components may be obtained. Depending on the angular acceptance of the electron detector, diffraction effects may also affect the intensities of the peaks. Typically an angular acceptance of ~14^0 is wide enough to average out diffraction effects.

2.8 : Identifying Surface valence band States

The primary focus of chapter 4 of this thesis regards the identification and characterisation of the surface features in the valence region of GaN. The surface is a quasi-2D system, as its effects may extend a few lattice planes into the solid, therefore the identified states may be mapped within the 2-D Brillouin zone by applying the parallel final state momentum component from equation 23;

$$(24) \qquad p_{//} = \sqrt{2mE_{kin}}\sin\theta \Rightarrow k_{//} = \frac{\sqrt{2mE_{kin}}\sin\theta}{\hbar}$$

where θ is the angle of the emitted electron detected with respect to the surface normal.

Figure 2.15 shows the identified surface features mapped within the 2-D Brillouin zone, $k_{//}$ versus binding energy. The binding energy is calculated by measuring the kinetic energy relative to a Fermi edge, taken from a clean metal.

To identify surface states specific characteristics are identified. (1) A true surface state will be located in the gap of the bulk band structure projected on the surface. (2) The energy position of surface states are independent of photon energy, as they will have no $k_{\perp}$ perpendicular component, and finally (3), surface states are most likely to be sensitive to the condition of the surface, such as a reconstructed surface or surface adsorption of another material i.e. a gas.

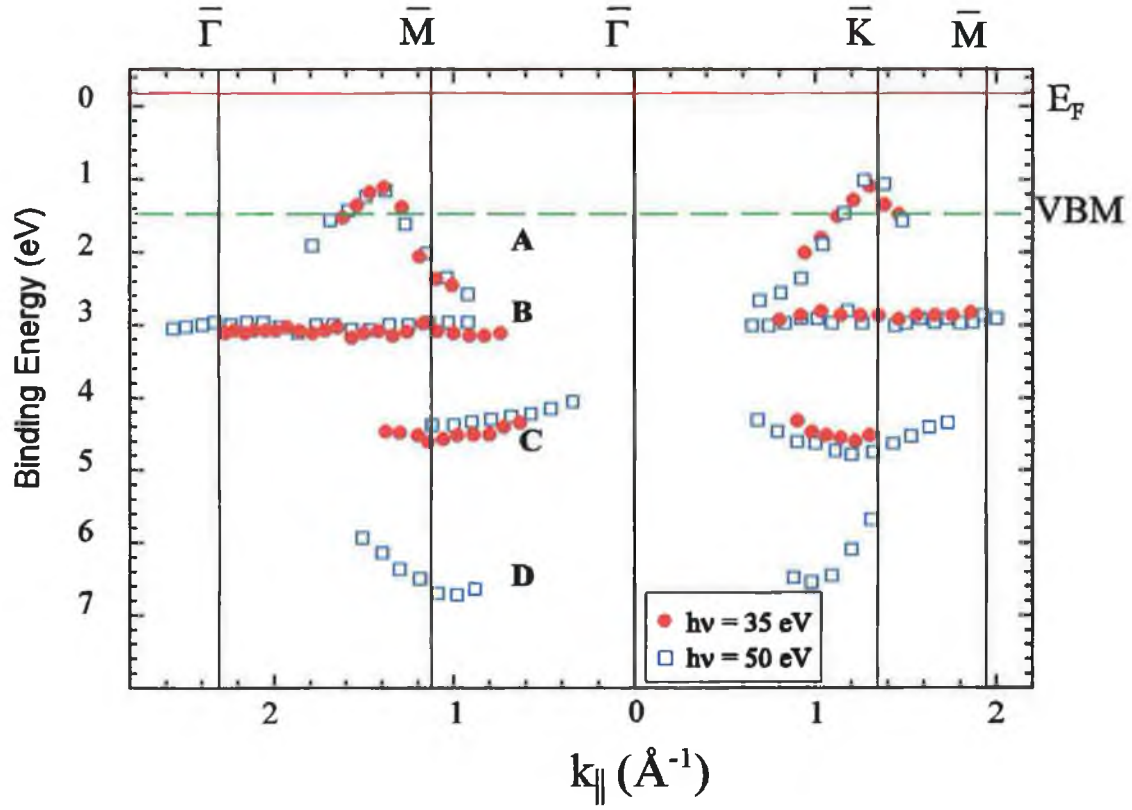

Figure 2.15 : The measured two dimensional surface band structure for the clean p-type GaN(0001)1x1 surface, mapped in the 1x1 surface Brillouin zone [19].

(1) Because the wave function of a surface state is spatially confined to the surface region, a true surface state will appear in an area of energy and momentum space of the crystal where there are no bulk states of the same $k_{//}$ and symmetry, no matter the $k_{\perp}$ component. Surface resonances are observed within the bulk band structure, representing mixed surface and bulk states.

(2) The second criteria, relies on the fact that surface states have no momentum component perpendicular to the surface, and therefore the respective binding energies do not disperse with changing incident energy as indicated in figure 2.15. Although some bulk states also show no dispersion with incident photon energy, due to broadening of final states and Umklapp transitions from flat regions of bulk bands. Thus we may say that, dispersing features with respect to photon energy are not surface states.

(3) The last criteria, relates to where these states may be altered with changes in the surface environment. Dosing the clean surface with hydrogen can affect any potential surface states. States may not be dramatically affected, particularly strong back bonded surface states, i.e. states which bond towards the sample. Adsorption may also have an adverse affect on the overall valence band structure, on both surface and bulk photoemission contributions.

2.8.1 : Orbital configuration and orientation

The photo cross-section intensity may also be used to investigate the electronic orbital configuration, due to its dependency on the interaction between the incident radiation and the orbital configuration.

When the polarisation of the incident light is parallel to the plane of reflection such as in figure 2.16, increasing the incident angle with respect to the surface normal, the cross-section of a p_z orbital increases, but for an s orbital configuration, the cross-section remains constant.

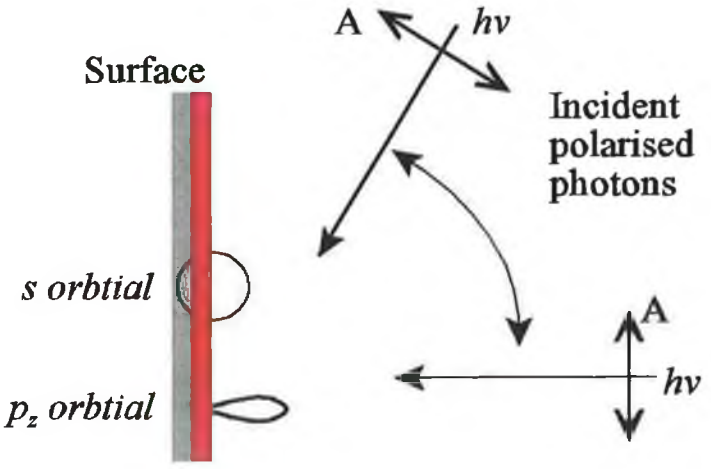

Figure 2.16 : If the incident light on the sample is linearly polarised parallel to the mirror plane, by changing the incident angle the photo crossection (A.p) of a p_z orbital maybe varied, while an s orbital will remain constant.

Figure 2.16 illustrates the experimental set up to probe the orbital configuration and figure 2.17 indicates the changing spectral intensities as the incident angle is modified.

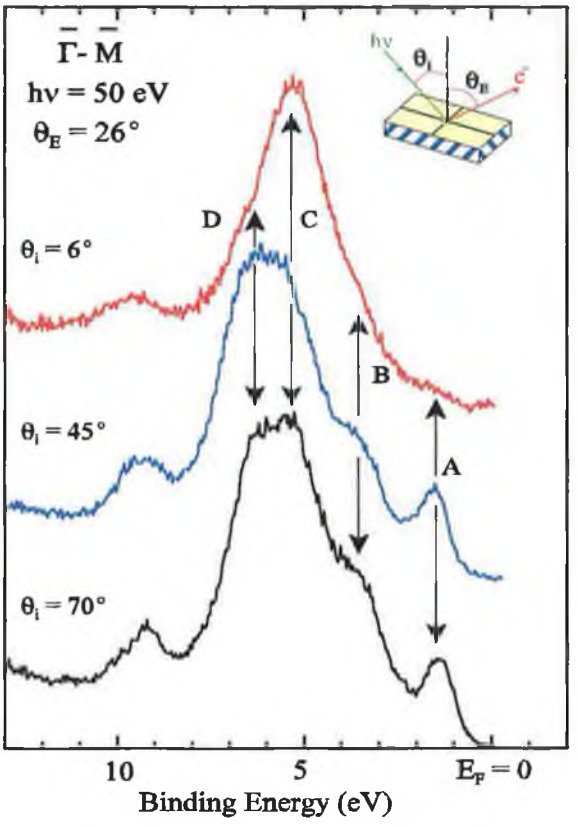

Figure 2.17; indicating the change in photoemission intensity with respect to changing incident angle depending on the orbital configurations. Features A,B and D show p_z orbital characteristics while C indicates an s orbital configuration [19].

2.9 : Soft x-ray emission and absorption spectroscopies

Chapter 5 investigates the bulk valence and conduction band density of states of the InGaN ternary alloy. To achieve this both soft x-ray emission and absorption spectroscopies (XES, XAS) techniques were employed. Figure 2.18 gives a simplified description of both processes. For XAS, an incoming photon is absorbed by removing an electron from a core shell to the unoccupied states. In SXE the core-hole created by the photon absorption is then filled by a radiative decay from an occupied state. These electrons may originate from

either core levels or from the valence bands. The x-ray emission is a low probability process, as the majority of the decay transitions are from non-radiative Auger processes. Due to the photon in/out nature of the x-ray emission, the technique is predominantly a bulk technique and the extreme surface conditions required by photoemission is not demanded by the so called fluorescence techniques

As with photoemission, if the single-electron theory is used to describe the absorption and emission processes, the transition probabilities are determined by a transition matrix as used in the Fermi Golden rule. This probability matrix multiplied by the density of states will determine both the emission and absorption spectral characteristics. Because of the small spatial extent of the atomic like core level wave-functions, the soft x-ray processes are predominantly intra-atomic, i.e. are localised at the absorption or emission site. In the soft x-ray regime, the energy of the incident photon field allows the optical transition to be treated within the 'dipolar' approximation. This approximation restricts optical transitions of angular momentum from initial to final states of ± 1. Thus if the incident photon creates a p core hole state then only s and d states may decay into the unoccupied core state or the ejected electron may only occupy an s or d unoccupied state. Either way only s and d states in the conduction or valence bands can be investigated.

Thus the techniques are site and symmetry sensitive, and also elementally specific, due to the small energy spread of core levels, and the general lack of energy overlap between the core states of different elements.

It also should be noted that for the interpretation of the experimental spectra, during x-ray emission the final state of the process whereby the core hole has been filled means that ground state calculation comparisons ought to be acceptable, however for x-ray absorption, calculated states should take into account the effect of the empty core holes. These empirical observations are called the 'final state rule' according to Von Barth and Grossman [20, 21].

As noted, the probability of photo-exciting a core electron depends on the density of unoccupied final states at a particular energy above the core level. Thus the absorption spectra reflects the unoccupied partial density of states.

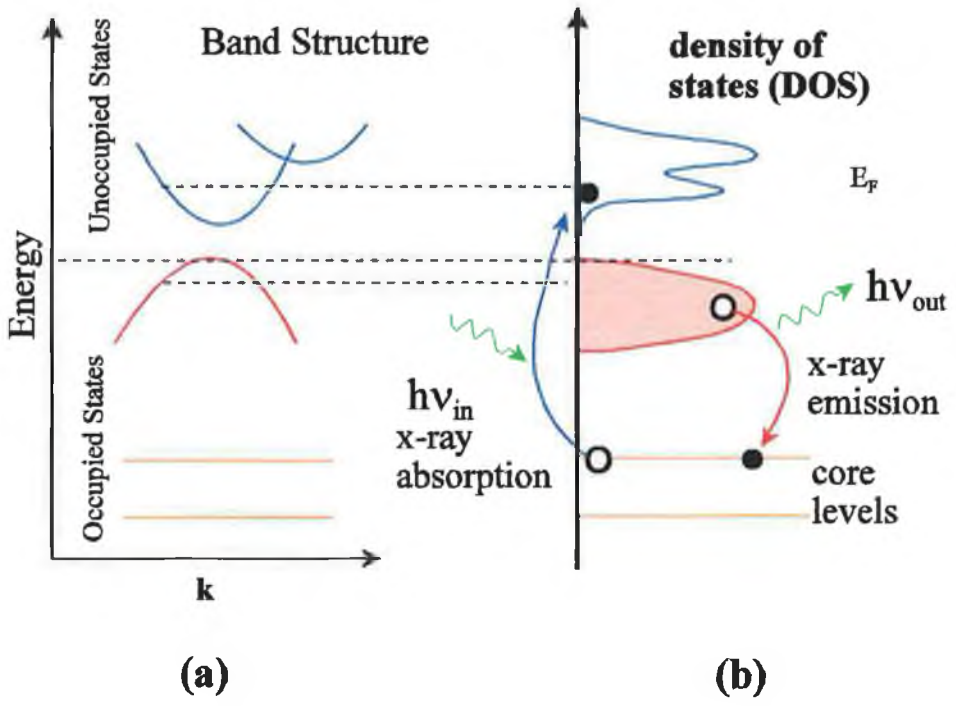

Figure 2.18 : A schematic illustration of the basic processes of x-ray emission and absorption techniques. (a) Dispersion of the crystal momentum of an ideal semiconductor, showing core levels, valence and conduction bands. Core levels are atomically localised and show no momentum dispersion. (b) The density of states is shown by summing throughout k space. An incoming photon excites an electron from a core level, creating a hole, (x-ray absorption). A subsequent de-excitation from the occupied valence band can result with x-ray emission. Thus the element specific density of states (partial DOS) of both occupied and unoccupied bands may be investigated [22].

Absorption spectra may be recorded as either total electron yield (TEY), or total flourescent yield (TFY). TEY records all the electrons escaping from the sample regardless of their specific kinetic energy. These electrons come from both photoelectrons and Auger electrons. The photoelectrons need to make a transition above the vacuum level to be detected. Many 'primary' electrons from both photoemission and the Auger process scatter and loose energy and create a 'cascade' of lower energy 'secondary' inelastic electrons. This cascade forms the main part of the TEY signal.

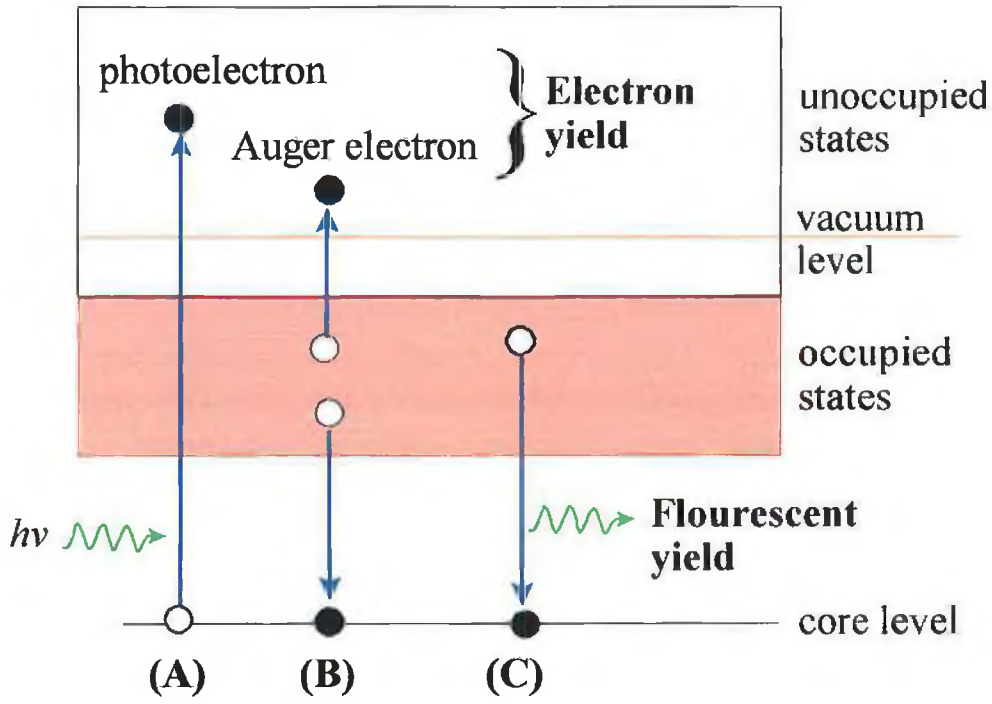

Figure 2.19 : X-ray absorption may be measured by three different processes, (A) a core hole is created with the absorption of a photon, a compensation current filling the hole may be recorded. (B) Electrons excited and emitted from the sample may be counted with a channeltron, (electron yield). (C) A total count of x-ray emission due to de-exciting electrons filling the core holes, (flourescent yield) [22].

Due to the low kinetic energy of the electrons which make up the vast majority of the signal, the electrons emitted from deep in the bulk will not be able to surmount the potential barrier once they have arrived at the surface. TEY has therefore a more restricted probing depth of ~50 -100Å [23].

For metals or semiconductors TEY spectra may be measured by recording the current flowing into the sample, compensating ejected electrons. For insulators the spectra are recorded using a channeltron to count the emitted electrons. To measure the unoccupied states using the TFY method, the total number of photons emitted from the sample is measured using the soft x-ray emission spectrometer, where the entrance slit is open wide and the diffraction gratings reflect zero order to maximize the signal. Due to the low interaction cross-section between x-rays and matter, the TFY technique is far more bulk sensitive.

2.10 : Instrumentation

Synchrotron radiation is a common source for producing both UV photons and soft x-rays for photoemission and flourescent techniques respectively. The photoemission and x-ray emission detection processes are considerably different requiring electron and soft x-ray detection respectively.

2.10.1 : Synchrotron Radiation (SR)

UV and soft x-ray sources such as He discharge lamps and Mg/Al Kα x-ray sources have been the predominent tools for studying the electronic properties and chemical composition of surfaces. With increasing availability of synchrotron facilities, home based sources cannot compete with the resolution and fluxes offered. The ability to tune the energy of the synchrotron radiation also makes absorption studies possible, and the plane polarisation of the photons as well as the ability of insertion devices to manipulate the polarisation makes synchrotron radiation a very powerful tool.

A full description of synchrotron theory and equipment, from storage devices (rings), focusing mirrors and diffraction gratings is given in reference [24]. The following entails the basics of a synchrotron facility.

Synchrotron radiation is emitted by relativistic electrons or positrons when deflected in a magnetic field, as illustrated in figure 2.20. To produce such a set-up, a storage ring, in vacuum, consisting of several bending and focusing magnets controlling the trajectory of electrons/positrons which circulate in tight bunches.

These bunches are accelerated to energies of the order of GeV by a radio frequency (RF) accelerating cavity, operated in phase with the arrival period of the electron bunches. Because the particles are at relativistic speeds the SR is emitted in a narrow cone in a tangential direction from the bending curve at the time of emission. The RF cavity continues to run during operation in order to compensate for the loss of energy due to the synchrotron radiation emission process. While this prolongs operation time, eventually due to collision losses, a re-injection of source particles is required, for useable SR fluxes.

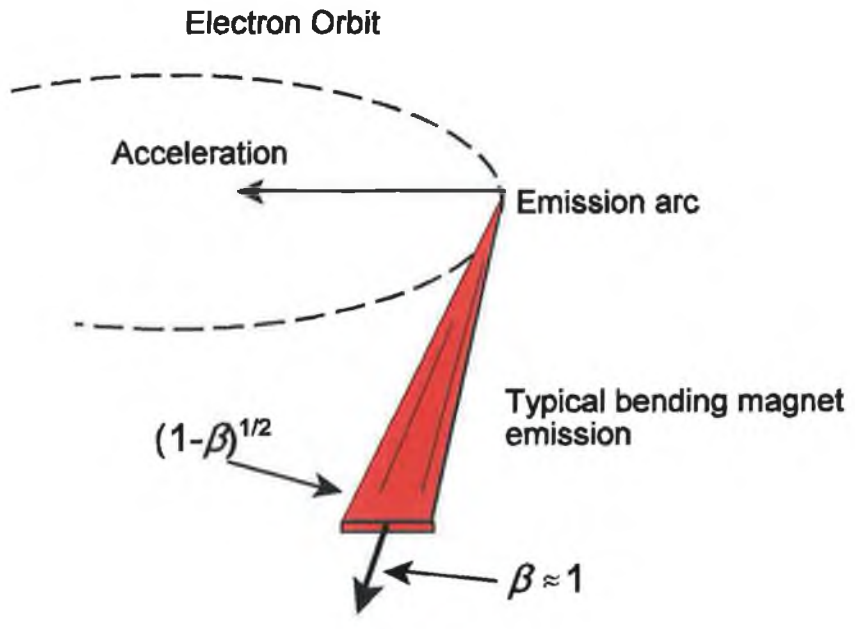

Figure 2.20 : Angular intensity distribution of relativistic electrons/positrons from a typical bending magnet. β, velocity in units of c. As *β goes to 1, the angular distribution narrows.*

SR is a photon source with several specific qualities, including a broad spectrum band, very high intensity, with a very high degree of collimation and is highly plane polarised. The spectrum of light emission may be characterised by a critical energy, in KeV:

$$(25) \qquad \epsilon_c = 2.2E^3/R,$$

where E is the stored energy in GeV and R is the bending radius (m) of the magnet. The intensity drops quickly above this energy but slowly below. The bending magnet produced radiation can be enhanced by other insertion devices, namely wigglers and undulators. A bending magnet will produce a searchlight radiation pattern as previously shown in figure 2.20, a wiggler will extend the useable radiation energy to higher values, while an undulator will significantly increase the intensity, particularly in the soft radiation regime i.e. UV and soft x-rays.

2.10.2 : Beamline Characteristics

The function of a beamline is to gather and monochromate the light emitted from the ring and finally to focus the light into as small a spot as possible onto the sample in the analysis chamber. The three beamlines utilised throughout the thesis, all have different parameters, but the basics are the same. Both beamlines U4A at the National Synchrotron Light Source (NSLS), Brookhaven and 4.1 at the Daresbury synchrotron facility are on bending magnets, both have three grating monochromators and supply UV radiation, up to ~250eV. Both shallow core level and valence band photoemission spectroscopies were performed on both of these beamlines. The X1B beamline also at NSLS, supplies soft x-ray radiation, has only one grating monochromator offering a range of light from 200eV to 1200eV. X1B obtains its light from an undulator insertion device, which supplies a far superior flux than a bending magnet. Due to the extremely low count rate of soft x-ray emission spectroscopy, the high flux is required to make the technique feasible.

The basic optical outline of the U4A bending magnet beamline is shown in figure

2.21. The beamline was built by Bell labs [25], and was specifically designed for use on the .8GeV UV ring at NSLS, to operate from 8eV to 250eV. The front end mirror collects the light directly from the bending magnet. This focuses the light on to the monochromator gratings. The monochromator is a 6m/160° toroidal grating instrument, with three gratings with 288, 822, and 2400l/mm. The light passes through both entrance and exit slits. The beamline has been updated with the installation of a linear motion drive mounted exit slit as to optimise the exit image on the Rowland circle (as discussed in appendix A). The resolution of the resultant beam leaving the grating depends on the area of grating illumination and the physical slit width, which are interdependent. The exit slit collimates the final image of the selected energy. This beam passes through the front chamber and is refocused into the angle resolved chamber. Figure 2.22 and 2.23 show the photon intensity throughout the useable energy range of both U4A and 4.1 beamlines respectively. All the relevant beamline details are available on the web at http://lsu13f.nsls.bnl.gov/u4a , for U4A, NSLS and http://srs.dl.ac.uk/station/4.1 for beamline 4.1 SRC.

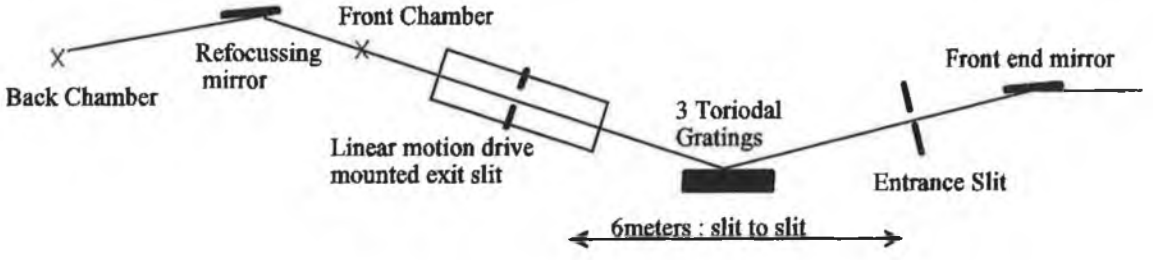

Figure 2.21 : Optical layout of beamline U4A, (UV ring, NSLS). The front mirror directs the synchrotron radiation through the entrance slit and onto a six meter radius toroidal grating monochromator (TGM). Three interchangeable gratings return an energy range of ~8eV to ~250eV. The diffracted beam passes through the exit slit, passes through the front chamber and is refocused to the sample position of the back chamber.

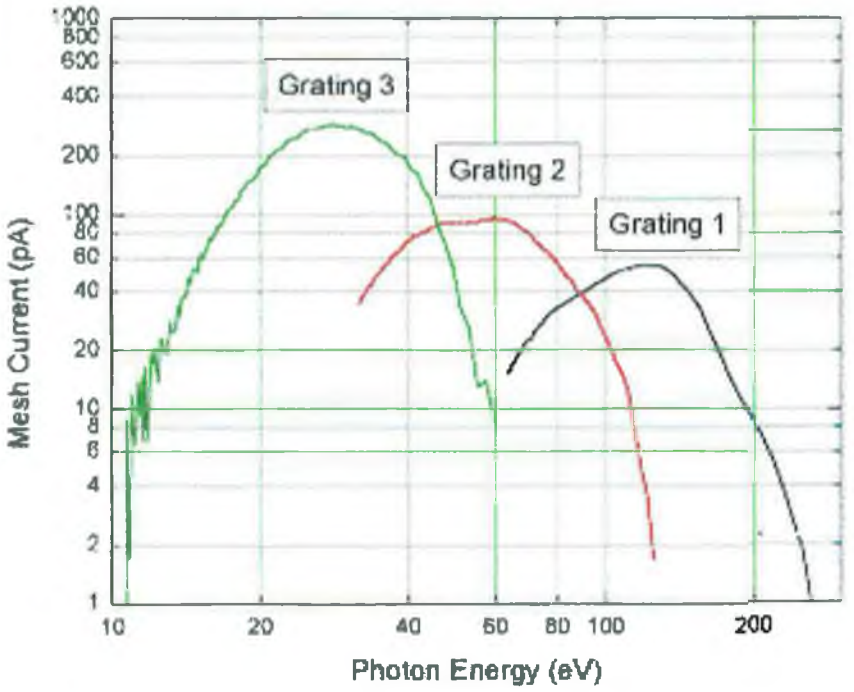

Figure 2.22 : A mesh placed between the exit slit and front chamber of U4A to read total intensity versus photon energy, indicating the useable energy range of the beamline.

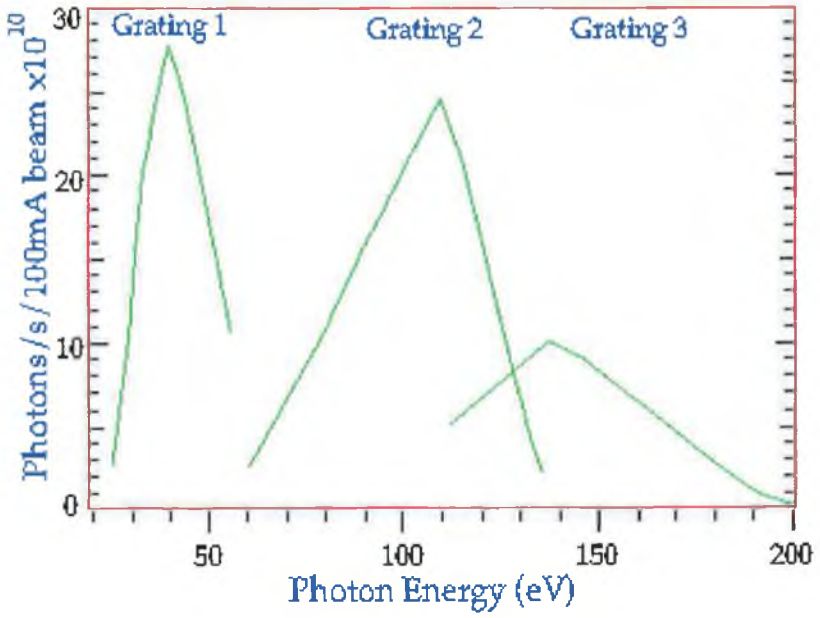

Figure 2.23 : Estimated photon intensity with respect to photon energy. Downloaded from http://srs.dl.ac.uk/station/4.1 .

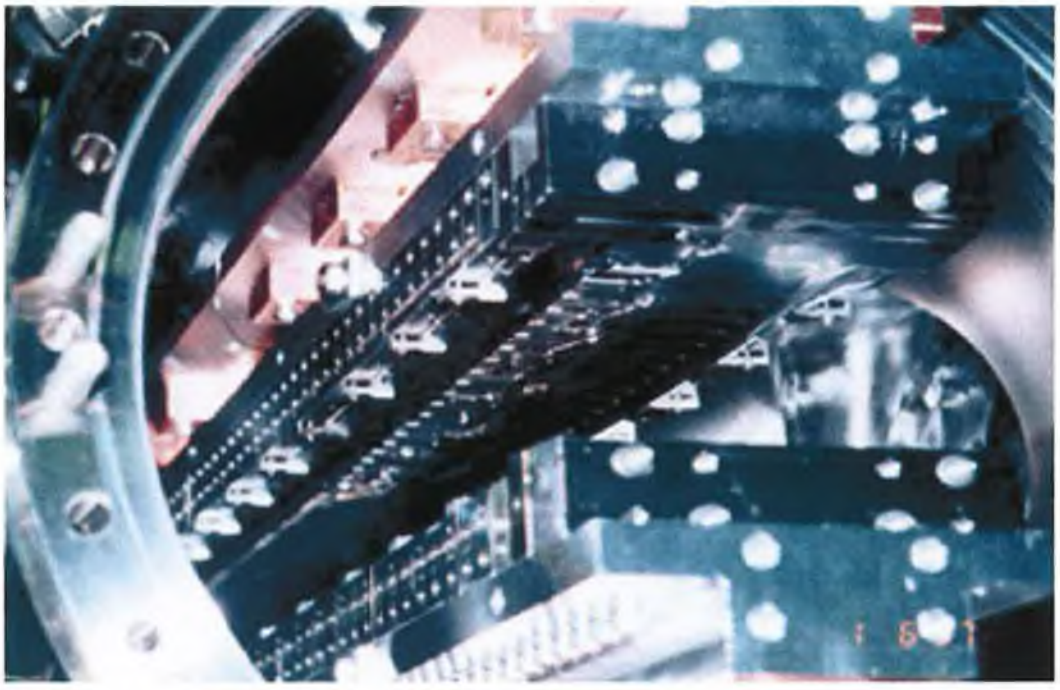

Figure 2.24 : Photograph of an undulator insertion device during installation at ESRF, Grenoble. The alternating magnetic pieces, make a corridor through which the electrons pass, transversely oscillating producing synchrotron radiation

The soft x-ray spectroscopy studies were recorded on X1B at NSLS, and as mentioned earlier the synchrotron light was produced with an undulator insertion device as opposed to a typical bending magnet. An undulator is a periodic electromagnetic structure typically made of a series of magnetic pairs with alternating magnetic directions which make the electrons oscillate transversely within the plane of the storage ring. Figure 2.24 shows a photograph of a typical horizontally planar undulator at ESRF. Some undulators may force a helix path (a helix undulator as opposed to a planar undulator). The aim is not only as mentioned to increase the intensity but also to produce quasi-monochromatic radiation. The emission characteristics of the undulator can be altered by changing the separation between the magnetic pole pieces. Figure 2.25(A) graphs the complete undulator characteristics, showing grey scale emission intensity with respect to emission energy and undulator gap separation. The interference effects within the undulator result in several

energy dependent intensity peaks, shown in figure 2.25 (B) at a specific undulator gap .

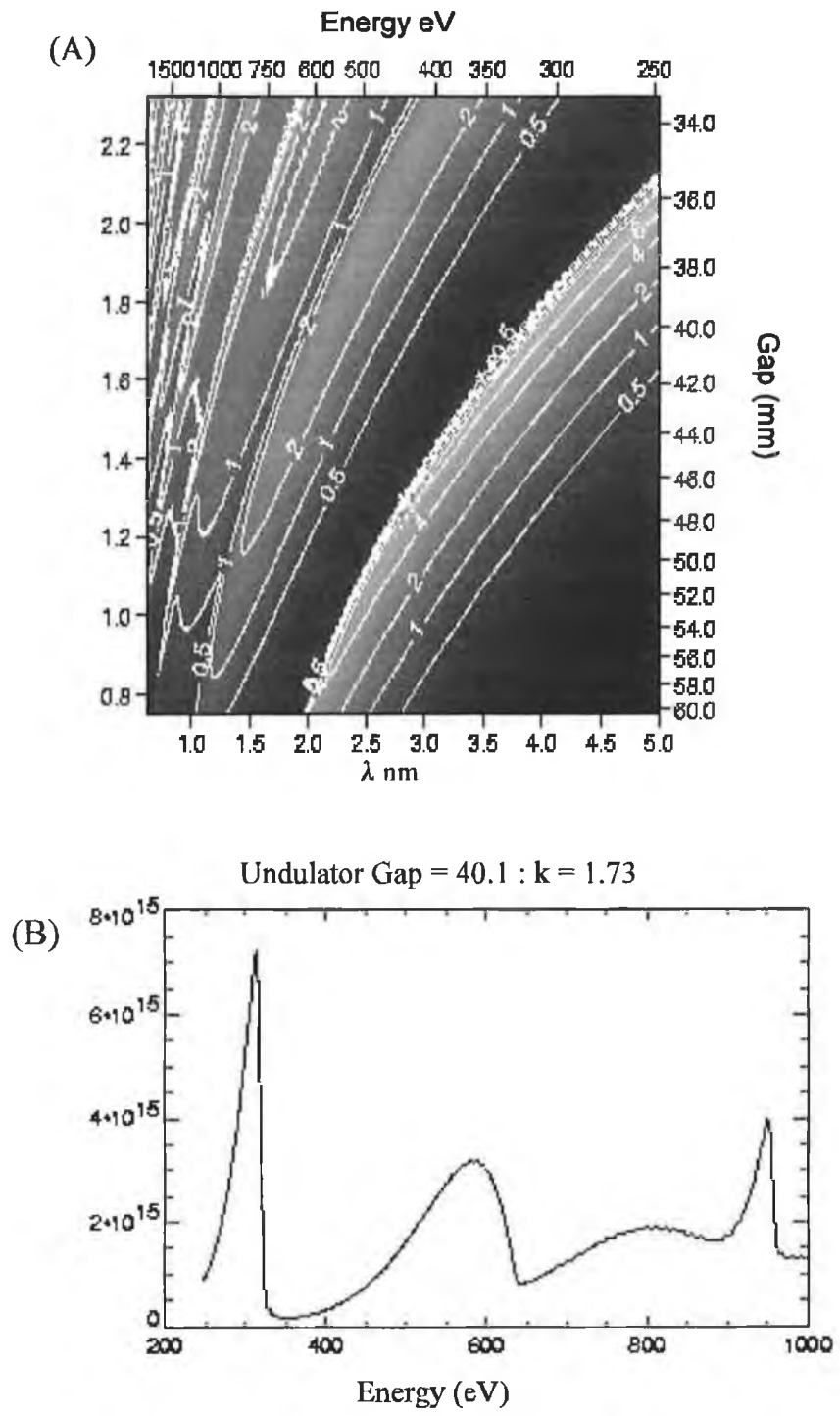

Figure 2.25 : (A) Plot showing the radiation emission intensity from the X1B undulator with respect to gap changes and energy emission. (B) An intensity versus energy plot with a specific undulator gap.

2.10.3 : Review of Detection Devices

While photoemission detects emitted photoelectrons from a sample, soft x-ray flourescent spectroscopy detects emitted x-rays, thus both techniques have different detection requirements. Electron detection requires that no magnetic fields exist within the experimental chamber, due to the effect of the field on the trajectory of the electron. To circumvent this problem, a mu metal shield is placed inside the stainless steel chamber to isolate the electrons from any stray magnetic fields. Both techniques require vacuum conditions, soft x-ray emission is bulk sensitive and does not need the ultra clean surfaces which are paramount for high quality photoemission. Thus the vacuum limits of XES are set by the nature of the soft x-rays which requires high vacuum, HV. The vacuum limits for photoemission are set by the ability to keep the sample surfaces clean, i.e. ultra high vacuum, UHV.

2.10.4 : Electron Detector

The primary objective of the electron detector is to measure the energy distribution of the detected electrons. The most important characteristics of a detection system are, first, the energy resolving power ρ where (26) $\rho = E/\Delta E_A$, where E is the detection energy, ΔE_A is the energy spread of the detected electrons through the system and second, the solid angle from which electrons can be accepted, $\Omega/2\pi$. The acceptance angle is critical in angle resolved photoemission, if this angle is large, the energy resolution may be improved due to a higher count rate but at the cost of momentum resolution. With a smaller acceptance angle a higher momentum resolution may be obtained at a cost of energy resolution. Momentum resolution is not an issue in core level photoemission, thus a wider acceptance angle will allow for a much greater count rate and allow for greater energy resolution. Angle integrated photoemission, as it is termed also avoids diffraction effects by accepting a wide angular range of electrons.

The ARUPS detector mounted on U4A was designed and constructed by S. D. Kevan [26], and is a modified 180^0 spherical deflection analyser (SDA). The aim of the detector was primarily two-fold, both to achieve high angular resolution and to operate up to 300eV kinetic energy with good energy resolution. The resolving power of the SDA has been reported to be twice that of the alternate techniques [27]. The design also allows for easy combination with an input electron lens. The SDA focuses in two dimensions, with linear energy dispersion. Thus the focused exit plane should be well defined, allowing multi-parallel detection in this case performed by a Galileo-electron optics supplied multi-anode array detector.

The physical size of the detector is important in determining both the range of kinetic energies to be detected and the overall count rates. If the focused incident photon beam on the sample has a diameter of ω_s. To collect as many electrons as possible the lens of the detector must image this spot onto the analyser entrance, ω_a. The possible resolution may be determined by the following :

$$\Delta E = \left(\frac{\omega_a}{2r_0}\right) E_a , \qquad (27)$$

where E_a is the analysis energy or pass energy through the detector and r_o is the mean radius of the analyser. The pass energy is selected through the lens system, the lower the pass energy the greater the energy resolution. It may seem therefore that r_0 is arbitrary if ω_a or E_a can be altered with the incoming lens, but spherical aberration effects of the analyser must be considered. There is a physical limit on ω_s/ω_a and E_s/E_a, where E_s is the electron beam energy emitted from the sample. In conclusion, the larger r_0, the higher resolution and the more counts possible. The real restriction is then the physical size of the chamber as the analyser is housed in the vacuum chamber on a two axis goniometer. The goniometer allows the detector to move in front of the sample in order to detect electron

emission off sample normal.

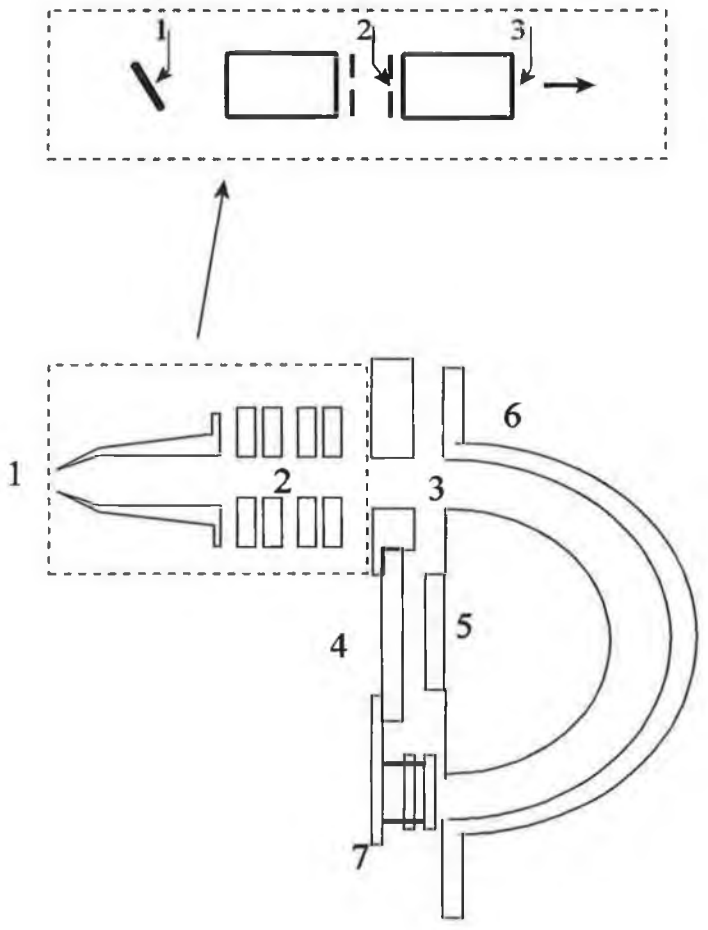

Figure 2.26 : A cross-section of the Kevan electron analyser design [26]. 1) Sample position, 2) focusing position after first lens, 3) focusing position after second lens and entrance to the analyser, 4) mounting plate, 5) inner hemisphere, 6) outer hemisphere, and 7) multi-anode detector.

The radius of the detector is 50mm, the optimal image diameter ω_a, was selected as to both encompass the complete spot of the sample, and give the best ΔE at the desired analysis energy E_a. 'ω_a' was selected to be ~.5mm, therefore $\Delta E/E_a$ is .005 and the energy resolution is theoretically ~20meV at an analysis energy of 4eV. The injection lens was thus designed with an overall linear magnification ω_a/ω_s of .5, knowing that the typical focused spot was ~1mm. The ratio of the kinetic energy of the electrons from the sample and the

pass energy, E_s/E_a, is determined by the Helmholtz-Lagrange relation, and is dependent on the angular acceptance angle of the lens. If the acceptance angle is ~.3^0 then this relation calculates the E_s/E_a ratio as ~90. This implies that if the photoemitted electron has a kinetic energy of 360eV, the effective pass energy will be 4eV.

2.10.5 : Soft x-ray emission detector

The relatively new interest in soft x-ray emission spectroscopy is due to advancements in both soft x-ray spectrometers and synchrotron radiation sources. New spectrometer designs have made the technique far more accessible and widened the investigative abilities of the inherent capabilities of soft x-ray spectroscopy.

Tunable excitation has allowed emission from chemically non-equivalent sites of the same atomic species to be differentiated where the excitation selectivity is typically better than an eV. X-ray absorption features represent separate chemical environments for a particular element, and the incident photon energy can be selected at each separate feature thus each chemical environment of the occupied bands may be probed independently. This resonance effect, may be described as resonant inelastic x-ray scattering (RIXS). This technique can probe the momentum resolved bulk electronic structure and because the technique is itself bulk sensitive, it may prove very useful, compared to ARP which is highly surface sensitive and requires atomically clean and ordered surfaces. The polarisation properties of synchrotron sources allows the preferential excitation of specifically oriented sites e.g $p_{x,y}$ or p_z, thus both x-ray emission and absorption techniques can study the various symmetry of states.

Several spectrometer designs have been recently implemented, the first of which by Nordgren which is now manufactured commercially by Gamadata/Scienta [28], was used at X1B undulator beamline at NSLS [29-31].The focus of the design is two-fold, adaptability/portability, so it can be used on different chambers and experimental set-ups.

To do this the source to detector distance needs to be minimised. Although resolution suffers as it depends on the simple geometrical scaling, and the bigger the distances between the grating and the detector the better the resolution from a given grating ruling density. A compromise is found by using multiple gratings. Because the detector is small it is also possible to attach it to a completely rotatable chamber so to utilise the polarisation properties of the synchrotron source.

The basic optical features of the detector are shown in figure 2.27. The emitted photons pass through the entrance slit, which is taken as the image source. Two moveable shutters (flags) select the grating. From the pre-selected grating the monochromatised photons are then incident on an area detector which can be moved on a three axis coordinate system.

Rowland optical geometry (discussed in Appendix A) determines the focus position and while each of the gratings form separate optical systems, the detector design merges these systems, with a common source position (entrance slit), and moveable detector (image position). Each of the gratings have separate ruling densities as well as radii to complement each others energy ranges and merge the three optical systems. The gratings had the following energy ranges, G1 : 300-1000eV, G2 : 100-450eV, and G3 : 50-200eV.

The instrumental dispersion is planar which allows the entrance slit to be positioned parallel to the incident photon beam, thus maximising the emitted photon capture with a grazing incidence on the sample. The detector as shown is comprised of multi-channel plates coated with CsI for improved efficiency [32] with a position sensitive resistive anode read-out of detected position [31]. The detector has a 40x40mm^2 surface area with 100μm resolution. An electrode is placed at the front of the detector to absorb the secondary electrons, which may be mistakenly registered by the detector anodes. This is likely particularly as the detector is at grazing angle with respect to its incident photon beam. The efficiency of the detector varies with photon beam energy, as the photoemissivity of CsI has

a strong energy dependence, but the overall efficiency is estimated to be the order of 20%.

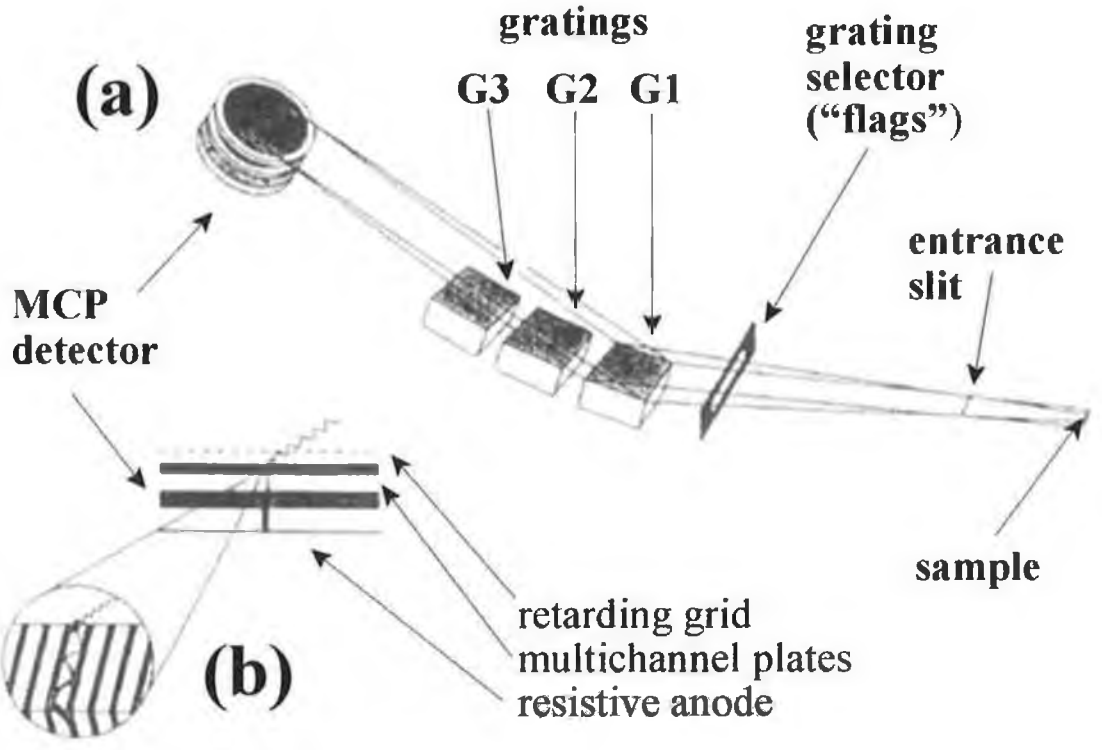

Figure 2.27 : Principle features of the Nordgren grazing incidence soft x-ray emission spectrometer design (XES 300). And (b) the structure of the multi channel plate detector (MCP)

2.11 : References

1. Zangwill, A., *Physics at Surfaces*. 1987: Cambridge University Press.
2. Feuerbacher, B., B. Fitton, and R.F. Willis, *photoemission and the Electronic Properties of Surfaces*. 1978.
3. Hufner, S., *Photoelectron Spectroscopy*. Solid State Sciences, ed. Springer. 1995.
4. Davisson, C. and L.H. Germer, *Diffraction of Electrons by a crystal of Nickel.* The Physical Review, 1927. **30**(6).
5. Hertz, H., Ann. Physik, 1887. **31**: p. 983.
6. Einstein, A., Ann. Physik., 1905. **17**: p. 172.
7. Vickerman, J.C., *Surface Analysis*. 1998: Wiley.
8. Mahan, G.D., Phys. Rev. B, 1970. **2**: p. 4334.
9. Schiach, W.L., in *Photoemission in solids*, M. Cardona and L. Ley, Editors. 1978.
10. Li, C.H., A.R. Lubinsky, and S.Y. Tong, Phys.Rev. B, 1978: p. 3128.
11. Holland, B.W., Surf. Sci, 1977. **68**: p. 1977.
12. Liebsch, A., Phys. Rev. Lett, 1974. **32**: p. 1202.
13. Pendry, J.B., Surf. Sci., 1976. **57**: p. 679.
14. Thorner, G. and G. Borstel, Physica Status Solidi, 1984. **b(126)**: p. 617.
15. Pendry, J.B., *Low Energy Electron Diffraction*. 1974.
16. Smith, N.V., CRC Critical Reviews in Solid State Science, 1971. **2**: p. 45-83.
17. Bergland, C.N. and W.E. Spicer, Phys Rev. A, 1964. **136**: p. 1030.
18. Hughes, G.J., *et al., Core level photoemission study of the deposition of thin manganese layers on sulphur terminated InP(100)surfaces.* Surface Science, 1999. **431**: p. 1.
19. Ryan, P., *et al., Surface electronic structure of p-type GaN(0001).* Surface Science Letters, 2000. **467**: p. L827-L833.

20. Barth, U.v. and G. Grossman, *The effect of the core hole on x-ray emission spectra in simple metals.* Solid State Communications, 1979. **32**: p. 645.

21. Barth, U.v. and G. Grossman, *Dynamical effects in x-ray spectra and the final state rule.* Physical Review, 1982. **B25**: p. 5150.

22. Stagarescu, C.B., *Soft X-ray Emission and Absorption Studies of Semiconductors and Organic Molecular Solids*, in *Physics Department*. 1999, Boston University: Boston.

23. Stohr, J., *NEXAFS Spectroscopy*. 1992, Berlin: Springer.

24. Koch, E.-E., *Handbook on Synchrotron Radiation*, ed. D.E. Eastman and Y. Farge. 1983: North-Holland Publishing Company.

25. Thiry, P., *et al.*, *A 6m Toroidal-Grating-Monochromator beam line for high momentum resolution photoelectron spectroscopy.* Nuclear Instruments and Methods in Physics Research, 1984. **222**: p. 85-90.

26. Kevan, S.D., *Design of a high-resolution angle-resolving electron analyser.* Re. Sci. Instrum., 1983. **54**(11): p. 1441.

27. Roy, D. and J.D. Carette, *Electron Spectroscopy for Surface Analysis*. 1977.

28. *Gamdata/Scienta AB, P.O. Box 15120, S-750 15 Uppsala, Sweden, (http://www.gamadata.se).* .

29. Nordgren, J. and R. Nyholm, Nucl. Instr. Meth., 1986. **A 242**: p. 246.

30. Nordgren, J., *et al.*, Rev. Sci. Instru., 1989. **60**: p. 1690.

31. Nordgren, J. and J. Gao, *Instrumentation for soft X-ray emission spectroscopy.* Jrnl.of Electron spectroscopy and related Phenomena, 2000. **110-111**: p. 1.

32. Fraser, G.W., *et al.*, Nature, 1982. **300**: p. 509.

Chapter 3

Core Level Photoemission Study of the Deposition of Thin Transition Metal Layers on Sulphur Terminated InP(100) Surfaces

3.1 : General Introduction

III-V semiconductors, in particular InP and GaAs have been extensively investigated for their potential applications in high speed electronic and optoelectronic devices. Their advantages over silicon include, higher electron mobility, direct energy band gap and the ability to grow a variety of many useful heterojunction structures. However, they have their disadvantages including cost of fabrication but more importantly, the electronic quality of the surfaces are very poor, and requires the development of surface treatment procedures which result in restoring desirable electrical, chemical and physical properties to the surfaces. The objective of surface 'passivation' is still in the research and development phase and has not been transferred to the commercial world due primarily to its limited success. The inability to control the properties of the surface, metal to III-V and insulator to III-V interfaces have hindered the potential use of these materials.

The 'passivation' term describes the objective of stabilizing the chemical and electronic properties of the surface, so that when exposed to operating ambient conditions the surface retains its ideal electrical characteristics. Silicon has been successfully passivated by the growth of a SiO_2 overlayer, but the native oxides grown on III-V semiconductors have not proved successful.

Many studies have investigated the passivation of InP and GaAs, by S termination with varying degrees of success [1]. With the ability under controlled environments, to passivate these surfaces, it is suggested that the process could reduce the level of interdiffusion across a metal-semiconductor interface which occur when thin metal layers are deposited on the III-V surfaces. Several studies have investigated the ability to deposit

thin layers of transition metals on S terminated GaAs, in the attempt to reduce interdiffusion and to grow more abrupt interfaces [2, 3].

3.1.1 : Surface Structures

To start, it is necessary to develop an understanding of the atomically clean surface. The ideal (100) surface of a III-V material is polar and in the case of InP being either terminated entirely by In or P. Although, such bulk termination at the surface is rarely achieved with III-V semiconductors, as the surface generally reconstructs. It is reported that sputtering and annealing of the InP(100) surface results in an In rich (4x2)/c(8x2) reconstruction similar to Ga rich reconstructions found on GaAs(100) [4-6]. However more recent studies using similar cleaning procedures have shown (2x4) reconstructions which may be either In or P rich [5, 7].

Our experiments found that the clean InP (100) surface formed a clear (2x4) reconstruction. Mac Pherson et al [5] proposed several possible (2x4) reconstruction models for the InP(100) surface involving a combination of dimer rows and missing dimers and trimers. These models have been supported by STM, XPS results and model calculations. Figure 3.1 shows a three P dimer with one missing dimer row reconstruction model. A vast array of studies, primarily on GaAs have led to general principles when formulating possible surface structures [8, 9]. The cation (In, Ga) dangling bonds are significantly higher in energy than the anion (As, P) dangling bonds. The reconstruction models also allow for the surface to remain uncharged, energy reduction of the surface occurs through the dimerisation of the surface atoms which leads to a reduction in the density of dangling bonds at the surface.

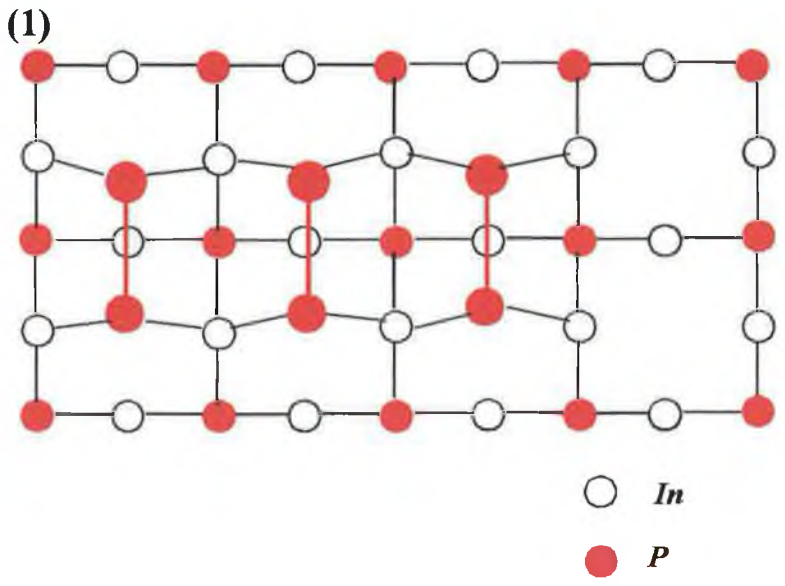

Figure 3.1 : A three P dimer with one missing dimer reconstruction model for the InP(100)(2x4) from MacPherson et al [5].

Several deposition procedures and techniques including ammonium sulphide based wet chemistry, H_2S gas exposure and also vacuum based elemental sulphur have been investigated on InP(100) [7, 10-25]. This study used a UHV compatible electrochemical sulphur cell [26-29], which generated small amounts of sulphur. The sulphur source is generated from a compressed pellet comprised of a Pt/Ag/AgI/Ag_2S/Pt cell. The pellet was formed by pressing powders of Ag, AgI, and Ag_2S together in between sheets of platinum mesh. The pellet was put into a glass tube 4cm long and 5mm wide, as shown in figure 3.2. In order to heat the electrochemical cell, a tantalum cylindrical shield was placed around the glass tube and wrapped by a tungsten heating element. The cell was mounted on a UHV flange as all components were vacuum compatible.

When heated to ~200^{0}C the cell produces a voltage of approximately 200mV. At this point an external bias is applied across the pellet. An ion current will flow through the cell as the Ag ions are removed from the silver sulphide, and are transported through AgI

which is an ionic conductor at 200°C. The cell is run in a 'constant current' mode whereby the breakdown of AgI is constant ensuring a consistent level of molecular sulphur emission. The molecular sulphur under UHV conditions effuses from the cell from the end face of the pellet. The prepared surface is placed a few centimeters from the cell during S emission. Typical exposure times of 5-10 minutes result in a saturation coverage between 1 and 2 monolayers. After deposition the sulphur treated surface is annealed to ~300^{0}C to remove the excess sulphur.The InP(100) surface is reported to form a (1x1) reconstruction after sulphur deposition and with subsequent annealing at ~350^{0}C forms a further (2x1) reconstruction. Mitchell et al [7] proposed a simple surface dimer model to explain the (2x1) reconstruction, as shown in figure 3.3.

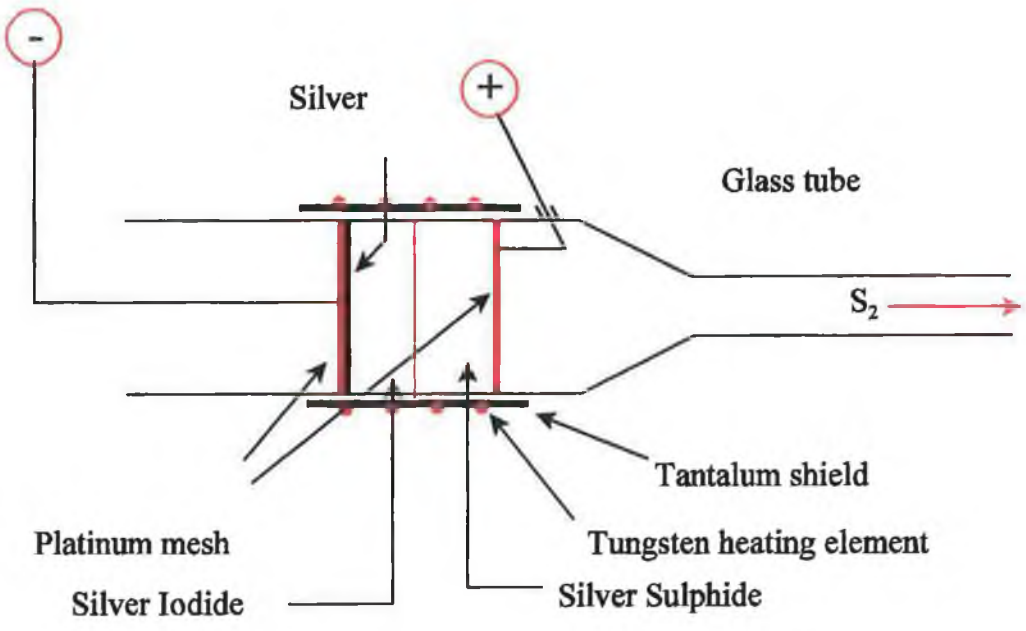

Figure 3.2 : A schematic illustration of the electrochemical sulphur source.

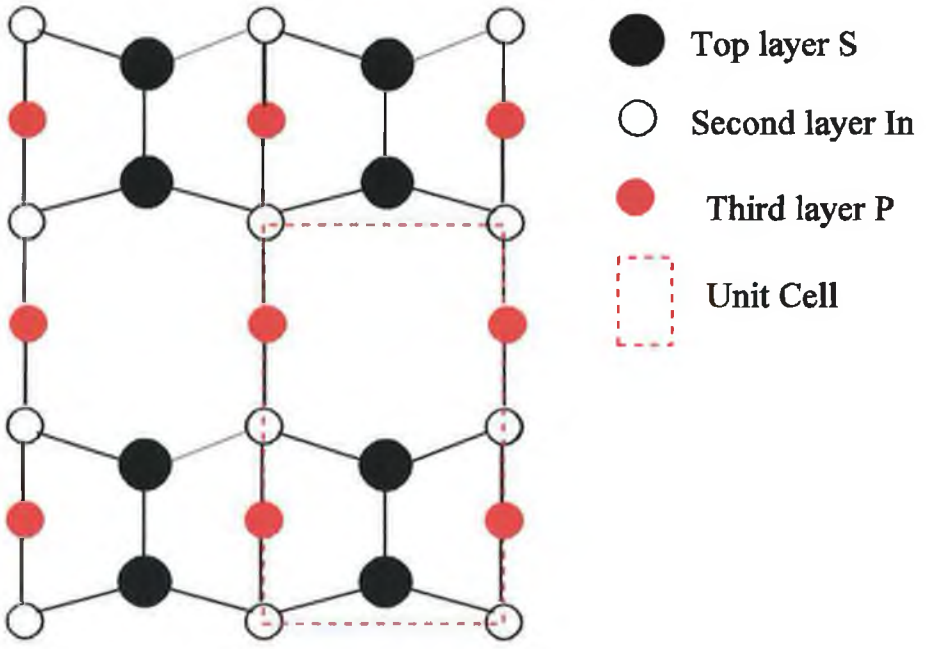

Figure 3.3 : Structural model for InP (100)-S (2x1), from Mitchell et al [7].

3.1.2 : Electron Counting Model

The electron counting model(ECM) [30] requires that the number of electrons in a semiconductor surface layer should occupy all the valence band dangling bond states and that all the conduction band dangling bonds should be empty. For the III-V semiconductors, the cation (In) sp^3 dangling bonds lie in the conduction band and the anion (P) sp^3 dangling bonds lie in the valence band. This condition will result in the surface having no net charge.

The ECM rule is applied to the InP(100)2x4 surface reconstruction using the 3 dimer/1 missing dimer model of figure 3.1. Figure 3.4 illustrates the procedure of equating the available electrons and the required electrons. Within this reconstruction there are 15 bonds each requiring 2 electrons and 6 lone pairs needing 2 electrons (dangling bonds), therefore this system requires 42 electrons. There are 6 P atoms which are pentavalent offering 30 electrons and 8 In atoms trivalently split between two bonds, thus each offering 1.5 electrons, i.e. 12 electrons. In total 42 electrons are available which satisfies the ECM rule.

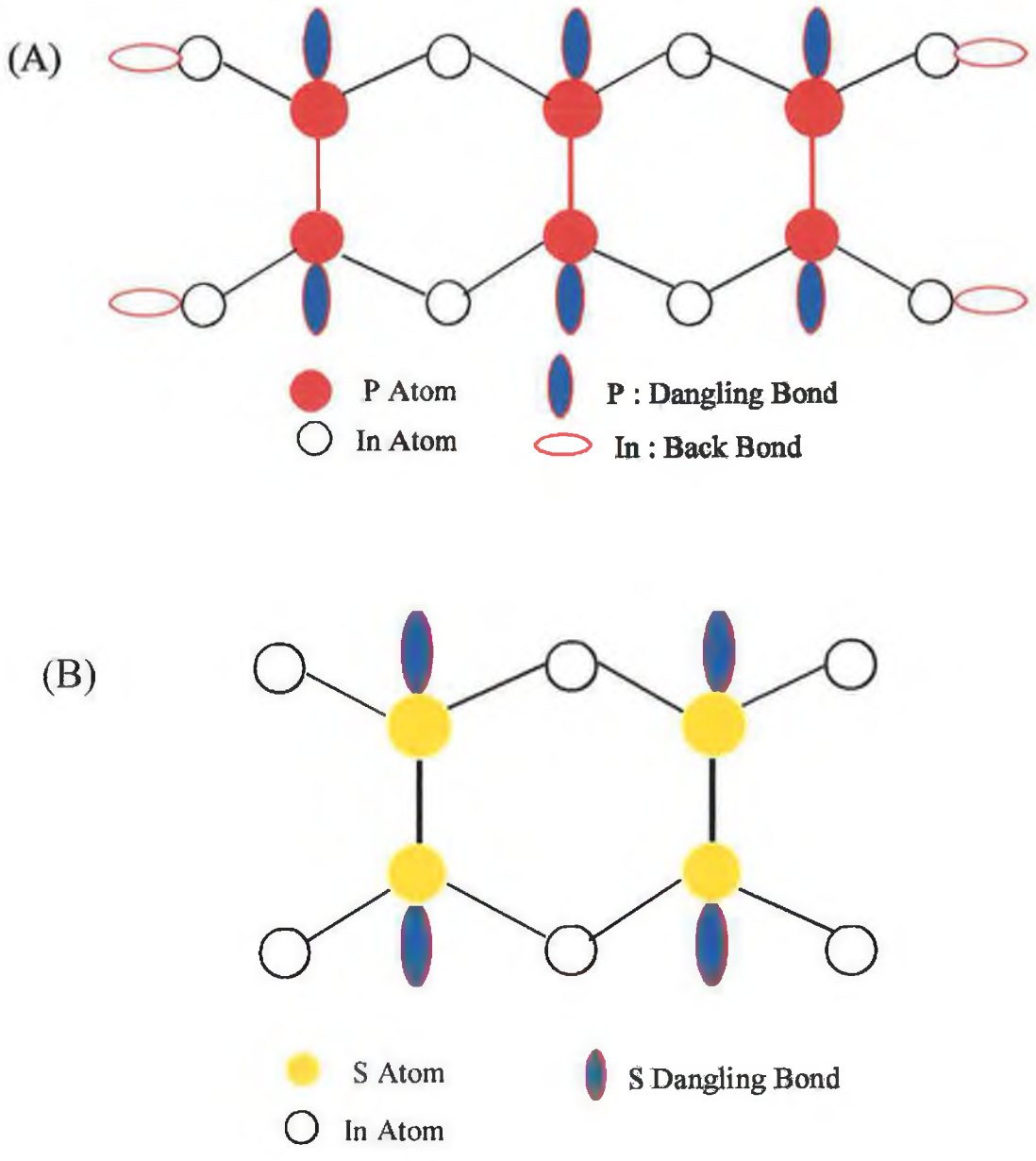

Figure 3.4 : Schematic illustrations applying the electron counting rule to both (A) InP(100)2x4 and (B) the InP(100)-S(2x1) reconstructions.

In the same manner the S terminated (2x1) reconstruction is treated with the ECM rule. There is no evidence of surface bands crossing the Fermi level from valence band studies, and as such the surface remains semiconducting and should satisfy the electron counting model. In applying the ECM to the (2x1) dimer surface reconstruction, shown in figure 3.3 there are 2 S atoms per surface unit cell and this structure requires 14 electrons, as both dangling bonds are full. Both S atoms offer 6 electrons each, i.e. 12 electrons and each of the 4 In atoms offer 3/4 of electron each, i.e. 3 electrons. In total there are 15 electrons available which is more than the 14 electrons required [5]. There is still no satisfactory explanation for the stability of the dimerised sulphur terminated InP or GaAs surfaces.

3.1.3 : Band Bending and Fermi Level Pinning

For a neutrally charged surface the 'neutral level' should be at the Fermi level (assuming that the Fermi-Dirac distribution is a step function). If states below this neutral level are empty, the surface has a net positive charge and if states above are full, then the surface has a net negative charge. Figure 3.5 illustrates band bending for an n-type Si (111) [31] surface where the bands bend upwards. The majority carrier concentration in the near surface region over which the bands are bent is less than in the bulk of the crystal. This region is known as the depletion region. On the other hand, where holes are the majority carrier (p-type) the surface is positively charged and downward band bending will occur, again decreasing the majority carrier concentration.

This surface induced band bending is primarily caused by surface states with energy levels within the bulk band gap. The associated bands within the gap are generally narrow and consequently the density of states at the surface is high. The high density of surface states ($\sim 10^{15}$-10^{16}/eV/cm^2) effectively pins the Fermi level as shown in figure 3.5. An n-type doped semiconductor with $\sim 10^{18}$ electrons/cm^3 may be estimated to have $\sim 10^{10}$ electrons/

cm^2 at the surface. The ratio of electrons at the surface to the density of surface states is given by [32]:

$$\frac{10^{10}\,\text{electrons}/\text{cm}^2}{10^{15}/\text{eVcm}^2} = 10^{-5}\,\text{eV}$$

Therefore the Fermi level does not penetrate far into the band of empty surface states. Thus the density of surface states and not the carrier density, dictates the surface Fermi level position. This effect is known as Fermi level pinning and leads to band bending reflecting the fact that the carrier concentration in the conduction band of the near surface region is significantly less than in the bulk. It also means that with the deposition of a metal onto this surface, charge transfer between the metal and the semiconductor would be to or from the surface states and the surface Fermi level position would remain unaltered, i.e. effectively pinned.

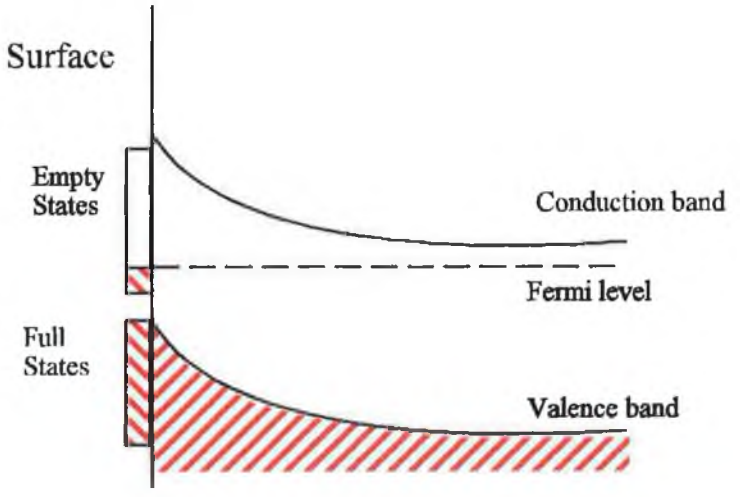

Figure 3.5 : Schematic illustration of the surface states on the n-type Si(111) surface and the induced band bending.

3.2 : Summary of Experimental Results

The deposition of thin layers of manganese and iron on sulphur terminated InP(100) surfaces has been investigated by soft x-ray core level photoemission. Clean InP(100) (2x4) surfaces were prepared by argon bombarding and annealing cycles. The sulphur treatment was carried out in-situ using an ultrahigh vacuum compatible electrochemical source as described in section 3.1.1. The Fermi level position for both n and p doped InP samples following sulphur deposition and anneal was found to lie in the range 1.1-1.2eV above the valence band maximum. These sulphur terminated surfaces displayed a clear (2x1) surface reconstruction with evidence of only In-S bonding at the surface. Thin layers of transition metals were subsequently deposited on these surfaces at room temperature. In both cases there is evidence of strong chemical interaction between the metal overlayers and the sulphur terminated surfaces which removes the (2x1) surface reconstruction and moves the Fermi level back towards a mid gap position for both doping types. In the case of the manganese layer, chemically shifted components of the In 4d and P 2p core levels diffuse out through the growing metal overlayer and the sulphur segregates to the top. Subsequent annealing cycles resulted in extensive chemical intermixing and a significant broadening of the interfacial region. In the case of the iron overlayer, chemically shifted components of the In 4d, P 2p and S 2p core levels are again observed which diffuse out through the growing metal overlayer producing a mixed chemical phase interfacial region. In neither case is there any evidence of heteroepitaxial growth at room temperature nor any indication that there is any significant suppression of chemical interactions at the interface.

3.3 : Experimental Introduction

The properties of thin magnetic films and particularly multilayer systems comprising of alternating layers of magnetic and non magnetic materials such as magneto-resistance and magnetic anisotropy have many potential industrial applications. These layers exhibit

different magnetic characteristic than the bulk due to interfacial or low dimensional effects [33].

The ability to grow abrupt thin magnetic films such as the transition metals, Fe and Mn on III-V semiconductors such as InP or GaAs has proven difficult with high degrees of inter-mixing occuring and thus the formation of disordered overlayers. Several studies [34-36] which investigated Fe on GaAs, have shown interdiffusion of the As with Fe and further surface segregation, finally resulting in the loss of magnetization of the grown Fe overlayer [36].

R.F.C Farrow [37] grew a Ag buffer layer on GaAs in an attempt to reduce the As-Fe interdiffusion, but the Ag buffer acts as an electrical shunt between the semiconductor and the magnetic overlayer. This led to other studies such as Al on S passivated GaAs [38] but more significantly to the study of Fe growth on S-passivated GaAs, in a similar attempt to reduce As diffusion and to preserve the magnetic characteristics of the thin Fe films [2, 3]. A monolayer of S was deposited to both electronically and chemically passivate the surface and subsequently acting as a surfactant to reduce the As interdiffusion as Fe is deposited. Anderson et al [2, 3] reported a clear ferromagnetic hysterises loop observed with the SMOKE (Surface Magneto Optic Kerr Effect) technique, demonstrating the retention of the magnetic characteristics after only 4 atomic layers. They suggest that the relatively successful inhibition of As interdiffusion may be a result of either S at the interface which is preferentially situated at defects and other active sites for As diffusion, or that S acts as a surfactant by holding the Fe onto the surface. Similar studies examining the growth of $CuInS_2$ on both Si (001) and (111) also used S passivation techniques to enhance the overlayer growth process [39, 40].

The present investigation examines in detail the chemical interactions at the surface. Both Fe and Mn, transition metals with magnetic characteristics were deposited to form ultra thin films on sulphur passivated InP(100). The study is a surface chemical analysis

using high resolution core-level photoemission spectroscopy XPS [41, 42].

3.4 : Experiment Details

InP(100) crystals, polished on one side (n and p = 4.4 x $10^{18}cm^{-3}$, Wafer Technology) were cleaned in-situ by three cycles of Ar bombarding (500eV and 2μA cm^{-2}) and annealing until a well defined (2x4) surface reconstruction was observed. The sulphur was deposited using a home built UHV compatible electrochemical Ag/AgI/AgS_2/Pt cell which preferentially emitted molecular sulphur [26-29]. The sulphur treated surface was subsequently annealed to approximately 300°C for 15min in order to obtain a clear (2x1) surface reconstruction. Manganese was deposited from high purity chips (99.98%) placed in a tungsten basket. Iron was deposited from an e-beam evaporator using a 1mm diameter wire of high purity. The metal deposition rate was determined by a thin film quartz thickness monitor. The experiments were performed on the 4.1 beamline at Daresbury synchrotron radiation laboratory. The resolution of the monochromator at 60eV, the photon energy used to probe the In 4d core level, was 200meV. The phosphorous 2p core level was excited by 170 eV photons, while 200eV was used for the S 2p thus ensuring that all photoelectrons had effectively the same kinetic energy and hence equivalent sampling depths. Movements of the Fermi level in the semiconductor bandgap for low metal coverages were monitored by measuring the position of the P 2p substrate core level peak and the valence band maximum relative to the metallic Fermi edge.

The core level spectra were curve fitted using a least squares fitting procedure which used spin-orbit split Voigt profiles. All core level spectra were acquired at normal emission and 60° off normal which allowed surface localised component peaks to be identified. The acceptance angle of the electron energy analyser was 14° which minimizes photoelectron diffraction effects in an angle dependent study. LEED was used to determine the surface structure of the clean and sulphur treated surfaces prior to metal deposition.

3.5 : Results and Discussion

The S-terminated InP(100) surface has been extensively investigated from structural [10-15], electronic [7, 16, 17, 43, 44] and surface chemistry [18-25] perspectives with several deposition procedures and techniques including ammonium sulphide based wet chemistry to H_2S gas and vacuum based elemental sulphur treatments. While discrepancies exist between different studies, sometimes with conflicting results, the structural and chemical model presented by Shimomura et al [45] who reported that the different surface reconstructions and chemical species identified in many of the previous studies can be correlated with the fraction of a S monolayer coverage on the surface.

3.5.1 : Manganese Deposition

There is almost a factor of two between the manganese lattice constant of .295nm and the .587 nm lattice constant of InP. The lattice mismatch between the substrate and the bcc Mn crystal structure is .5% with two Mn atoms for every substrate atom suggesting the possibility of epitaxial growth. Spectra for the n-type In 4d core levels at various stages in the experiment are shown in Figure 3.6. The clean surface spectrum consists of three components similar to the recent findings of Schmidt et al [46]. The assignment of the two surface components(In2 and In3) shifted by ±0.4eV with respect to the substrate peak was confirmed by an increase in intensity of these components relative to the substrate peak for the 60° off normal spectra. This three component fit for the In 4d clean surface spectrum was consistently reproduced for all five samples studied and is in contrast with the four component peak fit reported by Chab et al [24]and Shimomura et al [45] for the same surface. The reason for these differences in the clean surface structure are not clear but could be attributed to different sample preparation procedures. Following sulphur deposition and anneal at 300°C, the component peaks shift to lower kinetic energy and the surface components are replaced by a large chemically shifted component (In4) at 0.37eV

lower kinetic energy than the substrate peak (In1). The rigid shift of the component peaks to lower kinetic energy is consistent with a Fermi level shift reducing the clean surface band-bending. This assertion is supported by a comparable shift observed on the phosphorous 2p and the valence band maximum following sulphur deposition and anneal. This surface displayed the (2x1) surface reconstruction which corresponds to the much investigated sulphur terminated surface. The subsequent deposition of Mn leads to the appearance of a strong chemically shifted component (In5) at 0.85 eV higher kinetic energy which continues to increase in magnitude and ultimately becomes the sole In 4d component in the spectrum at a coverage of 1.1nm. This chemically shifted component is attributed to indium displaced from bonding with sulphur and phosphorous in the near surface region. In order to satisfactorily fit this component peak an asymmetric Doniach-Sunjic line shape is required which confirms its metallic nature. Figure 3.7 shows the corresponding spectra for the P 2p core level during the same experimental sequence. Again the clean surface spectrum consisting of a bulk and surface component is consistent with that reported by Schmidt et al [46]. Sulphur deposition and anneal results in a P 2p core level shift of 0.4eV to lower kinetic energy which becomes a single spin-orbit split component consistent with many other studies which found no evidence for sulphur - phosphorous bonding present on the (2x1) sulphur terminated surface. The deposition of 0.3nm Mn leads to the appearance of a chemically shifted component (P3) 0.35 eV to higher kinetic energy. At a coverage of 1.1nm Mn, where the In 4d substrate peak is completely attenuated, two chemically shifted components are observed in the P 2p spectrum. Neither of these components can be related to a substrate signal and therefore are assigned as P4 and P5. At a higher Mn coverage (not shown) the component labeled P5 completely dominates the spectrum.

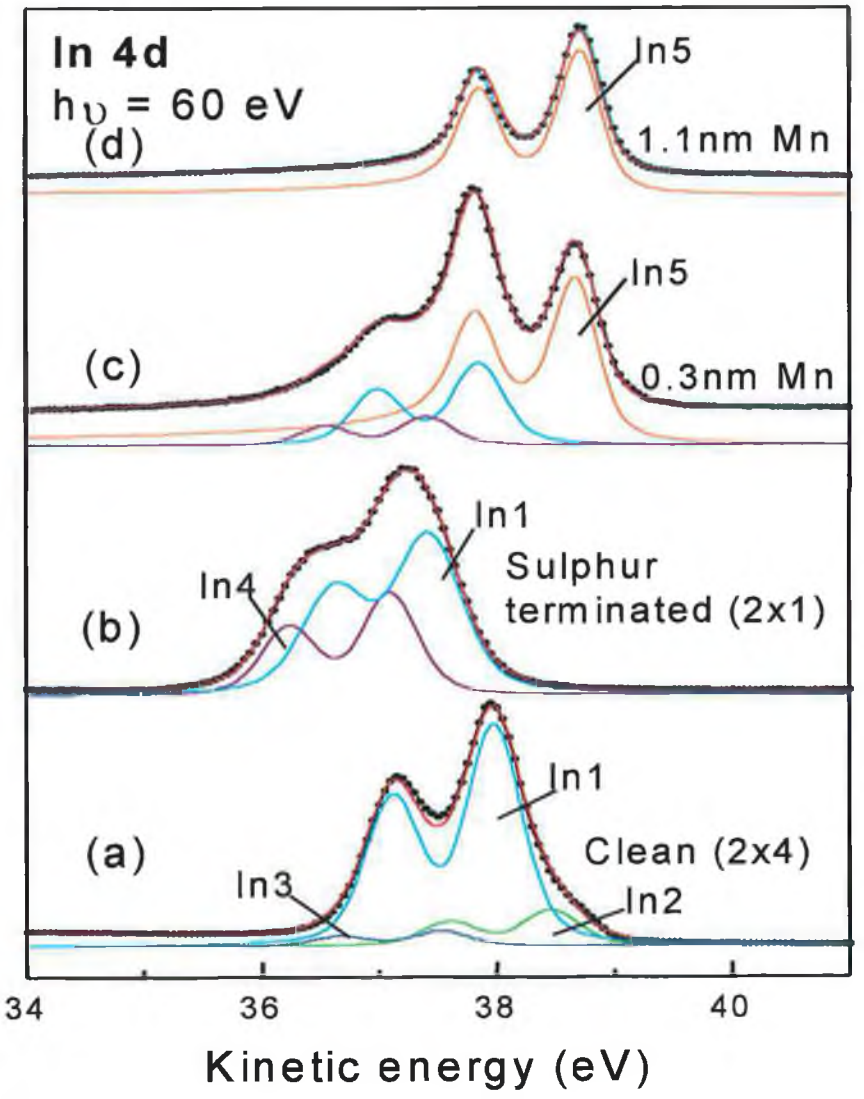

Figure 3.6 : In 4d core level spectra for a) clean InP (100) (2x4) surface, b)the sulphur terminated (2x1) surface reconstruction, c) after 0.3nm and d) 1.1nm Mn deposition.

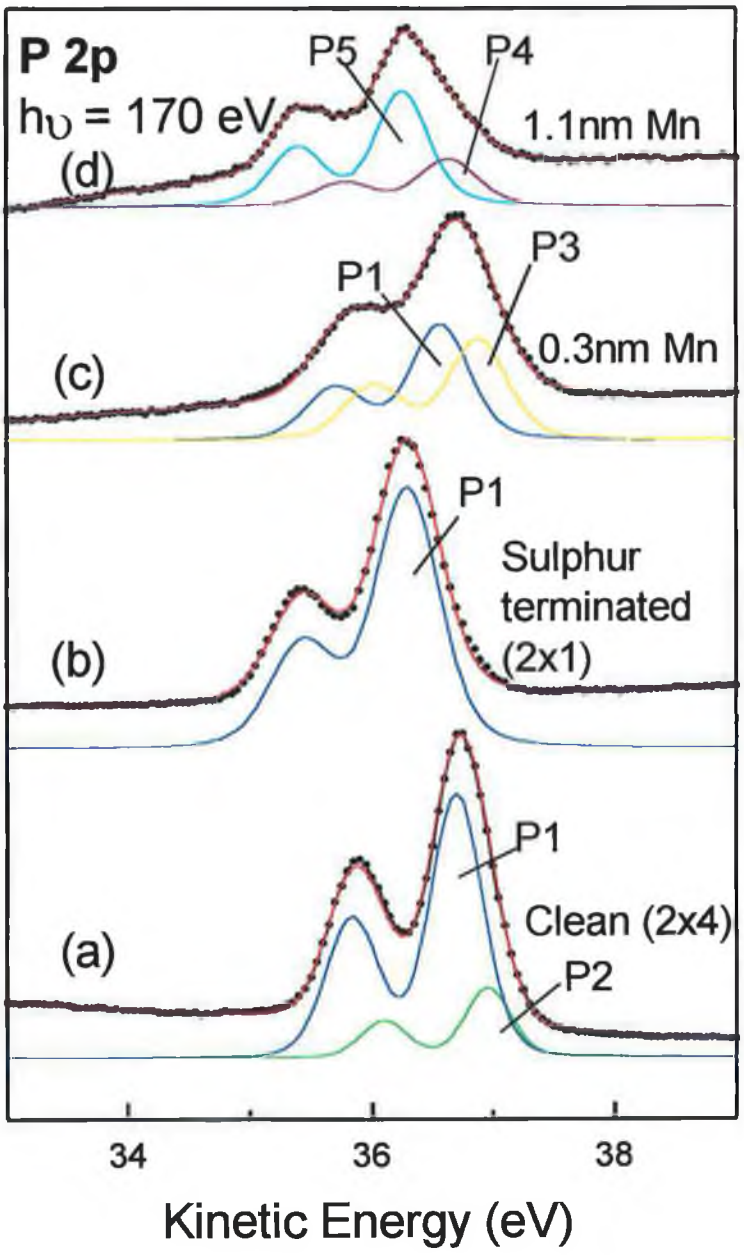

Figure 3.7 : P 2p core level spectra from a) clean InP(100) (2x4) surface, b) the sulphur terminated (2x1) surface reconstruction, after c) .3nm and d) 1.1nm Mn deposition.

The S 2p spectrum shown in Figure 3.8 for the (2x1) reconstructed surface shows clear evidence of two chemically shifted components separated by 0.5 eV. As stated in the introduction, this is consistent with the findings of Shimomura *et al* [45] who report that as the sulphur coverage approaches one monolayer, the sulphur 2p spectrum exhibits two distinct components. From the 60° off normal spectra taken prior to Mn deposition, we have consistently found that the higher kinetic energy peak (S1) is the more surface localised, which is also consistent with the findings of Shimomura *et al* [45]. Two component peaks are present in the S 2p spectra at low Mn coverages while at higher coverages (1.1nm), a single component persists.

The Mn coverage at which one P 2p chemically shifted component (P5) remains (not shown) corresponds to the same coverage at which the S 2p peak is a single component and the In 4d signal is dominated by the lower binding energy component attributed to a metallic In signal. At this same coverage, the Mn 3p peak (not shown) shifts to lower binding energy and this is interpreted as meaning that at this coverage, the substrate InP signal has been completely attenuated and that all three elements subsequently observed, In, P and S have diffused out into the manganese overlayer. This indicates that there is substantial disruption of the sulphur terminated surface following Mn deposition. The fact that a strong chemically shifted component appears on the P 2p core level, which was effectively bulk coordinated on the (2x1) surface, demonstrates that the sulphur layer is displaced by the deposited manganese. By comparing the thermodynamic data for heats of compound formation for InS (+0.16eV) and MnS(-0.66eV) it is clear that Mn would be expected to strongly interact with the deposited sulphur layer. In fact, the spectra for both In 4d and P 2p throughout the experimental sequence described indicate that complex chemical interactions occur at this interface which substantially disrupt the InP surface and makes precise assignment of the component peaks very difficult. Identical chemical

interactions were obtained for the p-type InP sample and therefore the spectra are not shown here.

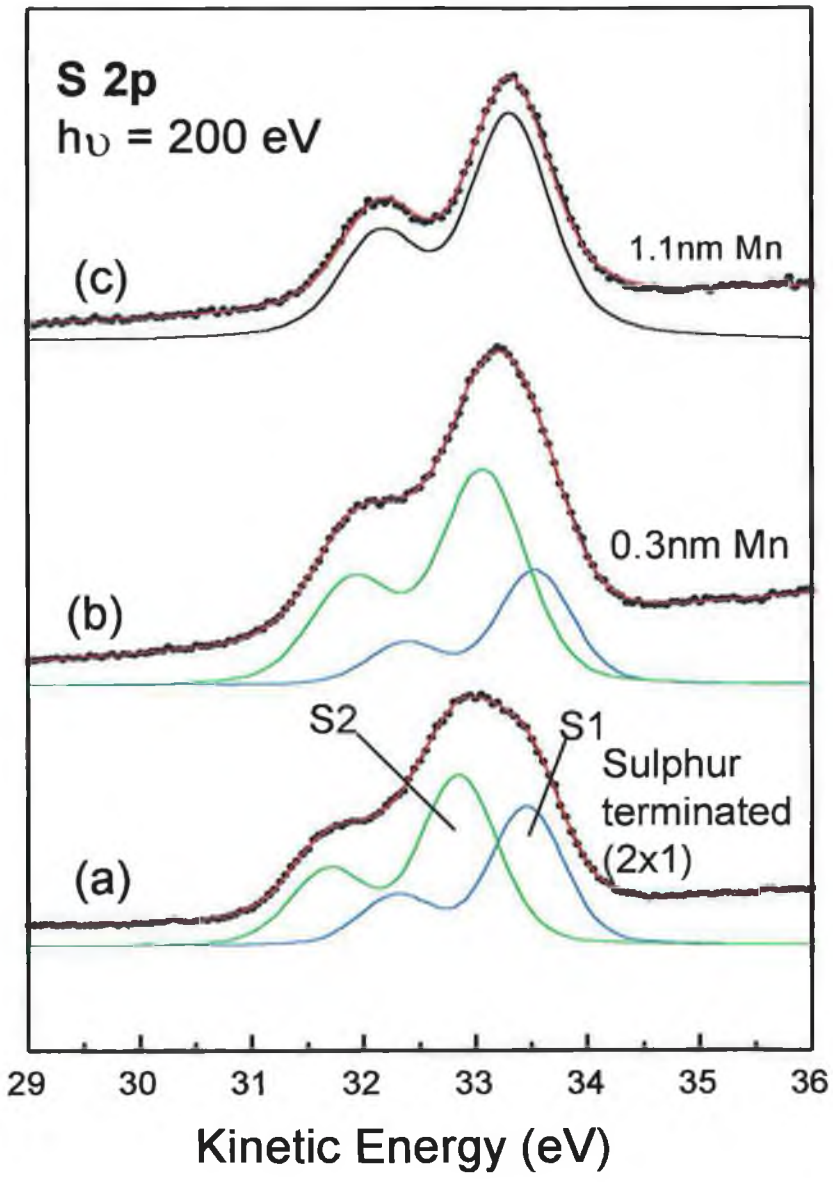

Figure 3.8 : S 2p core level of the S-terminated (2x1) surface, after a) .3nm and c) 1.1nm Mn deposition.

The movements of the Fermi level for both doping types following the deposition and anneal of sulphur and the first deposition of Mn are shown in Figure 3.9. The clean surface Fermi level position for both n and p samples is found to reside in the bottom half of the band gap, 0.5 -0.6 eV above the valence band maximum (VBM). Other clean surface samples investigated, (both n and p doped) showed a variation in the position of the Fermi energy in the lower half of the band gap of the order of 0.25 eV, but consistently below the mid gap position. The movement of the Fermi level following sulphur deposition and anneal for both n and p type samples was toward the top of the band gap to a position 1.0eV -1.2 eV above the VBM. While this corresponds to a considerable degree of band flattening for the n-type sample, it results in the inversion of the p-type sample. This behavior has been previously observed [20, 23, 44] and throws considerable doubt on whether the Fermi level movement in the case of the n-type sample corresponds to the conventional idea of surface passivation, i.e. the removal of surface states in the band gap, or simply to a re-establishment of the Fermi level pinning position closer to the conduction band. The results for the p-type sample would suggest that the latter explanation is more consistent with the experimental facts. A similar observation has been recently made in the case of the sulphur deposition and anneal on both n and p-type GaAs(100) surface [47]. This is not to say that the sulphur treatment doesn't reduce the density of defect states in the InP band gap, but simply that the band flattening observed for n-type samples may be mis-interpreted as indicating a complete removal of band gap states rather than a re-establishment of the Fermi level pinning position closer to the conduction band minimum.

Following the first deposition of Mn (0.03nm), the Fermi level moves back towards a mid gap position, but subsequent movements become impossible to follow at higher coverages due to the extent of the changes induced in the shape of the substrate core levels by the strong chemical interactions.

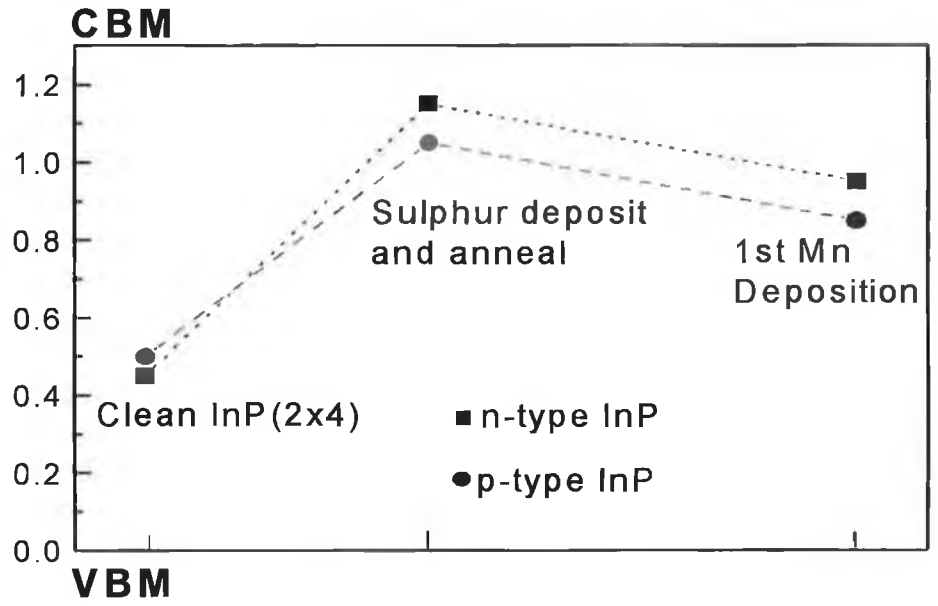

Fig. 3.9 : Fermi level movements in the InP(100) band gap for both n and p-InP as a function of sulphur and metal deposition.

The surface structural order was lost with the Mn deposition as no LEED pattern was observed. After a total of ~1.9nm Mn deposition the samples were subsequently annealed at between 300°C and 400°C in order to determine whether this treatment would result in the formation of an ordered overlayer. The In 4d core level spectra shown in figure 3.10 illustrate the dramatic effect of these annealing cycles on the chemistry of the overlayer. The appearance of two broadened chemically shifted components at lower kinetic energy which alter position as a function of annealing temperature, indicates significant chemical intermixing between the Mn overlayer and the underlying InP substrate. This interaction effectively broadens the width of the mixed chemical phase region between the InP substrate and the metal overlayer. Similar evidence of strong chemical interactions and peak broadening are obvious from the P 2p spectra shown in figure 3.11 where two distinct components can be resolved following a 300°C anneal for 15 minutes. The intensity

of both the In 4d and P 2p core levels increase as a function of annealing temperature while the intensity of the S 2p, shown in figure 3.12 decreases. The single component S 2p peak moves 0.4 eV to higher kinetic energy upon anneal and this coupled with the decrease in signal intensity suggests that the surface segregated sulphur chemically reacts with the Mn overlayer forming MnS, consistent with the thermodynamic data presented earlier. Annealing at 400°C further promotes the chemical interactions in the interfacial region.

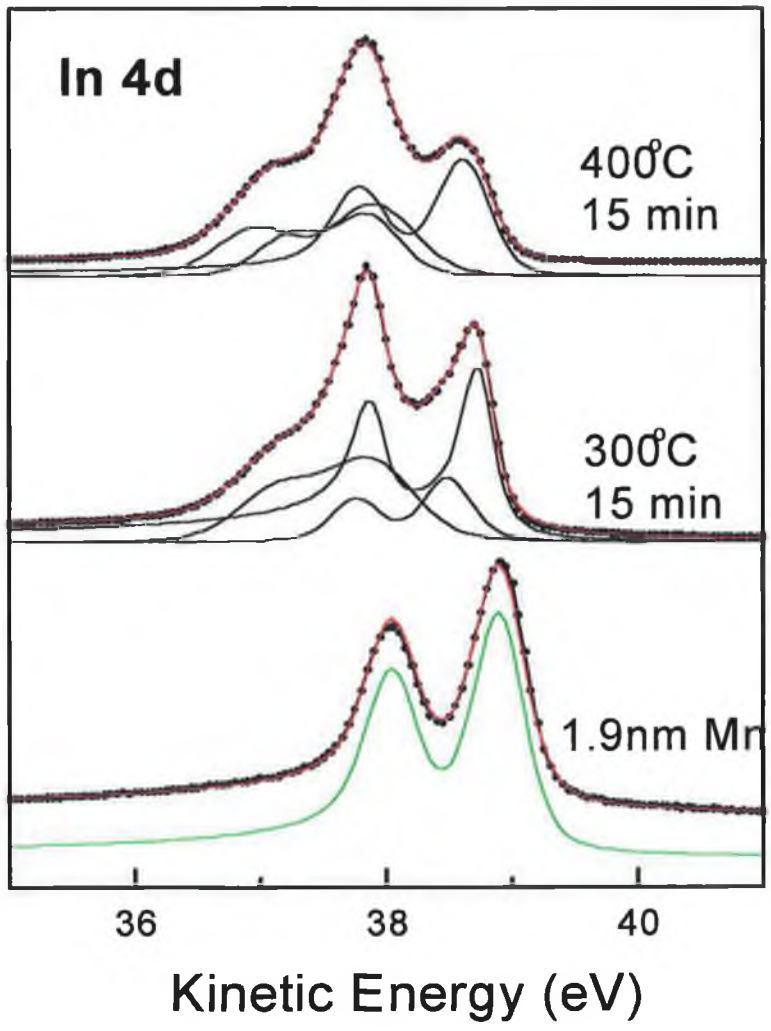

Figure 3.10 : In 4d core level spectra as a function of annealing temperature.

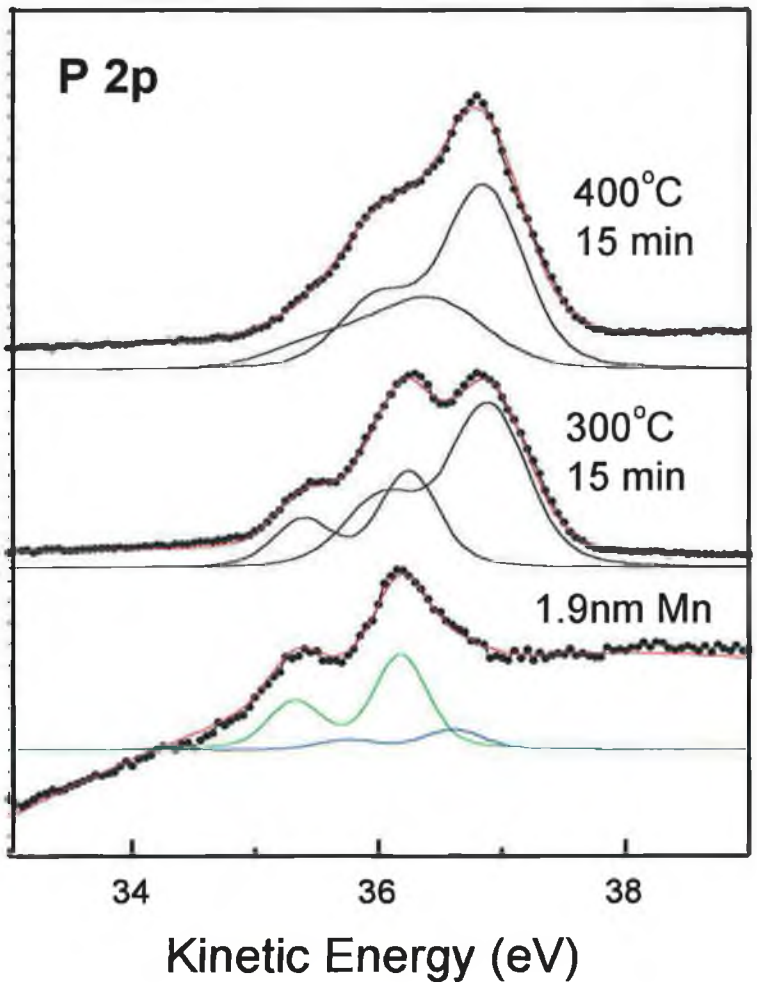

Figure 3.11 : P 2p core level spectra as a function of annealing temperature

The complex nature of the interfacial chemistry from the annealing cycles makes it difficult to unambiguously interpret the core level spectra. Although it is clear that the annealing results in a significant broadening of the interfacial region between the InP and the Mn overlayer and indicates vigorous intermixing across the metal semiconductor interface.

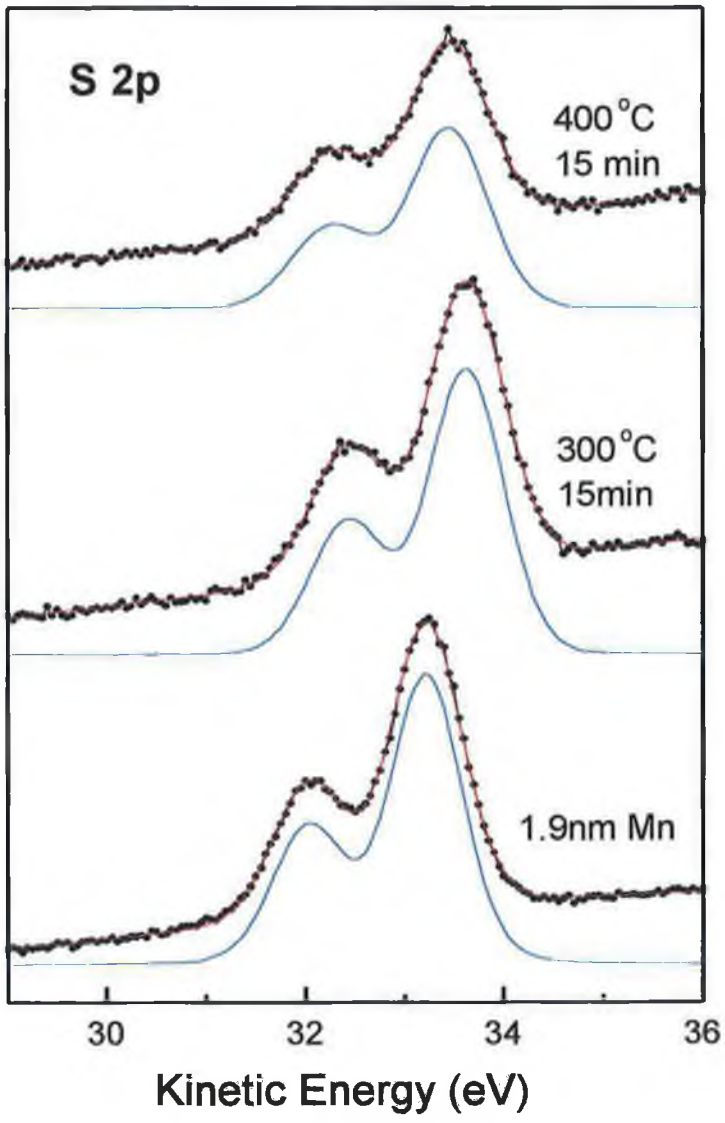

Figure 3.12 : S 2p core level spectra as a function of annealing temperature.

3.5.2 : Iron Deposition

The lattice mismatch between the .587nm of InP and .286nm of the bcc Fe crystal structure is 2.4% with two Fe atoms for every substrate atom. Spectra for the n-type In 4d at various stages in the experiment are shown in figure 3.13. As previously discussed the clean surface spectrum consists of three spin-orbit split component peak. The two components labelled In2 and In3 shifted by ±0.4eV with respect to the substrate peak were confirmed as surface peaks by off normal detection. The sulphur deposition and anneal at 300°C, resulted in complete peak shifts to lower kinetic energy, corresponding to a Fermi level shift, and the surface components are replaced by a large chemically shifted component labelled In4 at 0.35eV lower kinetic energy than the substrate peak. The sulphur terminated surface displayed the (2x1) surface reconstruction as discussed. The subsequent deposition of Fe leads to the appearance of a strong chemically shifted component (In5) at 0.7eV higher kinetic energy which continues to increase in magnitude until it dominates the In 4d spectrum at a coverage of 1.6nm. This chemically shifted component, which is fitted with an asymmetric Doniach-Sunjic line shape, is attributed to indium released from bonding with phosphorous which acquired metallic character as it diffuses out through the Fe overlayer.

Figure 3.14 shows the corresponding spectra for the P 2p core level during the same experimental sequence. Sulphur deposition and anneal result in the P 2p core level shifting to lower kinetic energy and becoming a single spin-orbit split component consistent with many other studies which found no evidence of sulphur - phosphorous bonding present on the (2x1) sulphur terminated surface. The deposition of Fe leads to the appearance of a chemically shifted component labelled P2, at 0.75 eV to lower kinetic energy. These two components remain present in the spectrum until at higher Fe coverage (1.6nm) the P 2p signal is completely attenuated, while an In 4d component peak persists.

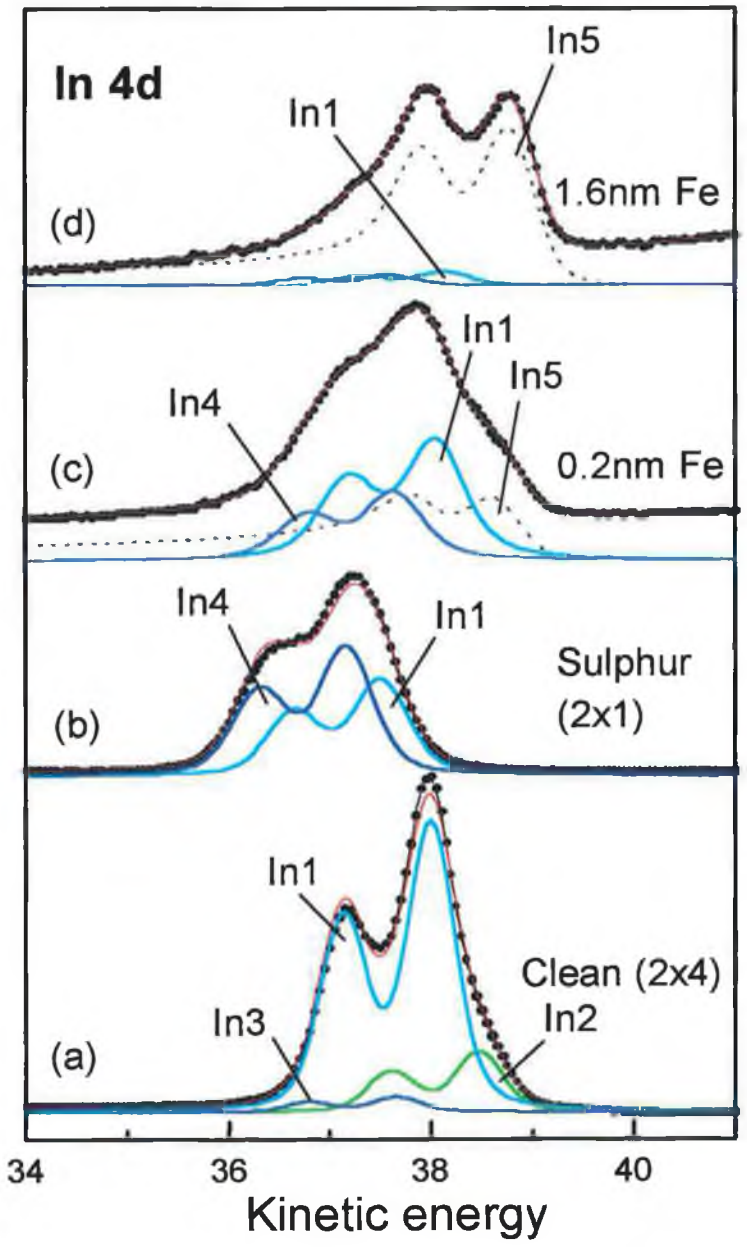

Figure 3.13 : In 4d core level spectra from a) clean (100)(2x4) surface, b) the S-terminated (2x1) surface reconstruction, and following c).2nm and d) 1.6nm deposition of iron.

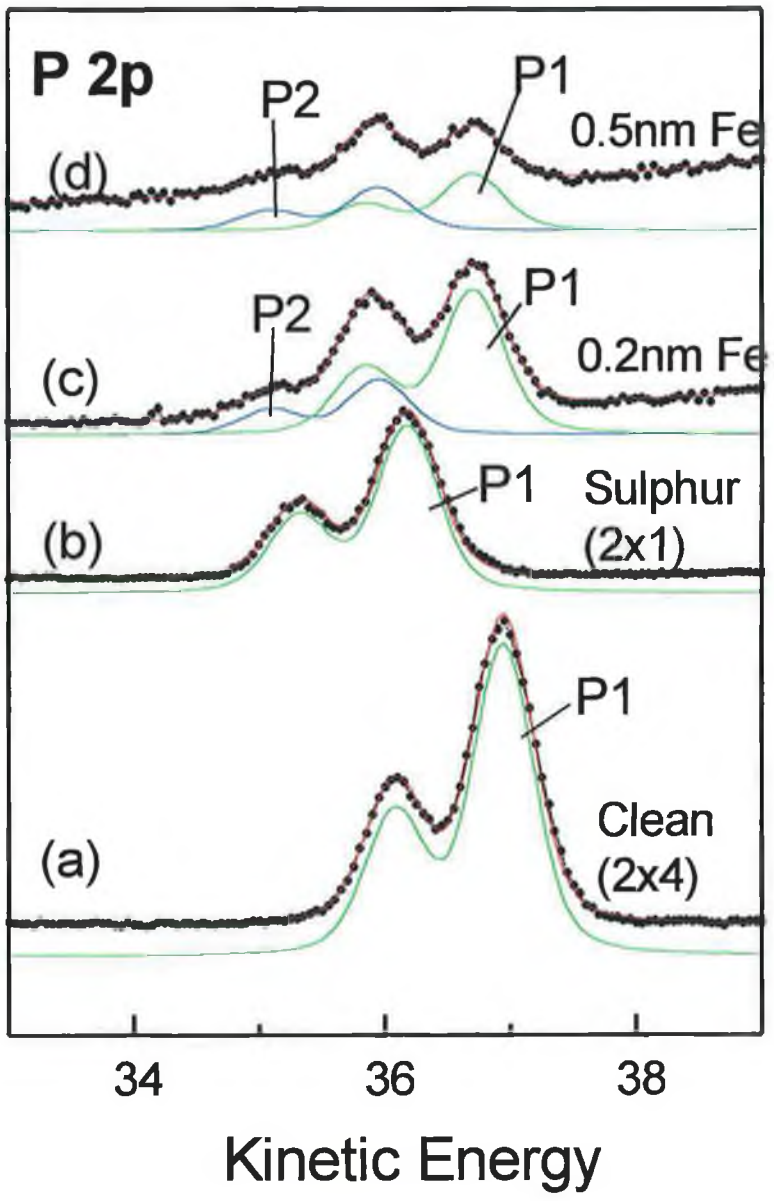

Figure 3.14 : P 2p core level spectra from a)clean (100)(2x4) surface, b) the S-terminated (2x1) surface reconstruction, and following c).2nm and d) .5nm deposition of iron.

The P 2p chemically shifted component in figure 3.14 labelled P2 has a slower attenuation rate than the substrate peak, indicating that this component is diffusing out through the growing metal overlayer. Off normal spectra confirmed the surface localisation of the chemically shifted component.

Figure 3.15 shows, as previously discussed, the S 2p core level of the reconstructed (2x1) sulphur terminated surface with two chemically shifted components and then as a function of metal coverage. The core level studies indicate that there is substantial disruption of the sulphur terminated surface following Fe deposition. The fact that a strong chemically shifted component appears on the P 2p core level, which was effectively bulk co-ordinated on the (2x1) surface, demonstrates that the sulphur layer is displaced by the depositing iron which chemically reacts with the phosphorous. At a coverage of 1.6 nm Fe at which the P 2p signal has been totally attenuated, the metallic In 4d and S 2p signals still persist indicating that In and S have diffused out into the iron overlayer. The overall trend of the chemical interactions as described are similar to those reported by Hohenecker et al [47] for the core level studies of the interaction of magnesium with sulphur terminated GaAs(100) surface. They also observed significant evidence of chemical intermixing at the interface including interaction between the Mg and the substrate As component.

Identical results were obtained for the p-type InP sample and therefore the spectra are not shown here. The movements of the Fermi level for both doping types following the deposition and anneal of sulphur and the first deposition of Fe are shown in figure 3.16. As previously discussed the clean surface Fermi level position for both n and p samples is found to reside in the middle of the band gap, 0.6 -0.75 eV above the valence band maximum (VBM). The movement of the Fermi level following sulphur deposition and anneal for both n and p type samples was toward the top of the band gap to a position approximately 1.1-1.2 eV above the VBM.

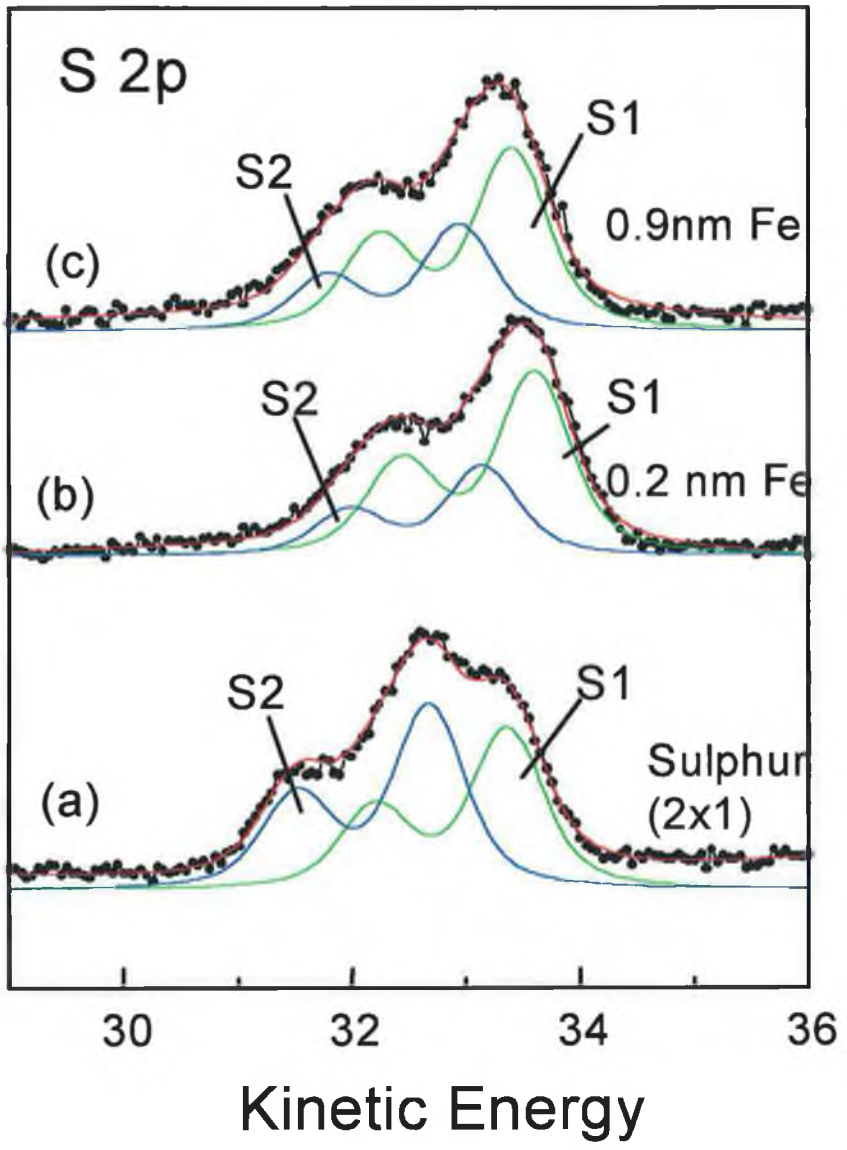

Figure. 3.15 : S 2p core level spectra for the a) (2x1) S-terminated surface and following b).2nm and c).9nm Fe deposition.

These results correspond to the results found with the Mn deposition experiment in that they cast doubt on whether the Fermi level movement, in the case of the n-type sample corresponds to the conventional idea of electronic passivation i.e. the removal of surface states in the band gap due to the occupation of dangling bonds by adatoms.

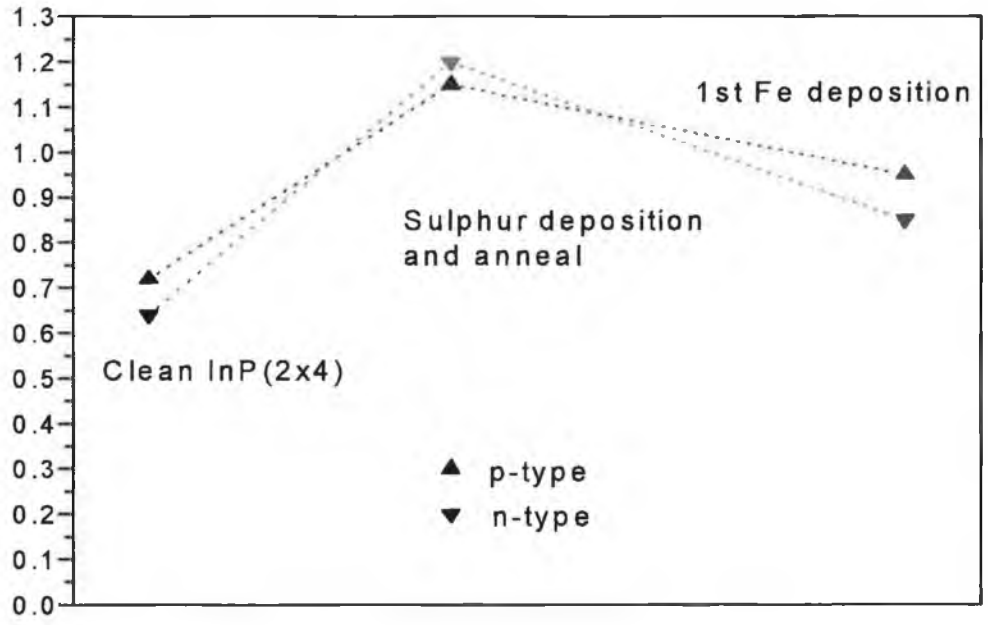

Figure 3.16 : Fermi level movements in the InP(100) band gap for both n and p-InP as a function of sulphur and metal deposition.

Following the first deposition of Fe (0.1nm), the Fermi level moves back by approximately 0.3 eV towards a mid gap position and the (2x1) LEED pattern of the sulphur terminated surface disappears. There is no significant additional movement of the Fermi level for subsequent metal coverages. Following the final Fe deposition (1.6nm), no LEED pattern was observed. There is no evidence of heteroepitaxial iron growth for Fe deposition at room temperature nor was there any indication that the extent of the chemical interactions at the interface were any less than would be observed for iron deposition on a

III-V semiconductor without a sulphur layer present. Indeed, the picture of the interfacial region which emerges from this study is of extensive chemical intermixing and the preferential out diffusion of indium and sulphur into the growing metal overlayer.

3.6 : Conclusions

From these parallel studies of the interaction of both thin Mn and Fe layers deposited onto the sulphur terminated InP(100) surface, it is apparent that very similar changes were induced in the Fermi level position by the deposition of metals with quite different workfunctions (Mn 3.83 eV and Fe 4.31 eV). Both deposition procedures showed evidence of chemical interaction between the growing metal overlayer and the substrate. This suggests that it is the chemical interactions which dictate the Fermi level movements. Metal deposition results in the removal of the sulphur induced (2x1) surface reconstruction and a corresponding movement of the Fermi level back towards a mid gap position for both n and p-type samples. We therefore propose that it is the (2x1) surface reconstruction which is responsible for the Fermi level being positioned close to the CBM for both n and p-type samples, and not sulphur doping of the near surface region which has been previously suggested. Once this reconstruction is removed by depositing a 0.1 nm coverage of metal, the Fermi level moves back towards a mid gap position, suggesting that the induced chemical interactions may not remove any sulphur from the near surface region, but significantly alters the local surface structure.

These studies have primarily shown the deposition of Mn and Fe on sulphur terminated InP(100) to result in strong chemical interactions at the interface. No significant suppression of the chemical interactions resulted from the S-termination of the substrate and there is no evidence of epitaxial growth.

3.7 : References

1. Malhotra, V. and C.W. Wilmsen, *Passivation of GaAs and InP*, in *Handbook of Coumpound Semiconductors : Growth Processes and devices.*, P.H. Holloway and G.E. McGuire, Editors. 1989.
2. Anderson, G.W., M.C. Hanf, and P.R. Norton, *Growth and Magnetic Properties of Epitaxial Fe (100) on S-Passivated GaAs (100).* Phys. Rev. Lett., 1995. **74**(14): p. 2764.
3. Anderson, G.W., *et al.*, *Epitaxial Growth of Fe on Sulphur -Passivated GaAs(100) a method for preventing As interdiffusion.* Surface Science, 1995. **346**: p. 145.
4. Biegelson, D.K., *et al.*, *Surface Reconstructions of GaAs(100) observed with Scanning Tunneling Microscopy.* Phys. Rev. B, 1990. **41**: p. 5701.
5. MacPherson, C.D., *et al.*, *Scanning Tunneling Study of InP(100)-2x4: An exception to the Dimer Model.* Phys. Rev. Lett., 1996. **77**(4): p. 691.
6. Sung, M.M., *et al.*, *Composition and morphology of InP(100) surfaces as a function of low energy Ar bombardment and annealing.* Surface Science, 1997. **382**: p. 147.
7. Mitchell, C.E.J., *et al.*, *Sulfur passivated InP(100): surface gaps and electron counting.* Appl. Surface Science., 1996. **104/105**: p. 434.
8. Xue, Q.K., T. Hashizume, and T. Sakarai, *Scanning Tunneling Microscopy of III-V Compound Semiconductor (001) Surfaces.* Progress in Surface Science, 1997. **56**(1-2).
9. Monch, w., *Semiconductor Surfaces and Interfaces.* 1995.
10. Tian, Z., *et al.*, *Core-level spectroscopy study of the evolution of the sulfur-passivated InP(001)surface duing annealing.* Phys. Rev. B, 1997. **55(8)**: p. 5376.
11. Qin, X.R., *et al.*, *Surface morphology of ex situ sulfur-passivated (1x1) and (2x1) InP (100) surfaces.* J. Vac. Sci. Technol., 1998. **A16(1)**: p. 163.

12. Warren, O.L., *et al.*, *Structural determination of the S-passivated InP(100)-(1 x 1) surface by dynamical low-energy electron-diffraction analysis.* Phys. Rev. B, 1995. **52(4)**: p. 2925.

13. Lu, Z.H., *et al.*, *S-passivated InP (100)-(1×1) surface prepared by a wet chemical process.* Appl. Phys. Lett., 1992. **60**: p. 2669.

14. Jin, J.-M., *et al.*, *Stabilization of face-centered-cubic Mn films via epitaxial growth on GaAs(001).* Phys. Rev. Lett., 1995. **75(5)**: p. 878.

15. Shimomura, M., *et al.*, *Surface structures and electronic states of H_2S-treated InP(001).* J. Appl. Phys., 1996. **79(8)**: p. 4193.

16. Iyer, R., R.R.Chang, and D.L.Lile, *Sulfur as a surface passivation for InP.* Appl. Phys. Lett., 1988. **59(4)**: p. 134.

17. Kapila, A. and V.Malhotra, *Passivation of the InP surface using polysulfide and silicon nitride overlayer.* Appl. Phys. Lett., 1993. **62(9)**: p. 1009.

18. Tao, Y., *et al.*, *S-passivated InP (100)-(1 x 1) surface prepared by a wet chemical process.* Appl. Phys.Lett, 1992. **60(21)**: p. 2669.

19. Gallet, D. and G.Hollinger, *Chemical, structural, and electronic properties of sulfur-passivated InP(001) (2×1) surfaces treated with (NH4)2Sx.* Appl. Phys. Lett., 1993. **62(9)**: p. 982.

20. Kwok, R.W.M. and W.M.Lau, *X-ray photoelectron spectroscopy study on InP treated by sulfur containing compounds.* J.Vac. Sci. Technol., 1992. **A10(4)**: p. 2515.

21. Maeda, F., Y.Watanabe, and M.Oshima, *Surface chemical bonding of (NH4)2Sx-treated InP(001).* Appl. phys. Lett., 1993(62(3)): p. 297.

22. Fukuda, Y., *et al.*, *$(NH_4)_2 S_x$ -treated InP(001) studied by high-resolution x-ray photoelectron spectroscopy.* J. Appl. Phys., 1994. **76(5)**: p. 3059.

23. Streubel, P., *et al.*, Surf. Inter. Anal., 1995. **23**: p. 581.

24. Chab, V., *et al.*, *Soft X-ray photoemission studies of S/InP(100).* Surf. Sci., 1997. **377-379**: p. 261.

25. Han, I.K., *et al.*, *Stability of sulfur-treated InP surface studied photoluminescence and x-ray photoelectron spectroscopy.* J. Appl. Phys., 1997. **8(10)**: p. 6986.

26. Roberts, L., *et al.*, *Vacuum Ultraviolet photoelectron spectroscopy study of the interaction of molecular sulfur with the GaAs (100) surface.* J. Vac. Sci. Technol., 1992. **B**(10(4)): p. 1862.

27. Davies, G.J., D.A. Andrews, and R. Heckingbottom, *Electrochemical sulfur doping of GaAs grown by molecular beam epitaxy.* J. Appl. Phys., 1981. **52**: p. 822.

28. Heegemann, W., *et al.*, Surface Science, 1975. **49**: p. 161.

29. Wagner, C., J. Chem. Phys, 1953. **21**: p. 1819.

30. Pashley, M.D., *Electron Counting Model and its application to island structures on molecular-beam epitaxy grown GaAs(001) and ZnSe(001).* Phys. Rev. B, 1989. **40**(15): p. 10481.

31. Zangwill, A., *Physics at surfaces.* 1987: Cambridge University Press.

32. Yu, P.Y. and M. Cardona, *Fundamentals of Semiconductors.* 1995: Springer.

33. Heinrich, B. and J.A.C. Bland, *Ultrathin Magnetic Structures Volume I and II.* 1993.

34. Waldrop, J.R. and R.W. Grant, *Interface chemistry of metal-GaAs Schottky-barrier contacts.* Appl. Phys. Lett, 1979. **34**: p. 630.

35. Chambers, S.A., *Simultaneous epitaxy and substrate out-diffusion at a metal-semiconductor interface: Fe/GaAs(001)-c(8 x 2).* Phys Rev. B, 1986. **34**: p. 6605.

36. Krebs, J.J., B.T. Jonker, and G.A. Prinz, *Properties of Fe single-crystal films grown on (100)GaAs by molecular-beam epitaxy.* J. Appl. Phys, 1987. **61**: p. 2596.

37. Farrow, R.F.C., S.S.P. Parkin, and V.S. Speriousu, Jap. Jrnl. Appl. Phys., 1988. **64**:

p. 5315.

38. Oigawa, H., *et al.*, Jpn. J. Appl. Phys, 1990. **29**(L544).

39. Metzner, H., *et al.*, *Epitaxial growth of CuInS2 on sulphur terminated Si(111).* Appl. Phys. Lett, 1996. **69**(13): p. 1900.

40. Hahn, T., *et al.*, *Epitaxial growth of CuInS2 on sulphur terminated Si(001).* Appl. Phys. Lett., 1998. **72**(21): p. 2733.

41. Hughes, G.J., *et al.*, *Core level photoemission study of the deposition of thin iron layers on sulphur terminated InP(100)surfaces.* Applied Surface Science, 1999. **147**: p. 201.

42. Hughes, G.J., *et al.*, *Core level photoemission study of the deposition of thin Mn layers on sulphur terminated InP(100)surfaces.* Surface Science, 1999. **431**: p. 1.

43. Iyer, R. and a. D.L.Lile, *Role of polysulfides in the passivation of the InP surface.* Appl. Phys. Lett., 1991. **59(1)**: p. 437.

44. Nelson, A.J., S.P. Frigo, and R. Rosenberg, *Surface type conversion of InP by H2S plasma exposure: A photoemission investigation.* J. Vac. Sci. Technol, 1993. **A11(4)**: p. 1022.

45. Shimomura, M., *et al.*, *Surface reconstruction of InP(100) upon adsorption of H_2S studied by LEED, STM, HREELS, and XPS.* J. Appl. Phys, 1998. **83(6)**: p. 3071.

46. Schmidt, W.G., *et al.*, *Atomic Structure of InP(100): A dimer reconstruction.* Phys. Rev. B, 1998. **57(23)**: p. 14596.

47. Hohenecker, S.T., T.U.Kampen, and D.R.T.Zahn, *Influence of sulfur interlayers on the Mg/GaAs(100) interface formation.* J. Vac. Sci. Technol., 1998. **B 16 (4)**: p. 2317.

Chapter 4

Surface Electronic States of clean GaN

4.1 : General Introduction

Binary nitride semiconductors AlN, GaN and InN all have direct band gaps which range from 1.9eV through 3.4eV to 6.2eV respectively and have the potential to form a complete series of ternary alloys producing light emitting devices with emission spanning the visible and into the UV region, i.e. from 650nm to 200nm. The current and potential engineering applications are well known, primarily the sought after blue and green LEDs and laser diodes [1-3].

4.1.1 : GaN Structure

Gallium nitride and its related compounds crystallize both in zinc-blende and wurtzite structures. The electronic structure of both phases is similar, and the crystal structures are also closely related as the next neighbour bonding is tetrahedral. The Bravais lattice of the wurtzite structure is hexagonal and the axis perpendicular to the hexagons is labeled the c-axis. Figure 4.1 shows a clinographic projection of the wurtzite structure along with the associated bulk and surface Brilloiun zones which are both hexagonal. The lattice constants are also given in the figure 4.1. The difference between zinc-blende and wurtzite structures may be demonstrated within their respective stacking sequences along the c-axis. For zincblende : $Ga_{(A)}N_{(A)}Ga_{(B)}N_{(B)}Ga_{(C)}N_{(C)}Ga_{(A)}N_{(A)}Ga_{(B)}N_{(B)}Ga_{(C)}N_{(C)}$.; and for wurtzite : $Ga_{(A)}N_{(A)}Ga_{(B)}N_{(B)}Ga_{(A)}N_{(A)}Ga_{(B)}N_{(B)}$.... . Both are polar crystal forms, with either an all Ga or N face, the bulk structure will have a corresponding Ga or N polarity.

While the wurtzite structure is far the more common of the two phases, the cubic zinc-blende structure still holds considerable potential interest. Theoretical calculations suggest that cubic p-type GaN should produce very high conductivities and have also

suggested that the optical gain in cubic quantum wells may be higher than in the wurtzite structure [2].

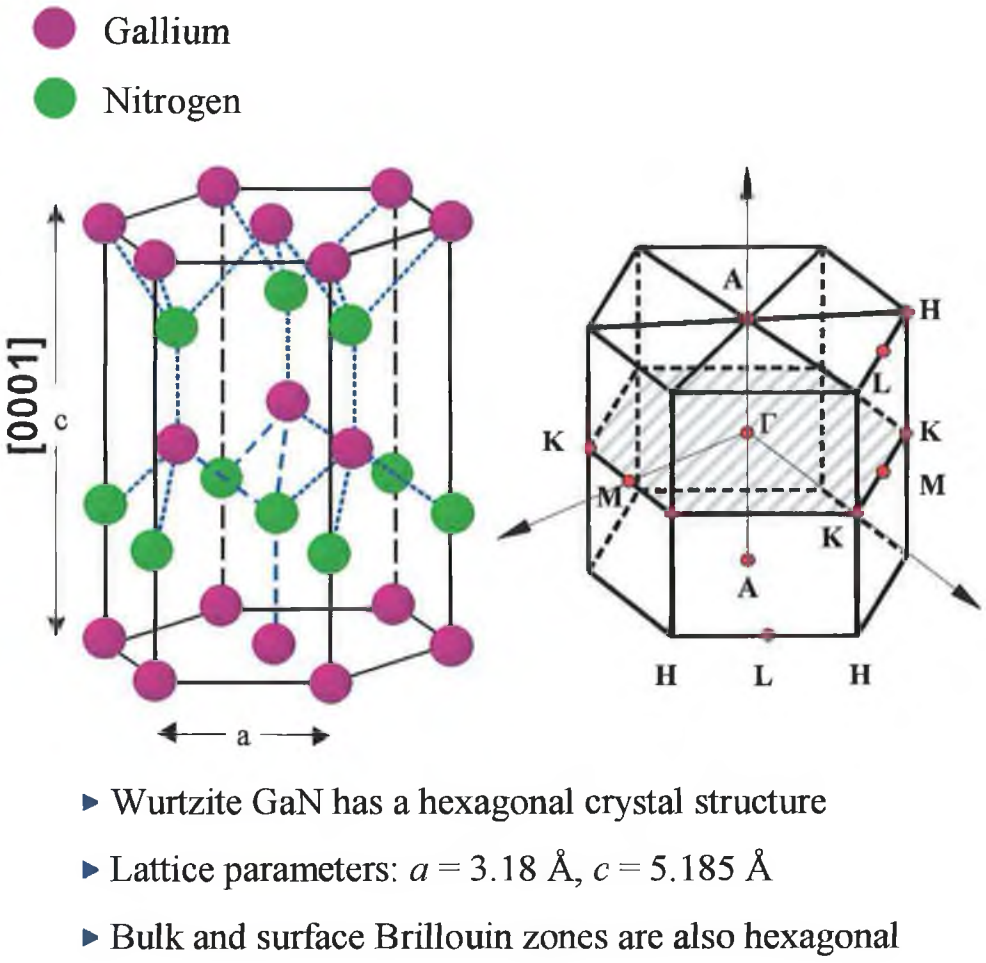

Figure 4.1 : Shows the hexagonal wurtzite crystal structure and its corresponding Brillouin zone, also hexagonal and indicating the high symmetry points. The c-axis [0001] of the structure is shown, which is also the common direction of growth, (indicating a Ga surface (top) thus Ga polar). The hatched areas show the two dimensional surface Brillouin zone which is also hexagonal.

4.1.2 : Growth of GaN

Bulk nitride crystals are not grown by the popular techniques of Czochralski or Bridgman which grow crystals from stoichiometric melts. This is due to the very high melting temperatures coupled with the very high decomposition pressures at melting, [Melting temperatures : GaN : 2791K, AlN, : 3487K, InN : 2146K][4]. This causes very low solubility of the three binary nitrides in the corresponding liquid metals. Thus the production of single bulk GaN crystals is both expensive and currently only crystals of small dimensions are grown [5]. Without large bulk single crystals, it is thus necessary to use materials with similar characteristics to act as suitable substrates for large single crystal growth. ZnO and SiC have suitable physical attributes, but wurtzitic ZnO is unstable in many of the corrosive growing environments associated with nitride growth and the high temperatures required. While SiC has been successfully used as a growing substrate, it is very expensive. By far the most common substrate material has been Al_2O_3, sapphire.

Epitaxial nitride films are produced by several different techniques, the most common growth method are hybrid vapour phase epitaxy (HVPE), molecular beam epitaxy (MBE) and metal organic chemical vapour deposition (MOCVD). HVPE uses ammonia (NH_3) and GaCl (produced by HCl flowing over a Ga melt) as the sources and N_2 as a carrier gas. High growth rates are achieved with this technique. MBE uses liquid gallium and atomic nitrogen as the source. Either an RF source or electron cyclotron resonance (ECR) may be used to produce atomic nitrogen. RF generally produces ions at relatively higher energies and so ECR is more favourable. This technique produces plasmas at lower energies by coupling the microwave energy at 2.45GHz with the resonance frequency of electrons within a static magnetic field although there is still an effect on the growth efficiency of the process which is relatively slow. MOCVD is the most widely used technique in industry with nearly all commercial optoelectronic devices being made by this process. Ammonia and tri-methyl forms of Ga (or In and Al) are used as the growth

sources. These precursors dissociate at about 550°C, with the crystal subsequently growing with increasing temperatures from 700°C to 1100°C [5].

The requirement for a foreign substrate creates many structural problems due to the lattice mismatch between the substrate and overgrowth. There is a 14.8% lattice mismatch between sapphire and GaN and 3.3% between SiC and GaN. The related structural stress created is large with dislocation densities typically of $\sim 10^{10} cm^{-2}$ [6]. Even with the introduction of low crystal quality AlN and GaN buffer layers which relax the interface induced strain, the defect density still remains very high as is clearly seen in figure 4.2 which shows a TEM cross-sectional image of GaN grown on a sapphire substrate with an AlN buffer layer [7].

The wurtzite structure has a polar asymmetry perpendicular to the (0001) plane, which is the typical growth direction. Figure 4.1 indicates the [0001] direction, which represents layered planes of each element. By convention the (0001) plane is defined by Ga bulk growth termination. Techniques to identify the polarity of GaN have been reviewed by Hellman [8]. To determine the polarity of the MBE grown samples while still in the growth chamber, the samples are cooled to allow the surface to reconstruct. Depending on the surface reconstruction (measured by RHEED), combined with model calculations performed with the aid of STM results [9] a specific polarity may be identified. The N polar structure is identified by a 3x3 reconstruction. Chemical etching experiments performed by Rouviere et al [10], indicated that Ga polar surfaces are resistant to 200°C molten NaOH and KOH etching whereas the N polar surfaces were chemically active. The etching procedure reveals the different chemical properties of the two polarities. A similar etching procedure was used in this study to substantiate the polarity assignment of our samples.

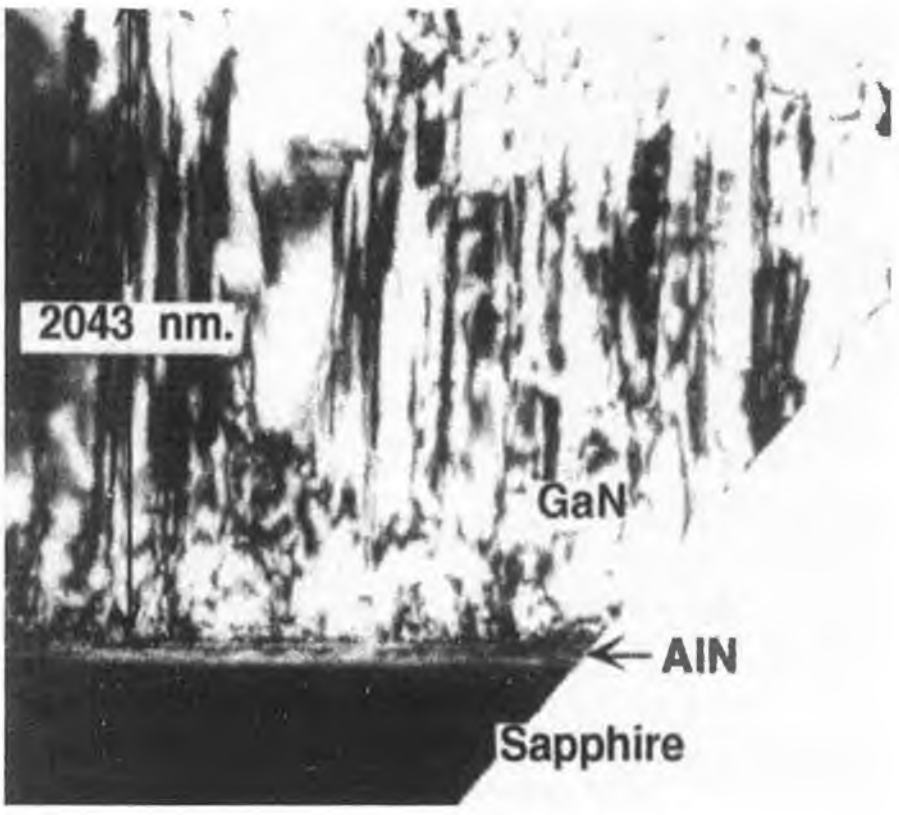

Figure 4.2 : Crossectional TEM micrograph of a GaN/AlN/sapphire structure. The image clearly indicates the level of dislocations which are estimated at 10^8 -10^{10} dislocations cm^{-2}, when compared with the level of crystal defects in other semiconductor materials such as Si: < 0.1 cm^{-2} : GaAs: ~ 50 cm^{-2} and the fore running wide band gap II-IV material

ZnSe : ~ 10^3 cm^{-2} [7].

4.1.1 : Sample preparation

With such high dislocation densities, the surface is not expected to be highly ordered. Several articles reviewing the preparation of clean GaN surfaces covering both ex-situ and in-situ procedures have been written [11-13]. The surface preparation procedures were generally sample dependent, and the procedure was modified from sample to sample. It was found that pre-etching did not improve the final clean surface, and often introduced more variables into an already troublesome process. An optical microscope was used to give an immediate indication of the quality of the surface. The sample was first rinsed in a degreasing agent such as acetone or methanol and the sample was then blown dry with nitrogen. Once the sample was under UHV conditions, it was annealed to ~800^{0}C for several hours, to remove as much amorphous surface material as possible. Initially, a Ga layer was deposited and annealed as to remove remaining oxides, but this appeared to result in a Ga rich surface. Finally, cycles of sputtering and annealing are used to present an ordered and consistent surface. As with most III-V semiconductors the group V component is preferentially bombarded and so nitrogen is used for sputtering rather than an inert source so as to replenish its supply in the near surface region. Auger electron spectroscopy gives a good indication as to whether the surface is mostly free of contaminants such as surface carbon and oxygen, and the ratio of the Ga:N signals indicate the chemical balance of the surface. LEED describes the relative long range structural quality of the surface. By far the clearest signal of a clean and ordered surface is the valence band spectral quality from UV photoemission. The spectra reveal surface features indicative of an ordered surface. The cleaning cycles are repeated until the spectra do not change thus indicating a consistent surface. Interestingly, MBE grown samples required a more prolonged cleaning procedure than MOCVD grown samples. The GaN surfaces irrespective of the growth technique were not stable even under the extreme vacuum conditions of UHV, and after 2 hours the spectral features began to loose their clarity, and required to be re-cleaned.

4.2 : Summary of Experimental Results

The surface electronic structure of MOCVD grown n-GaN(0001)1x1 and MBE grown p-type wurtzite GaN($000\bar{1}$)1x1 have been investigated using synchrotron radiation excited angle resolved photoemission spectroscopy . Several discrete surface states on both materials were identified and characterised. All the states were removed by exposure of the surface to atomic hydrogen, signaling their surface localisation. Three previously unobserved surface states on the MOCVD n-type GaN are described, one of which was highly non-localised, dispersing throughout much of the valence band. Four states were identified on the p-GaN MBE grown surface, three of the states were of p_z orbital character, while the forth is derived from s-orbitals. Three of the surface states lie below the bulk valence band maximum throughout the surface Brillouin zone, and one surface state was observed to disperse into the bulk optical band gap. Comparison to theory suggests that this surface state is Ga-derived, consistent with a model of Ga terminated, N polar GaN.

4.3 : Experimental Introduction

Wide band gap nitride semiconductors are of significant scientific and technological interest due to their use in optoelectronic and other semiconductor devices [14, 15]. While many aspects of their bulk electronic structure are understood, the same cannot be said of their surface electronic structure. A full determination of the surface electronic structure is a prerequisite to a fundamental understanding of the physics of epitaxial and overlayer growth and metal contact formation on these materials. The prototypical wide band gap nitride semiconductor is GaN, and most surface studies have focused on this nitride. The geometric structure of GaN surfaces has been recently studied, with numerous reconstructions of MBE grown GaN observed *in-situ* using both scanning tunneling microscopy and reflection high energy electron diffraction [9, 16-19].

The first complete experimental investigation of the occupied electronic structure of GaN was reported by Dhesi et al [20] using thin wurtzite n-GaN (0001) films grown by ECR assisted MBE [21]. A comparison of the experimental data with local density approximation band structure calculations by Rubio et al [22] showed excellent agreement indicating the validity of both experiment and calculations. Dhesi et al [20] also presented data indicating a prominent feature showing no dispersion in k-space and which did not agree with any calculated bulk states. The feature was identified as a surface resonance. While surface states at the valence band edge have been reported before [23], this report was the first to produce a detailed description of such a surface state. The studies presented here are a continuation of work by Dhesi et al [20]. Discovery of such a surface state prompted a wider investigation of the electronic structure of GaN, including both MOCVD and MBE grown samples. Modifications of the surface preparation procedure were made as the investigation progressed. Pre-etching certainly accelerated the cleaning process but no significant improvements were noted. The constant fear of producing an over Ga rich surface prompted several other modifications, such as omitting the gallium deposition and anneal procedure, used to remove surface oxides. The energy of the nitrogen ions during sputtering was reduced from 1.5KV to .5KV along with a reduction in the annealing temperature in an attempt to inhibit the loss of N from the surface.

4.4 : Experimental Results

4.4.1 : MOCVD n-GaN

The most successful and widely used growth technique for GaN and related materials has been metal organic chemical vapour deposition (MOCVD)[2]. Because of its technological importance, a full investigation was initiated of the surface electronic structure of clean GaN surfaces grown by MOCVD [24]. The n-type, Si doped, wurtzite GaN film was grown on a AlN buffer layer on a 6H-SiC(0001) Si face, on axis substrate

by low pressure MOCVD [25].

The first apparent difference between the two growth techniques was the hexagonal LEED (1x1) pattern, the MOCVD pattern was clear with small sharp spots and low background intensity as illustrated in figure 4.3, while the MBE samples had diffuse LEED spots and a brighter background. The clear LEED pattern of the MOCVD surface suggests a lower density of surface defects, structural domains, and higher long range structural quality.

In figures 4.4 and 4.5 a series of valence band spectra through selected emission angles, at both 26 and 50eV indicate the dispersion of the surface features. Figure 4.6 shows the effect of surface disorder and atomic hydrogen adsorption. The hydrogen was activated by a hot W filament facing the surface, as to chemisorb atomic hydrogen. Typical hydrogen exposures were ~7000 - 10,000L, (1 L = $1x10^{-6}$Torr s). The hydrogen has effectively electronically passivated the states, and indicates them to be surface localized. Figure 4.7 shows the identified surface features mapped in k-space, the two azimuths which define the hexagonal Brillouin zone are indicated. State A was found to be weakly dispersive and very sensitive to hydrogen adsorption, suggesting it to be a dangling bond. State B showed a high level of dispersion and seemed to depend on the quality of the 1x1 surface reconstruction. A streaky LEED pattern coincided with the disappearance of this state, as illustrated in figure 4.6(b). Both states also showed an increase in spectral intensity with increasing angle of incidence, thus suggesting a dependence on the z-character (surface normal) indicating both states to have p_z orbital configurations, shown in figure 4.8. The lack of information regarding the samples polarity makes it very difficult to ascertain the origins of these surface states.

In comparison with the previous MBE n-GaN studies [20] far more surface detail was procured from the MOCVD grown sample. This was interpreted as an indication of a more ordered surface. As discussed the surface took far fewer cleaning cycles and the

energy of ion bombardment was reduced to .5 KV and the annealing temperature reduced to 850°C. No pre-etching was performed or Ga deposition and annealing to remove surface oxides

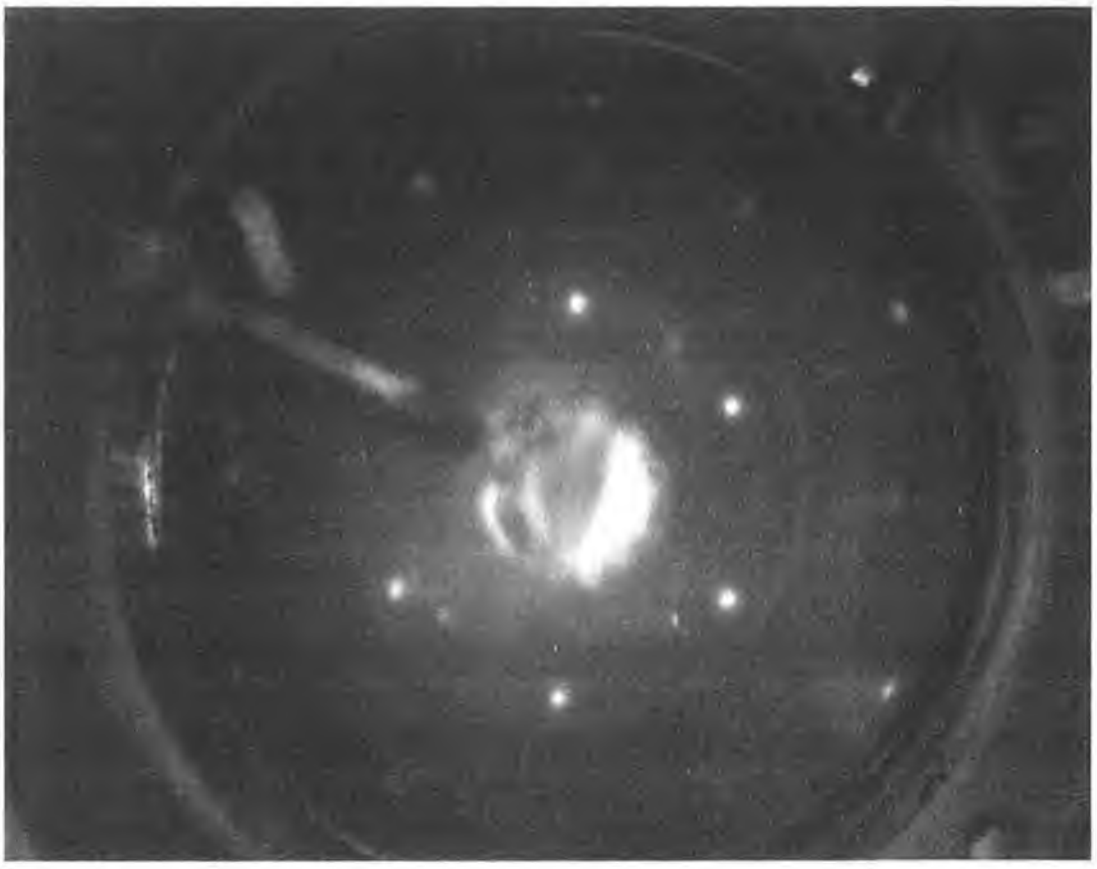

Figure 4.3 :A 1x1 hexagonal LEED pattern taken on clean MOCVD grown GaN(0001) surface. The spots are sharp with a dark background, this compares with the diffuse spots and bright background of the MBE grown GaN(0001)1x1 LEED pattern.

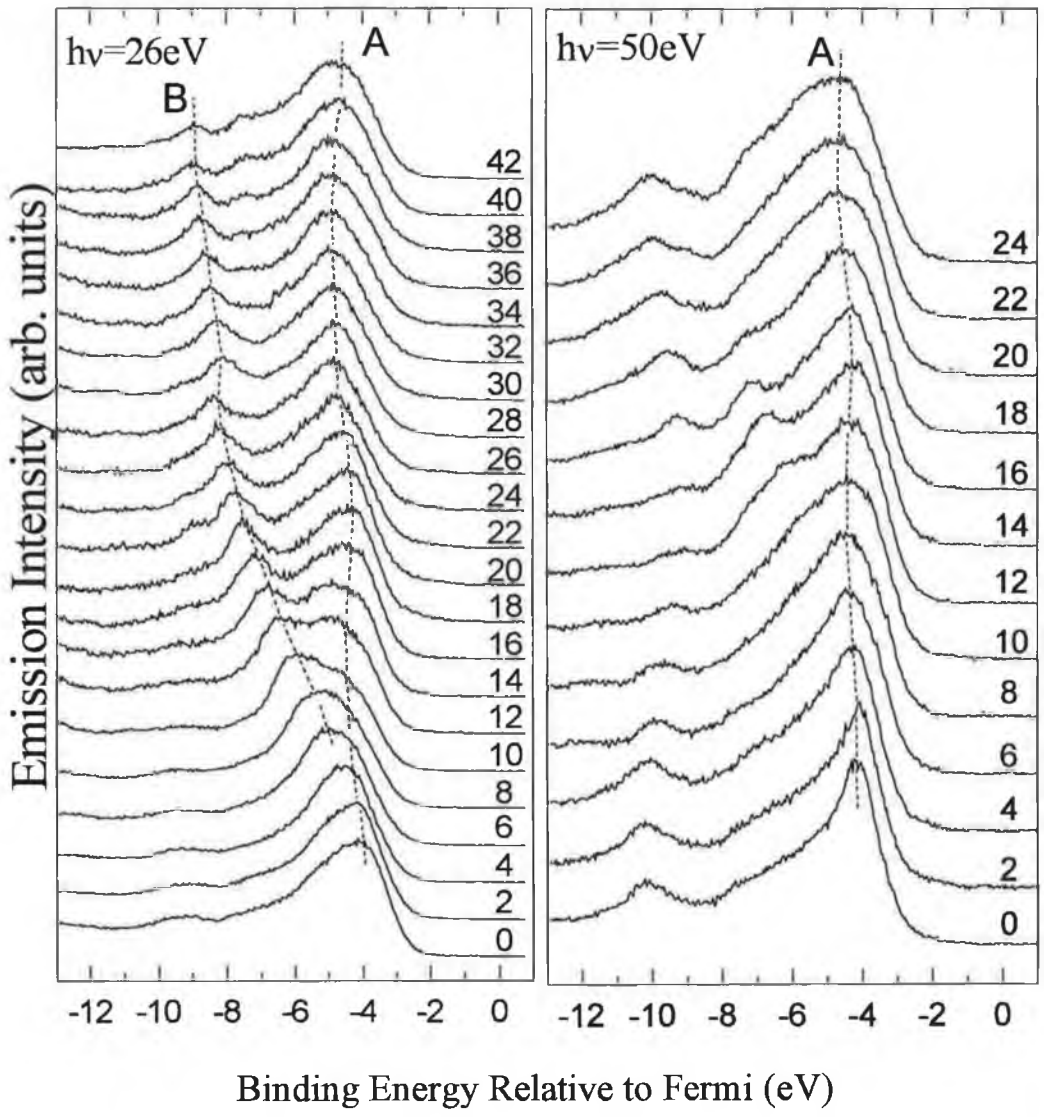

Figure 4.4 : Angle resolved photoemission spectra from the clean GaN (0001) 1x1 surface with photon energies of 26eV and 50eV showing emission from states along the $\bar{\Gamma}$- $\bar{K}$-$\bar{M}$ direction. The angle of incidence was 45°. The binding energy scale is taken with respect to the Fermi edge of a clean Ta foil

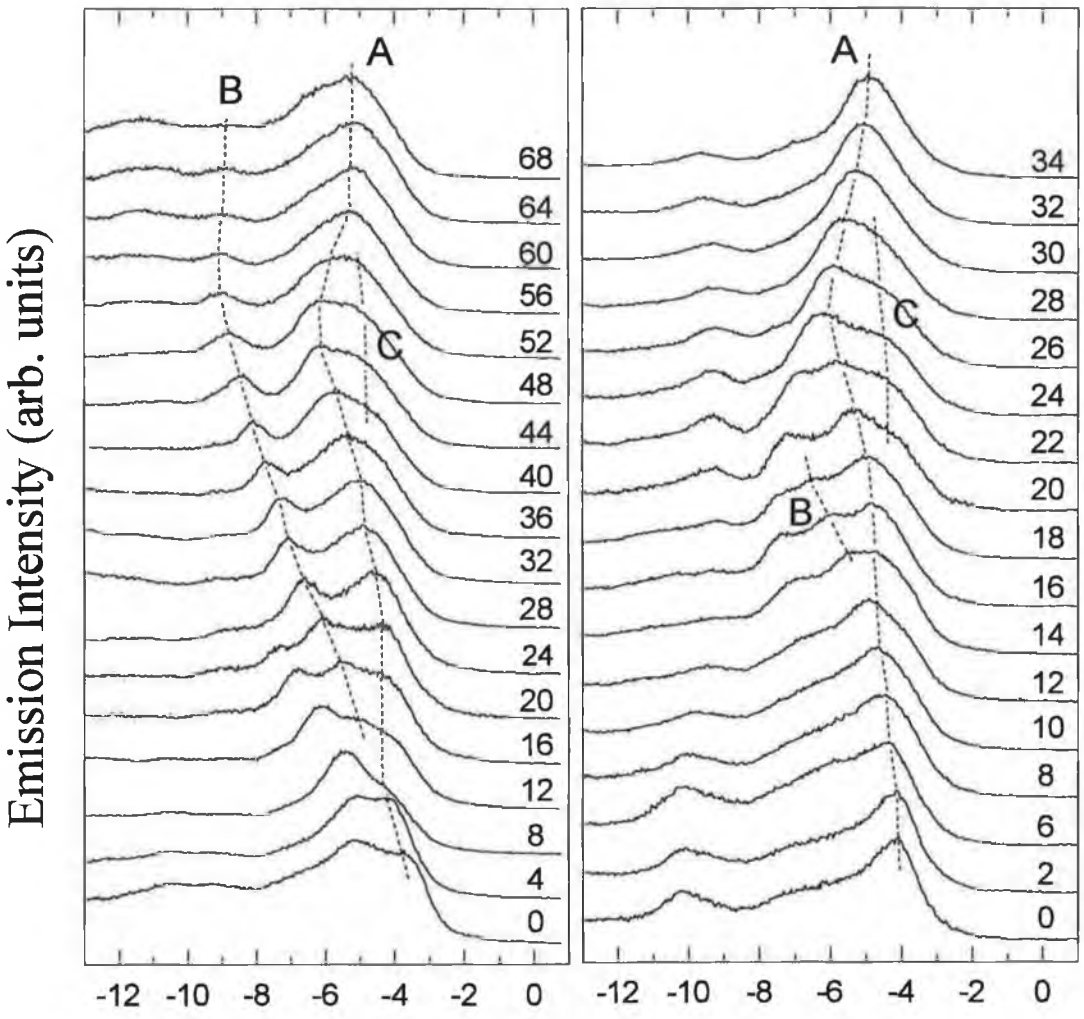

Figure 4.5 : Same as figure 4.4, except investigating states along the $\bar{\Gamma}$-$\bar{M}$ direction.

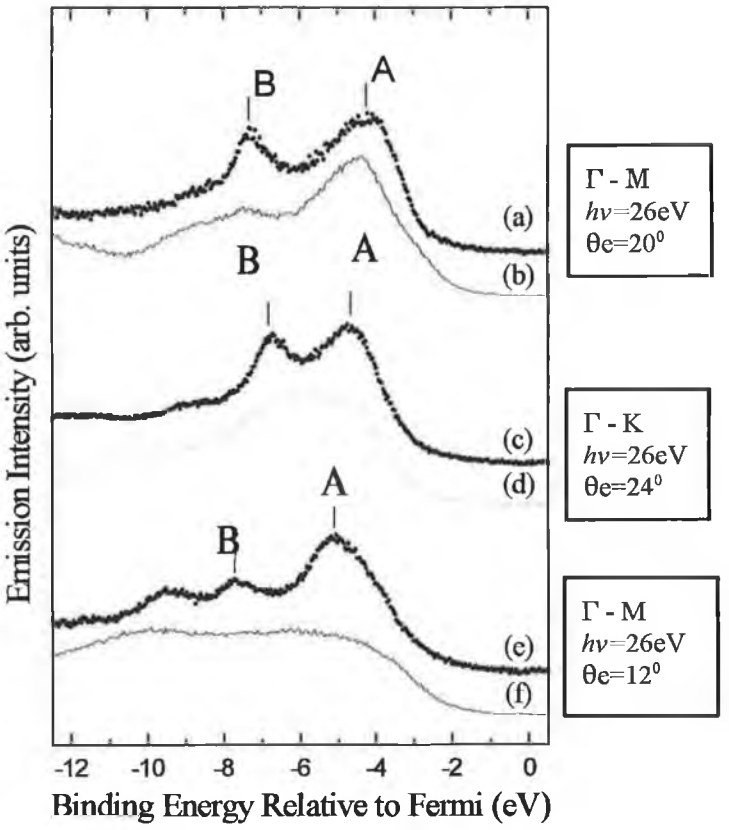

Figure 4.6 : Spectra a,c, and e, were recorded from the clean GaN(0001)1x1 surface. Spectrum b was recorded from a clean surface with a streaky 1x1LEED pattern, while d and f were recorded after saturating the surface with hydrogen.

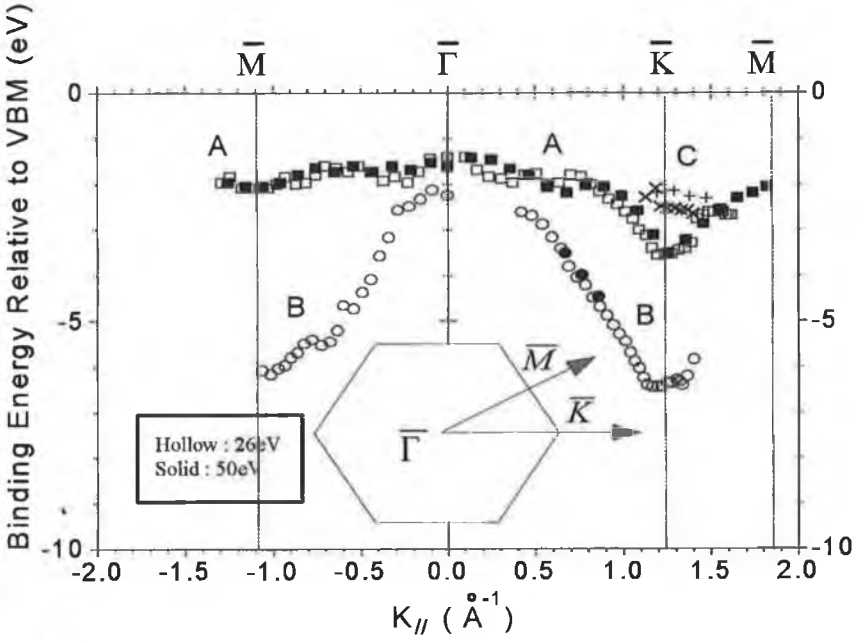

Figure 4.7 : Measures two dimensional band structure for the clean GaN (0001) surface in the 1x1 surface Brillouin zone.

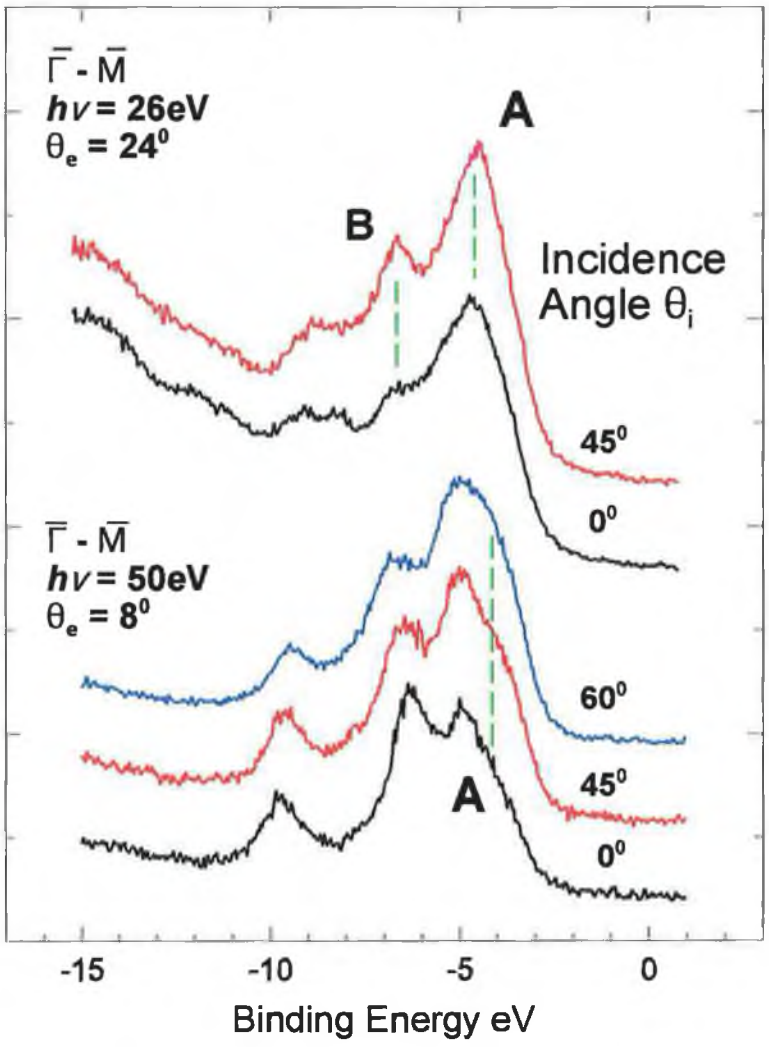

Figure 4.8 : ARP spectra recorded from the clean GaN(0001)1x1 surface with different photon energies and azimuthal directions. Information about the orbital symmetries of the surface states may be obtained by changing the incident angle of the incoming photons. Indication of the p_z orbital configuration of both states is shown.

4.4.2 : MBE p-GaN

The largest stumbling block in the development of GaN based devices has been the production of low resistivity p-GaN. The lack of p-type GaN films prevented the ability to produce visible light emitting p-n junction diodes. Typically grown GaN is naturally n-type, most likely due to nitrogen vacancies. As recently as1992 Nakamura et al [26] started to consistently produce p-GaN with low resistence by thermal annealing which removed hydrogen impurities breaking the H-Mg complexes and activating the doping material, Mg.

The samples in this study were Mg doped p-type GaN with a carrier concentration of $5x10^{17}cm^{-3}$. The samples were grown on a sapphire substrate with a 50nm GaN buffer layer. The polarity of the sample was determined to be predominantly N-polar with evidence of inversion domains [27]. Inversion domains comprise of micro domains where the polarity of the structure reverses, in this case becoming Ga polar. Mg incorporation during MOCVD growth has been reported [28] under certain growth conditions to form micro-superlattices, comprised of planar defects which show characteristics of inversion domains. MBE growth also reported evidence of inversion domains caused by Mg exposure to the surface during the growth process [29], therefore, the polarity of the sample within these domains switches. The method of polarity determination follows from STM and model calculations by Smith et al [30]. For GaN grown on a GaN buffer layer, the surface is unreconstructed displaying a 1x1 pattern as observed by RHEED measurements made at the growth temperature (~750°C). However upon cooling to 300°C or lower the surface reconstructs forming a 3x3 RHEED pattern, which is associated with N polarity. It is possible to control the polarity of an MBE grown sample by changing the buffer layer. It has been found that samples with an AlN buffer layer grow with a Ga polarity while samples with a GaN buffer layer grow with N polarity [27]. As with the MOCVD grown samples, the p-type MBE were not pre-treated before being put into UHV, and once inserted, were annealed for several hours at 800°C and then several sputter-anneal cycles at .5KeV and

850°C respectively. The LEED pattern showed diffuse spots and a bright background which was taken as an indication of poor long range order of the surface. Obtaining a consistent valence band spectra for the clean surface was far more difficult to achieve than for MOCVD grown material and took a greater number of cleaning cycles to prepare the surface. The spectral quality was also found to vary across the sample, in contrast to the MOCVD grown samples.

Figures 4.9 and 4.10 show a series of valence band spectra with a selected range of emission angles in both $\bar{\Gamma}$-$\bar{K}$-$\bar{M}$ and $\bar{\Gamma}$-$\bar{M}$ directions at both 35eVand 50eV incident energies. The dispersion of the four identified surface peaks are shown with the aid of dashed lines. States B, C and D all sit within the bulk valence band, while state A sits most predominantly in the band gap and is therefore a potential recombination centre. Three states show a level of dispersion but B shows a distinctive lack of dispersion, identical to the surface state reported by Dhesi et al [20] on similarly grown n-GaN. States C and D sit deep in the bulk valence band. Figure 4.11 shows selected spectra comparing the clean and atomic hydrogen exposed surfaces, illustrating the removal of all four states. The cleaned surface normally lasted ~2 hours at pressures in the region of $9x10^{-11}$Torr, after which the spectral quality of the valence band deteriorated. This is in contrast to the hydrogen terminated surface which remained stable for long periods of time under UHV conditions, in effect electronically passivating the surface.

Figure 4.12 compares spectra of different incident angles, with all other variables kept constant. Using the fact that the incident synchrotron light is plane-polarised, as the incident angle tends away from the surface normal, the relative intensity of states A, B, and D dramatically increase due to increasing cross-sections, while state C remains constant. These results indicate that states A, B and D have p_z character and state C's an s electronic orbital configurations, which is spherically symmetrical.

These states have been mapped within the surface Brillouin zone in figure 4.13

assuming the free electron theory [31]. Data using both 35eV and 50eV incident energies was used to map the surface states which covered both $\bar{\Gamma}$- $\bar{K}$-$\bar{M}$ and $\bar{\Gamma}$-$\bar{M}$ azimuths. The bulk valence band maximum position was determined by its position at $\bar{\Gamma}$ point, and 1.61eV binding energy compares well to previous measurements [32].

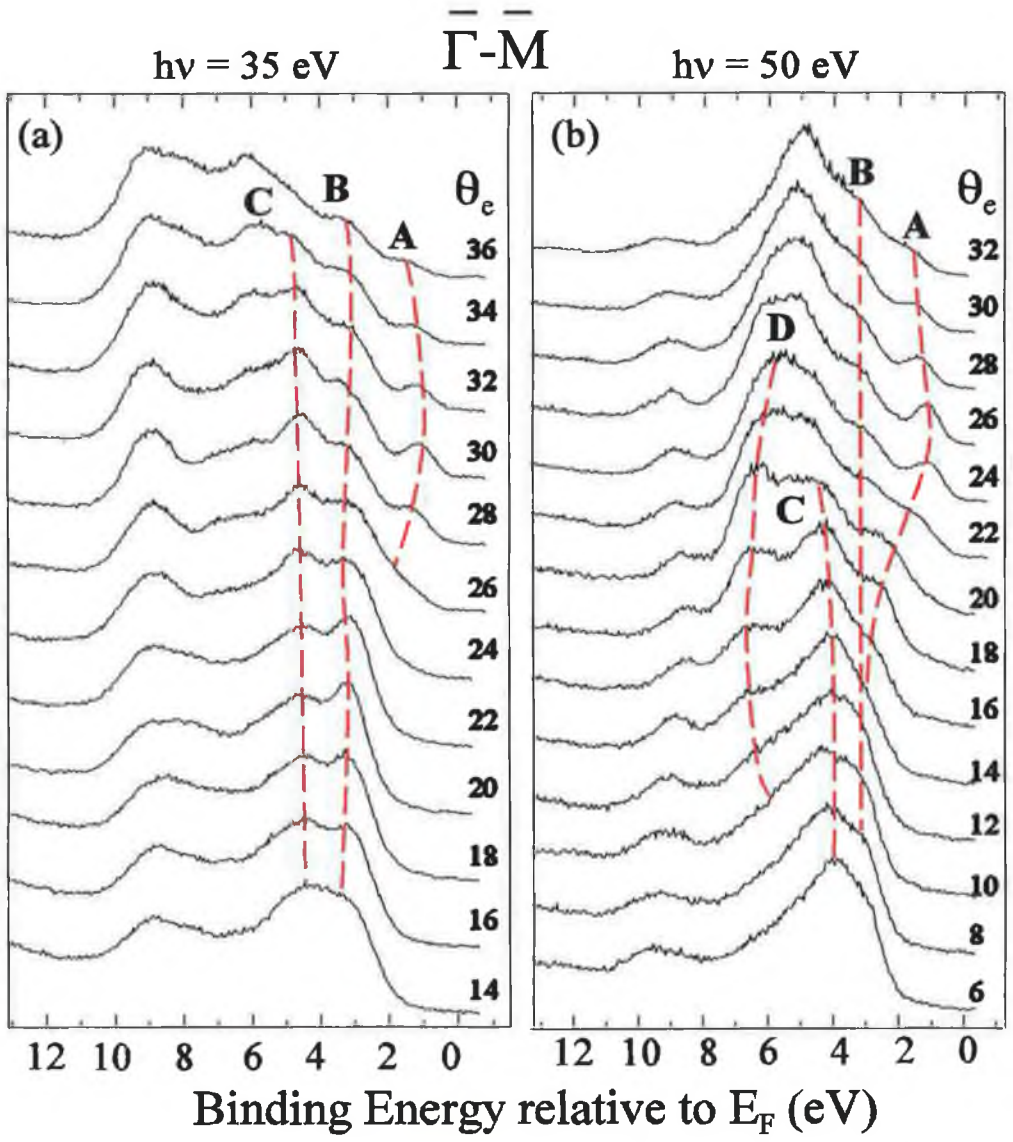

Figure 4.9 : ARP spectra recorded from a clean p-GaN(0001) 1x1 surface with photon energies of 35eV and 50eV showing emission states along the $\bar{\Gamma}$- $\bar{M}$ direction. The angle of incidence was 45°.

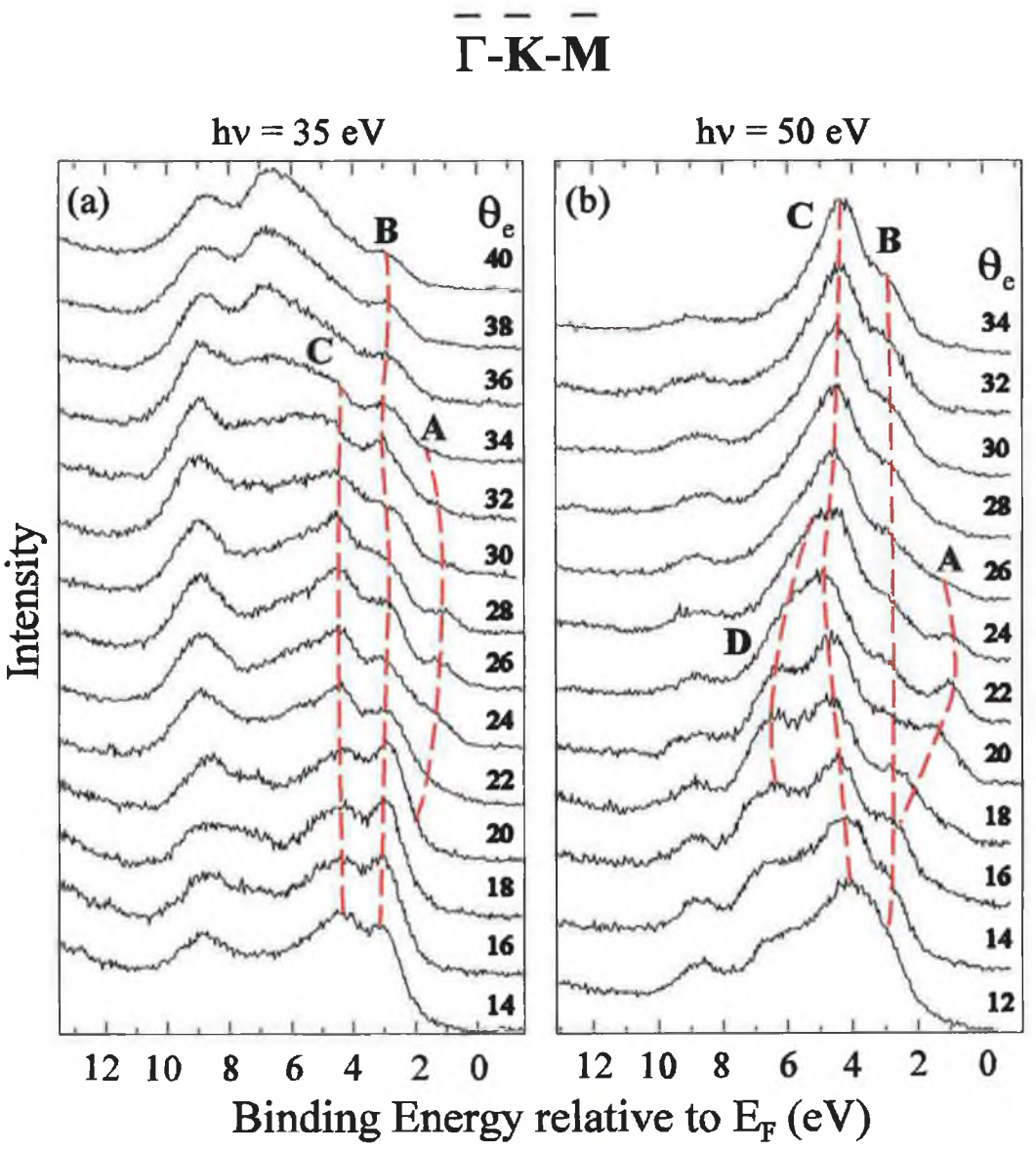

Figure 4.10 : Same as figure 4.9 but for states along the $\bar{\Gamma}$-$\bar{K}$-$\bar{M}$ direction.

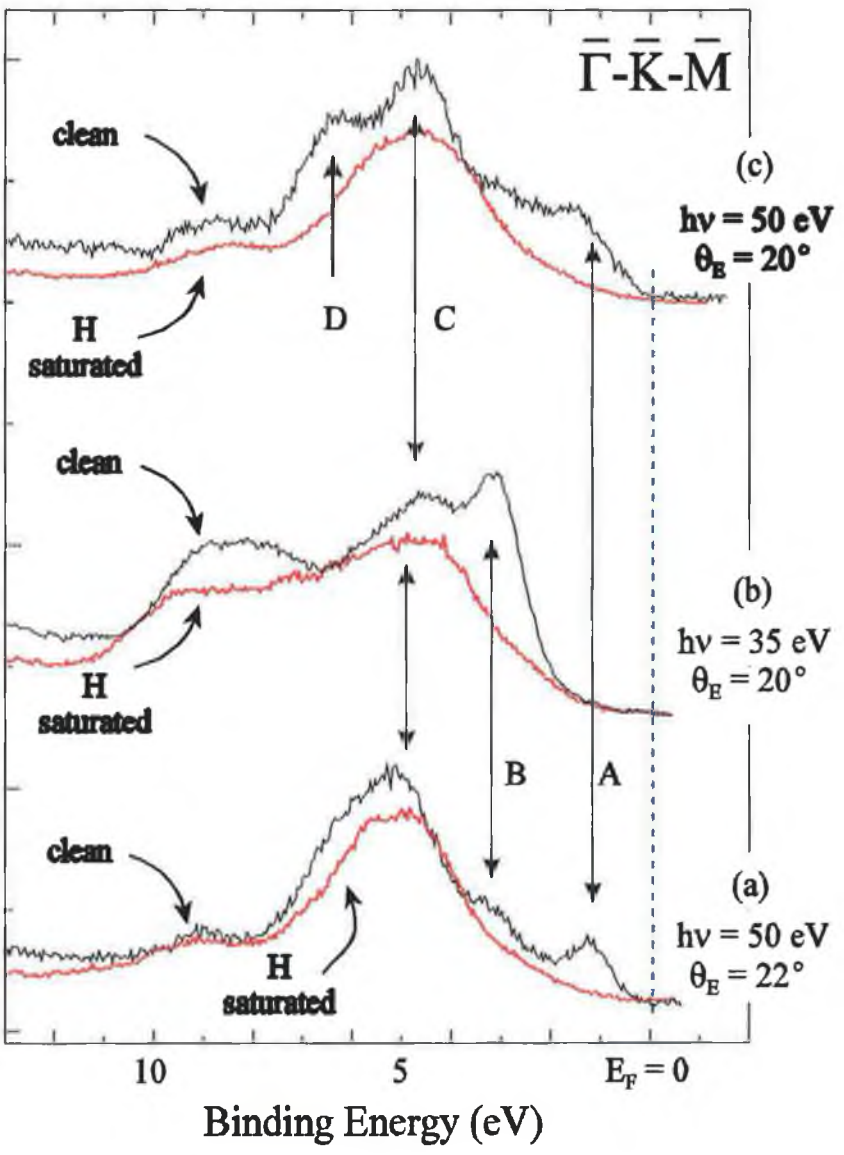

Figure 4.11 : ARP spectra recorded from the clean and hydrogen saturated p-GaN(0001)1x1 surface. States along the $\bar{\Gamma}$-$\bar{K}$-$\bar{M}$ azimuth are shown, and photon energies and emission angles are indicated. The removal of all the surface state emission features (A,B,C and D) by hydrogen adsorption are noted.

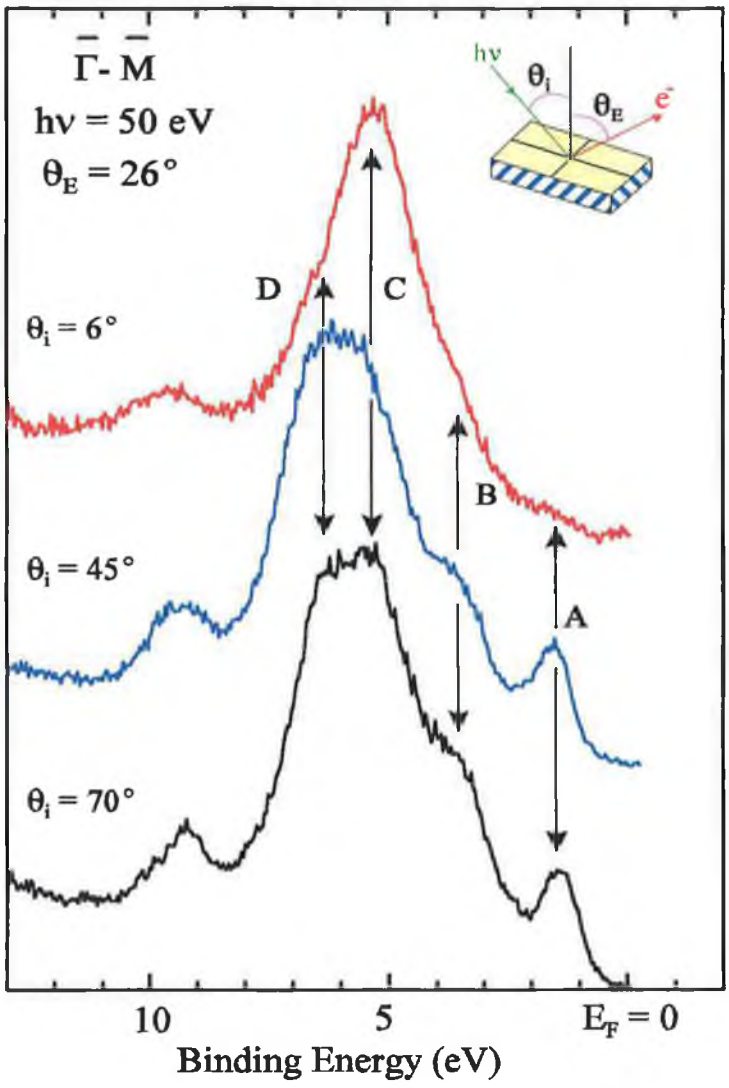

Figure 4.12 : ARP spectra as a function of the photon angle of incidence recorded from the clean p-GaN surface with a common incidence energy of 50eV and emission angle of 26°. The orbital configurations of the surface states are probed by changing the incidence angle. (The recording geometry is indicated in the inset.)

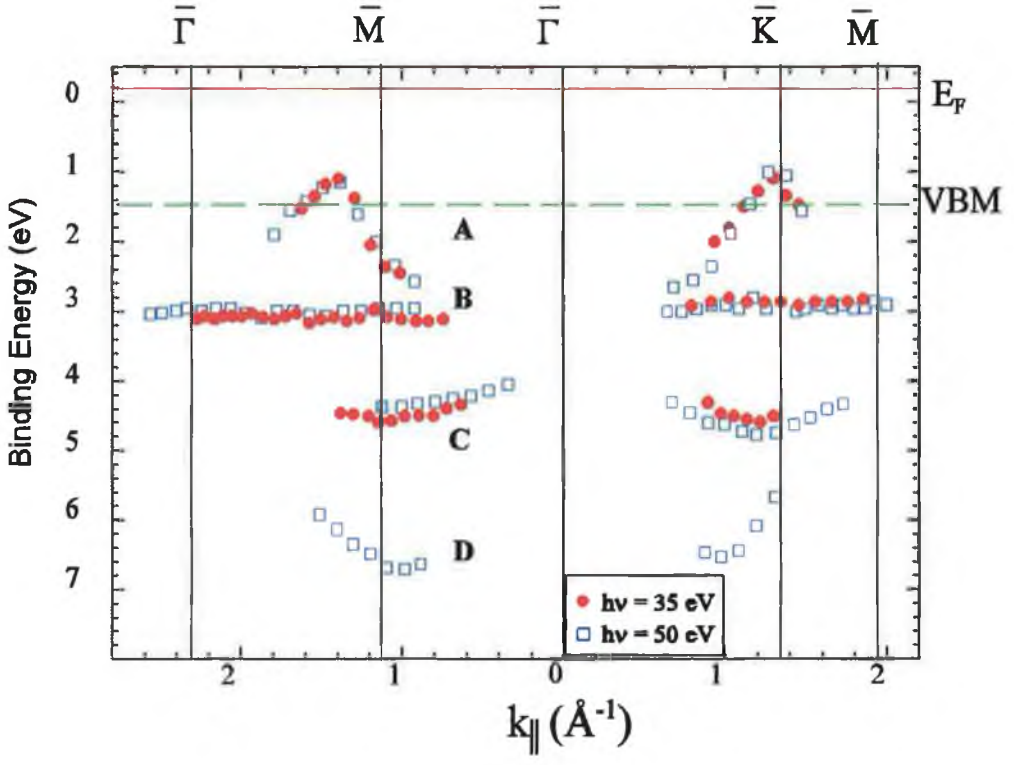

Figure 4.13 : The measured two dimensional surface band structure for the clean p-type GaN(0001)1x1 surface, mapped in the 1x1 surface Brillouin zone.

The non-dispersive quality of state B indicates the lack of local electronic interaction and its p_z orbital configuration agrees with Dhesi et al [20] that this state is a dangling bond. States C and D have s and p_z orbital configurations respectively, indicating them to be back bonding, intrinsic surface states. State A shows a remarkable level of dispersion sweeping close to the Fermi level within the bulk band gap, and clearly shows its potential to act as an optical recombination centre.

Because the surface preparation procedure is invasive and continues throughout the length of the experiment, a second, post-experiment procedure was deemed necessary to check sample polarity. Hellman [8] reviewed the issue of GaN polarity and after investigating several techniques formulated a 'standard framework' by which to work with. As discussed, it is expected that GaN samples with Ga and N polarities will have different chemical properties, and it was found that with NaOH or KOH etching the samples with

different polarities have different reactivities.

After the p-type GaN sample was removed from UHV, it was divided and one side was etched in a solution of 100ml de-ionized water and 10g of KOH at 150°C for 3 minutes, as described by Doppalapudi [33]. AFM images (figure 4.14) of both etched and un-etched samples were taken. From the images shown it is evident that a high degree of etching occurred at the surface, the chemical activity indicates the sample to have N polarity.

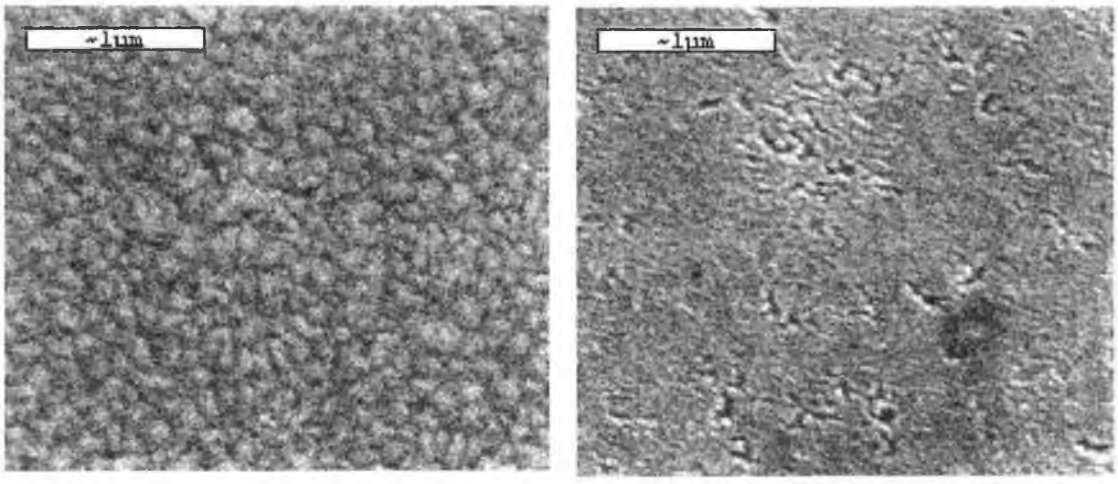

(a) *(b)*

Figure 4.14 : SEM images of the (a) cleaned and (b) cleaned and etched p-GaN sample. The high level of chemical etching in (b) is evident from the severe change in the morphology of the surface.

4.5 : Discussion of Results

Bermudez identified a surface state when absorbing oxygen onto clean GaN. This was the first evidence of a surface state resonant in the GaN valence band [23]. Rizzi et al noted a shoulder continuously present on GaN(0001)(1x1) sample at the valence band edge. This coupled with their HREELS spectra showing a shoulder absorption peak at 2.53eV, may have indicated a transition from an occupied surface state to either an empty bulk or surface conduction band state [34]. But, the first detailed description of a GaN surface valence band state was given by Dhesi et al [20].

In order to investigate the origin of these states it is necessary to refer to model simulations. Theoretical calculations have been carried out for the GaN bulk band structure [22, 35-38], but few for the surface derived bands [18, 36, 39]. Figure 4.15 shows a ball and stick figure illustrating the proposed model by Smith et al [40]. The surface is N polar but gallium terminated by an adlayer, where each adatom sits on top each of the N atoms. Using this model the same report calculated the surface band structure with local density functional calculations. Figure 4.16 (a) shows the calculation results of three surface states clearly distinct from the bulk bands denoted by S_1, S_2 and S_3. All three states are associated with the Ga adlayer. S_1 is fully occupied and has a p_z orbital configuration. This state corresponds well in terms of position and dispersion with the experimentally observed state A of the p-type MBE samples. It is a highly dispersing state, finding its maximum just below the Fermi level at the $\bar{K}$ point and it follows a similar dispersion path from $\bar{K}$ - $\bar{\Gamma}$. Both other states were unoccupied although, one of which (S_3) disperses below the Fermi level, suggesting a metallic surface system. Both of these states originate from Ga-Ga p_x and p_y orbitals and the authors propose that these states give this surface its stability.

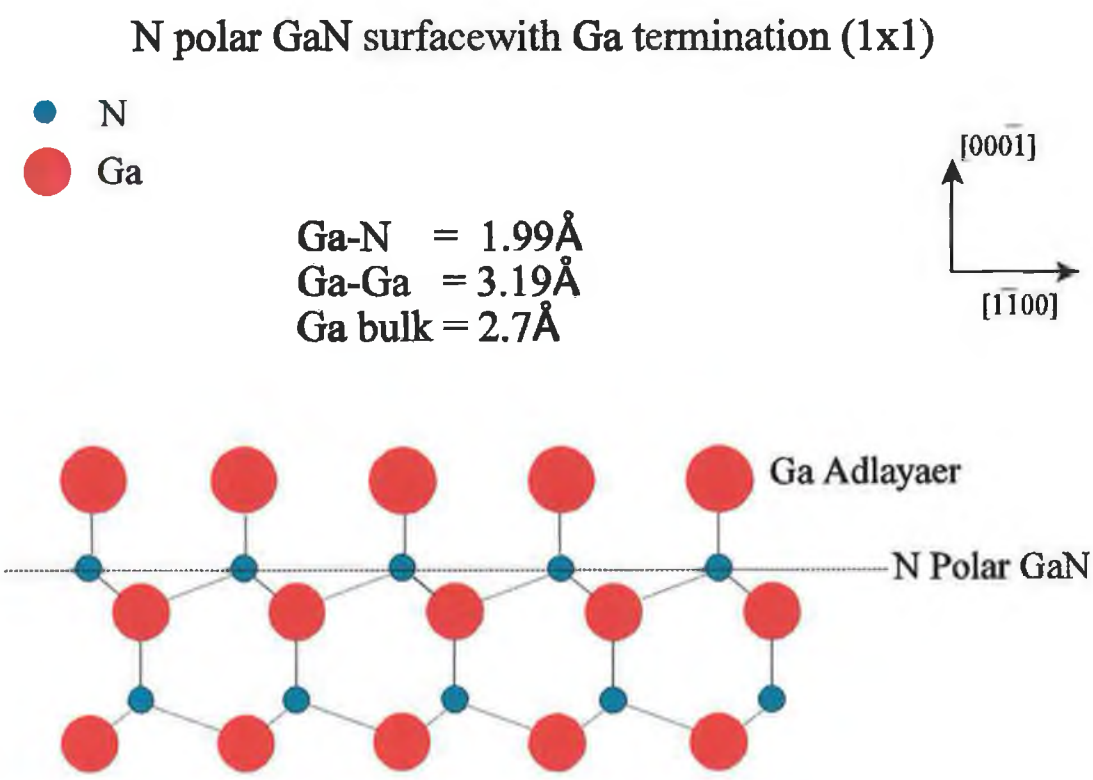

Figure 4.15 : Model structure for the 1x1 Ga adlayer N–polar GaN surface. The Ga adlayer is under tensile stress since the Ga atoms are stretched further apart than the bulk Ga spacing i.e. 3.19Å compared to 2.7Å [40].

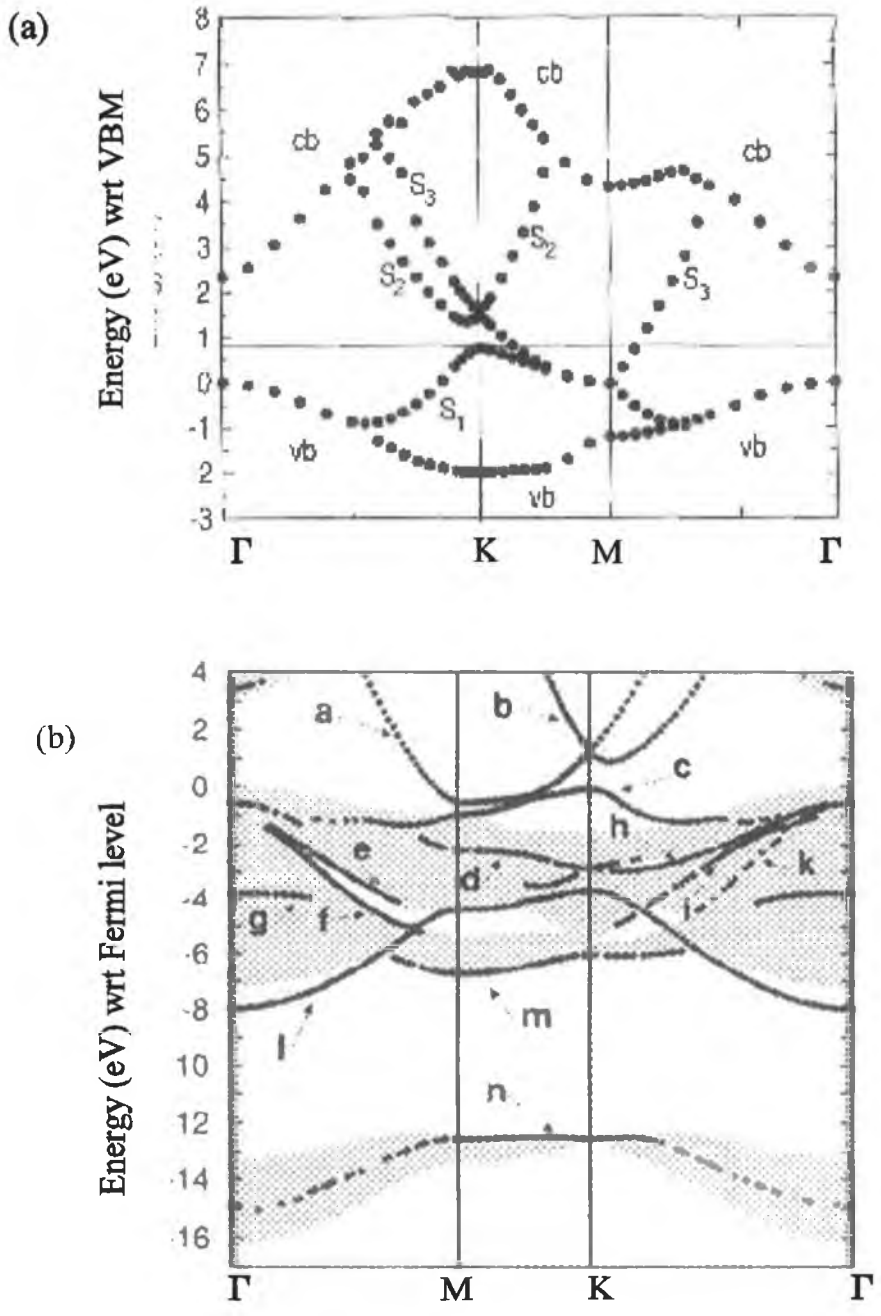

Figure 4.16 : Surface band calculations based on the Ga ad-layer terminated N-polar 1x1 GaN surface. Top : Smith et al [18], proposed the model which both calculations are based. Local density functional calculations have been used to formulate the bands. Bottom : Strasser et al [39] uses total energy calculations performed within local density formalism. The shaded area indicates the bulk derived band.

The stability of the model depends on both the Ga-N bond and the interaction of the Ga adatoms. The bulk inter-atomic spacing for Ga metal is 2.7Å and the proposed model suggests the Ga adlayer separation to be 3.19Å. This might suggest the Ga ad-atoms would form dimers, because of the large atomic spacings between p_z orbital configurations. There would be a relatively small overlap between the orbitals from such dimers, and the resulting occupied bonding state of the partially filled Ga 4p state would disperse close to the Fermi edge [41]. This would support evidence of an occupied surface state close to the Fermi level within the bulk band gap such as state A, from figure 4.13. However no experimental evidence of dimer formation was found by the STM studies.

Why do the Ga adatoms not form dimers? Smith et al [40] suggest that the S_2 and S_3 states which originate from p_x and p_y orbitals supply additional stability along with the strong Ga-N bonding for this model. In a similar case of the GaAs $(\bar{1}\bar{1}\bar{1})$ surface [18], where the Ga-Ga separation within the adlayer is 4 Å, calculations show that the total chemical reaction of the Ga adlayer is endothermic, thus dimers are more likely to form on this surface. The reduced Ga-Ga distance on the GaN $(000\bar{1})$ surface may explain why the surface system does not form dimers, although it is clear that the Ga-Ga interaction within the adlayer plays an important role in the stability of this structure.

Corroborating these findings, Strasser et al [39] using the same GaN$(000\bar{1})$ surface model, also calculated three distinctive surface states with similar attributes. Figure 4.16b indicates several more surface features but three of the peaks a,b and c are almost identical to the three surface states reported by Smith et al [40]. States a and b are mostly unoccupied, and are derived predominently from p_x and p_y orbitals. State c originates from both Ga s and p_z orbitals and disperses around $\bar{\Gamma}$ point, following a similar dispersion path as the experimental state A,(figure 4.13).

Both calculations found the surface system to be metallic, as a single surface state disperses across the bulk band gap. Smith et al [40] also presented scanning tunneling

spectroscopy(STS) results which indicated a metallic surface. However, no evidence of metallic gallium in the Ga 3d core level or a Fermi edge was found in our measurements. Previous inverse photoemission studies [42]on MBE grown n-GaN showed no evidence of unoccupied conduction band surface states. The samples were prepared in the same manner as earlier ARP studies [20]. In that study only one non-dispersive surface state was observed which was thought to be a dangling bond therefore one would not expect to have an associated anti-bonding state. Later studies with higher quality samples and improved cleaning techniques on n and p-type GaN have revealed many surface features of superior quality. Further inverse photoemission studies on these samples would offer a clearer understanding of the surface states and reveal the accuracy of the model calculations.

4.6 : Conclusions

The surface electronic structure of both MOCVD grown n-GaN and MBE grown p-GaN were studied [24, 43] by angle resolved photoemission spectroscopy. Both surfaces revealed many intricate surface features. The ability to determine the polarity of the samples helped investigate the origin of the mid gap state A on the MBE grown p-GaN surface. The disparity between the surface band detail from the MBE and MOCVD grown crystals indicates very different terminating surface structures. The angle resolved (ARP) study of MBE grown n-GaN [20] which revealed a non-dispersive dangling bond state, was reproducible on other MBE grown GaN samples including the p-GaN, presented here, (state B). Although the MOCVD samples showed superior LEED patterns suggesting higher long range order, the surface valence band spectra of the p-type MBE sample were of higher quality, perhaps indicating the importance of the surface preparation.

A better understanding of epitaxial and overlayer thin film growth and interfacial electronic characteristics may be derived from the knowledge acquired of the electronic structure of prepared clean surfaces of III-V nitrides. This study of the bulk electronic

structure of GaN, lead to a fruitful investigation and exploration of improving the preparation techniques of clean surfaces and has added to the understanding of the complex nature of the these surfaces.

4.7 : References

1. Morkoc, H. and S.N. Mohammad, *High-Luminosity Blue and Blue-Green Gallium Nitride Light- Emitting-Diodes.* Science, 1995. **267**: p. 51.
2. Nakamura, S. and G. Fasol, *The Blue LED.* 1997, Berlin-Heidelberg: Springer.
3. Orton, J.W. and C.T. Foxon, *Group III nitride semiconductors for short wavelength light emitting devices.* Rep. Prog. Phys, 1998. **61**: p. 1-75.
4. Porowski, S. and I. Grzegory, *Growth of GaN Single Crystals Under High Nitrogen Pressure,* in *GaN and Related Materials,* S.J. Pearton, Editor. 1997, Gorden and Breach Science Publishers.
5. Gil, B., ed. *Group III Nitride Semiconductor Coumpounds.* , ed. H. Kamimura, R.J. Nicholas, and R.H. Williams. 1998.
6. Ponce, F.A., *Microstructure of Epitaxial III-V Nitride thin films,* in *GaN and related Materials,* S. Pearton, Editor. 1997.
7. Hersee, S.D., J.C. Ramer, and K.J. Malloy, *The microstructure of MOCVD GaN on Saphire.* MRS Bulletin, 1997. **22**(7): p. 45.
8. Hellman, *GaN Polarity : A critical Review.* MRS Internet J. Nitride Semicond. Res. 3, 11(1998)., 1998.
9. Smith, A.R., *et al., Reconstructions of the GaN(0001) surface.* Physical Review Letters, 1997. **79**(20): p. 3934-7.
10. Rouviere, J.L., *et al., Polarity determination for GaN films grown on (0001) sapphire and high-pressure-grown GaN single crystals.* Applied Physics Letters, 1998. **73**(5): p. 668.

11. Smith, L.L., *et al.*, *Cleaning of GaN Surfaces.* Jrnl. of Electronic Materials, 1996. **25**(5).

12. King, S.W., *et al.*, *Cleaning of AlN and GaN surfaces.* Journal of Applied Physics, 1998. **84**(9): p. 5248-5260.

13. Bermudez, V.M., D.D. Koleske, and A.E. Wickenden, *The dependence of the structure and electronic properties of wurtzite GaN surfaces on the method of preparation.* Applied Surface Science, 1998. **126**(1-2): p. 69-82.

14. Ponce, F.A. and D.P. Bour, *Nitride-based semiconductors for blue and green light-emitting devices.* Nature, 1997. **386**(6623): p. 351-359.

15. Strite, S. and H. Morkoç, *GaN, AlN, InN: A review.* Journal of Vacuum Science and Technology B, 1992. **10**: p. 1237.

16. Hacke, P., *et al.*, *Monitoring surface stoichiometry with the (2*2) reconstruction during growth of hexagonal-phase GaN by molecular beam epitaxy.* Applied Physics Letters, 1996. **69**(17): p. 2507-9.

17. Okumura, H., *et al. Surface reconstruction and As surfactant effects on MBE-grown GaN epilayers.* in *Silicon Carbide, III-Nitrides and Related Materials. 7th International Conference*. 1997. Stockholm, Sweden: Trans Tech Publications.

18. Smith, A.R., *et al.*, *Wurtzite GaN surface structures studied by scanning tunneling microscopy and reflection high energy electron diffraction.* Journal of Vacuum Science and Technology A, 1997. **16**(3): p. 1641-5.

19. Smith, K.E., *et al.*, *Bulk and Surface Electronic Structure of GaN Measured Using Angle Resolved Photoemission, Soft X-ray Emission and Soft X-ray Absorption.* Materials Research Society Proceedings, 1997. **449**: p. 787-792.

20. Dhesi, S.S., *et al.*, *Surface and Bulk Electronic Structure of Thin Film Wurtzite GaN.* Physical Review B, 1997. **56**: p. 10271 - 10275.

21. Lei, T., *et al.*, Applied Physics Letters, 1991. **59**: p. 944.

22. Rubio, A., J.L. Corkill, and M.L. Cohen, *Quasiparticle band structures of short-period superlattices and ordered alloys of AlN and GaN.* Physical Review B (Condensed Matter), 1994. **49**(3): p. 1952- 6.

23. Bermudez, V.M., *Study of oxygen chemisorption on the GaN(0001)-(1*1) surface.* Journal of Applied Physics, 1996. **80**(2): p. 1190-200.

24. Chao, Y.C., *et al.*, *Observation of Highly Dispersive Surface States on GaN(0001) 1×1.* Physical Review B, 1998. **59**(24): p. R15586-/R15589.

25. Weeks Jr., T.W., *et al.*, *GaN thin films deposited via organometallic vapor phase epitaxy on (6H)SiC(0001) using high-temperature monocrystalline AlN buffer layers.* Applied Physics Letters, 1995. **67**: p. 401-403.

26. Nakamura, S., *et al.*, Jpn. J. Appl. Phys., 1992. **31**: p. L139.

27. Moustakas, T.D., *Private Communication*, . 2000.

28. Liliental-Weber, Z., *et al.*, *Spontaneous Ordering in Bulk GaN : Mg Samples.* Phys. Rev. Lett., 1999. **83**(12): p. 2370.

29. Ramachandran, V., *et al.*, *Inversion of wurtzite GaN (0001) by exposure to magnesium.* Appl. Phys. Lett., 1999. **75**: p. 808.

30. Smith, A.R., *et al.*, *Determination of wurtzite GaN lattice polarity based on surface reconstruction.* Applied Physics Letters, 1998. **72**(17): p. 2114-16.

31. Kevan, S.D., *Angle Resolved Photoemission*, ed. S.D. Kevan. 1991, Amsterdam: Elsevier.

32. Wu, C.I., *et al.*, *GaN(0001)-(1*1) surfaces: composition and electronic properties.* Journal of Applied Physics, 1998. **83**(8): p. 4249-52.

33. **Doppalapudi, D.**, *Thesis*, in *Electrical and Computer Engineering Department, Boston University, Boston, MA 02215*. 1999, Boston University: Boston.

34. Rizzi, A. and H. Luth, *Electronic gap states on GaN (0001)-(1x1) surfaces studied by electron spectroscopies.* Il Nuovo Cimento, 1998. **20D**(N. 7-8): p. 1039-1045.

35. Xu, Y.-N. and W.Y. Ching, *Electronic, Optical, and Structural Properties of some Wurtzite Crystals.* Physical Review B, 1993. **48**: p. 4335.

36. Strasser, T., *et al.*, *Valence-band photoemission from GaN(001) and GaAs:GaN surfaces.* Physical Review B (Condensed Matter), 1997. **56**(20): p. 13326-34.

37. Rubio, A., *et al.*, *Quasiparticle bond structure of AlN and GaN.* Physical Review B (Condensed Matter), 1993. **48**(16): p. 11810-16.

38. Ding, S.A., *et al. Electronic structure of wurtzite GaN(0001)*. in *Proceedings of the 23rd Int'l Conference on the Physics of Semiconductors*. 1996: World Scientific, Singapore.

39. Strasser, T., *et al.*, *Valence Band Photoemission from the GaN(0001) surface.* Phys. Rev. B, 1999. **60**(16): p. 11577.

40. Smith, A.R., *et al.*, *Reconstructions of GaN(0001) and (000-1) surfaces: Ga-rich metallic structures.* J. Vac. Sci. Technol., 1998. **B16(4)**(Jul/Aug): p. 2242-2249.

41. Bermudez, V.M., *Private Communication*, .

42. Valla, T., *et al.*, *Unoccupied band structure of wurtzite GaN(0001).* Physical Review B-Condensed Matter, 1999. **59**(7): p. 5003-5007.

43. Ryan, P., *et al.*, *Surface electronic structure of p-type GaN(0001).* Surface Science Letters, 2000. **467**: p. L827-L833.

Chapter 5

Valence and Conduction Band Studies of $In_xGa_{1-x}N$ Alloys

5.1 : General Introduction

InGaN has become an important commercial nitride, as it is now used as the optically active layer in nitride based light emission devices in both LEDs and laser diodes [1, 2].

The $In_xGa_{1-x}N$ alloy is a random alloy in either the hexagonal wurtzite or cubic zinc-blende structure. The cation sites (Group III) are randomly occupied between Ga and In with the relative compositions x and 1-x respectively, but with all anion sites remaining occupied by nitrogen as illustrated in figure 5.1. Because of the large difference between the Ga-N (1.94Å) and the In-N (2.15Å) [3] bond lengths, the atomic positions are expected to vary, particularly with increasing indium composition. Experimental studies have reported that the system phase separates with a large indium content [4-6]. Theoretical studies have [3] also found that even with low indium content ($In_{.2}Ga_{.8}N$), the calculated bond length distribution centered around both the In-N and Ga-N bond lengths.

The growth of InGaN crystals is hampered not only by the large lattice mis-match of the InN and GaN bonds but also by the fact that nitrogen has a very high equilibrium vapour pressure (EVP) over InN. At the normal growth temperatures of GaN (~750°C for MBE growth) the EVP of nitrogen is more than ten orders of magnitude greater than GaN [7]. The growth temperature must be lowered as to prevent dissociation. Unfortunately lowering the temperature increases the opportunity for indium droplets to form which may act as sinks for InN growth and therefore prevent further indium incorporation in the crystal. The lower temperatures also affect the crystalline quality of the film, because of the reduced mobility of the adatoms during the growth process.

Figure 5.2 shows photoluminescence spectra dependence on the indium fraction for

thin films grown by metal organic vapour phase epitaxy [8]. The GaN films show a sharp, strong peak at 365nm corresponding to the band to band emission. As the indium content increases the peak intensity weakened and shifted towards longer wavelengths. The shift is indicative of a reduction of the band gap, which is anticipated with increasing indium content.

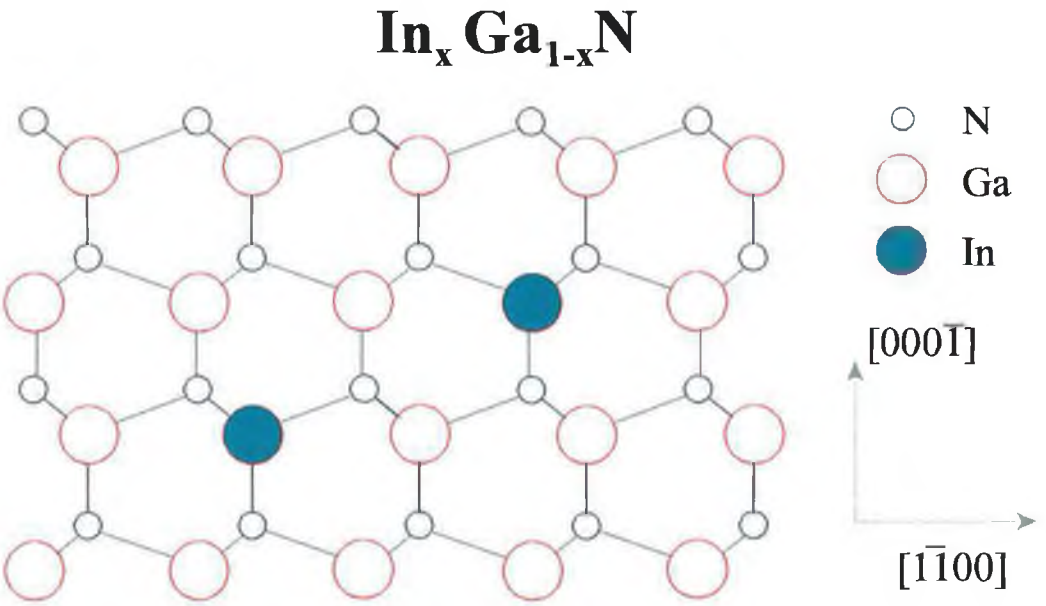

Figure 5.1 : A ball and stick model of the basic construction of the $In_xGa_{1-x}N$ crystal. The indium introduced to the sample during growth randomly sits at a cation site, with the remaining sites occupied by gallium. The anion site remains occupied by nitrogen.

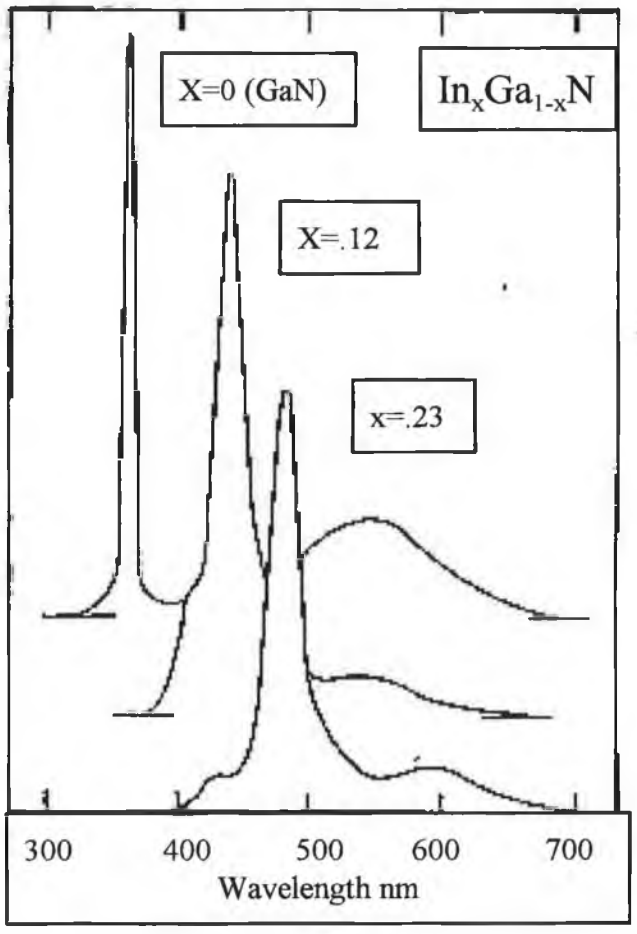

Figure 5.2 : Photoluminescence spectra showing its dependence on the indium fraction within the InGaN ternary alloy [8].

5.2 : Summary of Experimental Work

The electronic structure of a series of $In_xGa_{1-x}N$ ($0 \leq x \leq .3$) alloys have been studied. Using linearly polarised synchrotron radiation excited soft x-ray emission and absorption spectroscopies, the partial density of states (PDOS) of the valence and conduction bands were studied. There is evidence that the conduction band broadens considerably with increasing indium incorporation in both Ga L and N K absorption spectra. The evolution of the band gap as a function of indium content derives primarily from this broadening of

the conduction band states. The N K emission spectra indicates that the valence band only makes a small contribution to changes in the band gap. This gap evolution differs from previous studies on the $Al_xGa_{1-x}N$ alloy system [9], which observed a linear valence band shift through the series ($0 \leq x \leq 1$), and no contribution from the conduction band to the gap evolution. Evidence of a possible In 4d -N 2p hybridisation resonant feature is reported along with previously reported Ga 3d - N 2p hybridisation [9, 10]. The thermal stability of the valence and conduction bands of an $In._{11}Ga._{89}N$ crystal was investigated. Both emission and absorption spectra were found to have a temperature dependent shift in energy, but the overall definition of the spectra was unaltered even at annealing temperatures well beyond the growth temperature of the crystal.

5.3 : Experimental Introduction

Nitride based wide band gap semiconductors have had a large technological impact due to their potential applications as light emitting devices coupled with their extreme hardness and the ability to sustain high temperatures [1, 11-14]. The proto-typical nitride semiconductor GaN, with a band gap of 3.4eV has a very large typical defect density, ~10^8 - 10^{10} cm^{-2}, compared to 10^3 cm^{-2} for ZnSe, the previous leading candidate for an operational wide band gap semiconductor [1]. The high level of defects gives an understanding of the typical surface one may expect. The most common investigative tools for probing the electronic structure are photoemission based, i.e. angle resolved and inverse photoemission. These techniques are very surface sensitive, and the ability to prepare clean ordered surfaces is critical.

Introductory studies into the preparation of more complex ternary nitride alloy surfaces indicate much work needs to be done, and until a systematic approach for preparing clean, bulk terminated surfaces has been achieved, photoemission based studies aimed at probing the electronic structure of these materials will not realise its full potential.

On the other hand, x-ray based techniques are not surface sensitive, and both x-ray emission and absorption spectroscopies probe the partial density of states of both the valence and conduction bands respectively. Recent studies have taken the opportunity to investigate the electronic structure of nitrides [9, 10]. Stagarescu et al [10] first investigated thin MBE grown GaN films, but the more complicated the alloy, the greater the advantage of the bulk sensitive techniques as the surface preparation becomes far more complicated.

An important potential application of nitride ternary alloys in the foreseeable future is the ability to control the direct band gap, from 1.9eV (InN) through 3.4eV(GaN) to 6.2eV(AlN). If this potential were realised it would have an important technological impact on the semiconductor optoelectronic industry. A greater understanding of the evolution of the electronic band structure of the AlGaN alloy system was obtained when Duda et al [9] investigated a series of samples ranging from AlN to GaN. As a natural progression the band evolution of the GaN based ternary alloy InGaN was studied in this thesis. The recent success of multi-quantum well structures to lase in the blue, using InGaN as the optically active layers within multi and single quantum well devices, [2] has led to intense interest in these structures, due to a lack of understanding of the actual luminescence process [1, 15].

5.4 : Experimental Details

The samples investigated were thin films of ~1μm, $In_xGa_{1-x}N$ ($0 \leq x \leq .3$) grown by electron cyclotron resonance assisted molecular beam epitaxy on sapphire substrates with a GaN buffer layer. X-ray diffraction (XRD) and photoluminescence (PL) were used to obtain the structural and operative quality of the samples. XRD was also used to obtain the In and Ga ratios [6].

The experiments were performed on the undulator beamline X1B at NSLS, BNL. Absorption spectra were measured by either the sample drain current or by the total flourescent yield (TEY) and were taken with energy resolutions of ~.2eV at 400eV at the

N 1s absorption edge. This resolution is defined by the incident photon beam, determined by the beamline (monochromator and entrance and exit slits). During the x-ray emission experiments, however the resolution of the incoming photon beam was set between ~0.3eV and >1eV. This lower resolution was used in order to compensate for the low count rate from the weak process of soft x-ray emission when compared to competing non-radiative de-excitation processes. Emission spectra were recorded using a Nordgren type grazing-incidence grating spectrometer. The spherical grating had a 5m radius of curvature with 1200 lines/mm [16, 17]. N K emission (~400eV) was recorded in first order of diffraction at a resolution of ~0.31eV. To detect Ga L emission (~1000eV) the spectrometer used second order diffraction with a resolution of ~0.8eV [16, 17]. The average acquisition time for spectra was 90 mins. The base pressure of the analysis chamber was $8x10^{-10}$Torr.

The elementally and orbitally resolved valence and conduction band density of states are probed by the combination of the emission and absorption of N K and Ga L spectra. Both procedures acquire their relevant data separately as described but may be presented on a combined graph with a common energy axis. The emission data is recorded as a pixel position on the multichannel detector and in order to calibrate the spectra, two reference points are required. Often the elastically scattered incident photons can be detected, and therefore by changing the incident photon energies, the detector can be calibrated for that specific energy range. In effect the absorption and emission spectra are then both referenced to the energy calibration of the beamline monochromator. The zero energy position is then set to the valence band maximum, as the precision of the absolute energy scale is not vital. Once the spectrometer is calibrated for a specific energy range, all subsequent spectra are similarly calibrated. If the elastic peak is not visible then reference samples are required to calibrate the emission spectra. For the N K emission, the second order emission of both cobalt Lα, and β are used to reference both absolute and relative photon emission energy. The Ga Lα emission spectral set up is calibrated by detecting both Ga Lα and β, from GaN,

the separation of the two emission lines is the spin orbit split of GaN 26.9eV [10].

If reference samples are used, the absorption and emission spectra do not have a common reference energy. To share a common binding energy scale, the energy axis for N K is referenced to the valence band maximum of the N2p PDOS and the absorption edge set to the theoretical band gap value of GaN. Although the Ga Lα emission and absorption spectra are presented in photon energy, they may be presented on a common binding energy axis determined by the Ga band gap derived by theoretical calculations [10].

5.5 : Results and Discussion

5.5.1 : Band Evolution

Figure 5.3 shows both emission and absorption spectra of the N 2p derived occupied and unoccupied bands respectively. The dashed lines indicate movements of the band edges as a function of indium content. The energy axis is referenced to the valence band maximum of GaN, which is estimated by extrapolating the leading edges of the absorption and emission spectra and the band gap is set to 3.4eV. The sample series is limited due to the difficulty in growing high quality InGaN with an indium content beyond ~$In_{.35}Ga_{.65}N$ as the sample begins to phase separate into both InN and GaN.

Figure 5.3 clearly indicates the N 2p derived band gap evolution of the series. The emission spectra which represents the occupied valence band states, shows the edge shifting by .15eV to lower binding energies with x=.1, but with no appreciable shift occurring beyond this point. The unoccupied states indicated by the absorption spectra were taken at grazing incidence, and show considerable band edge movements with increasing indium content. Figure 5.4 shows a clearer illustration of the conduction band movement, where the absorption spectra were taken at normal incidence. From figure 5.4 (a) it is noted that the spectral features shift with changing indium content. The conduction band edge movement seems to derive mostly from the broadening of the existing spectral feature A,

figure 5.4 (b). Figure 5.5 plots the band gap with respect to the indium content. A best fit line of the data points is compared to a straight line from GaN to InN band gaps. The diagram clearly shows a large deviation from a linear gap evolution.

The concept of calculating the gap size with elemental concentrations within ternary alloys has been typically described by Vegaard's law, a parabolic function of the molar fraction, x [18],

$$Eg(x) = \bar{E}g + \Delta Eg(x - \tfrac{1}{2}) - bx(1 - x)$$

Where Eg is the resultant gap of a specific sample in a series, $\bar{E}g$ is the average gap, ΔEg is the difference between the gaps of the pure end members of the alloy system, and b is the bowing parameter. The bowing parameter allows for the deviation from the expected linear behavior of the band gap through the ternary system.

First principle calculation results of 1.02eV [19]and 3.8eV [20] have been obtained for the bowing parameter of InGaN series, and the band gap evolution illustrated by figure 5.5 would indicate a very large downward bowing factor. Although, Vegaards law did not satisfactorily fit the gap evolution presented here. It has been suggested that the bowing term x(1-x) is reasonable only when based on the assumption that the mixed crystal is an ideal solution and the crystal lattice changes gradually through the ternary alloy system [21]. Due to the In-N and Ga-N bond length difference (~10.8%) the atom positions are considered to fluctuate from the perfect lattice sites leaving both bond length and bond angle distortions in the alloy. While phase separation is well documented particularly in InGaN alloys with higher indium content [4-6], a theoretical analysis of a relatively low indium content model ($In._2Ga._8N$) alloy revealed random alloying or 'alloy disorder' as opposed to complete phase separation [3]. This disorder may account for this alloy systems lack of adherence to Vegaards law, even with low indium content. The band gap evolution of GaN-InN also depends heavily on the growth parameters, in particular the growth temperature as described by Kalashnikov et al [21] where calculations show the complete

closure of the gap at elevated growth temperatures of 1100^{0}C.

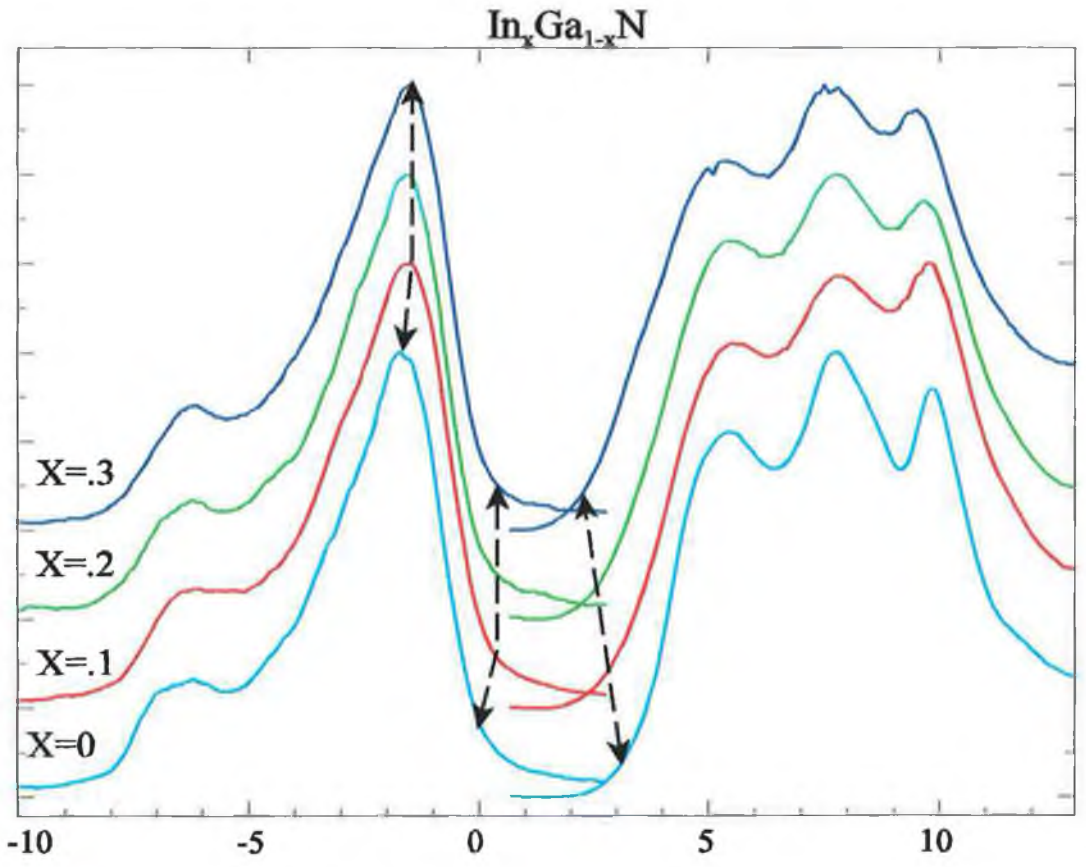

Figure 5.3 : X-ray emission and absorption spectra indicating the N 2p derived valence and conduction bands of a series of $In_xGa_{1-x}N$ samples. Dashed lines help guide the eye following gap edges. The energy axis is set with respect to the valence band maximum of GaN. The absorption spectra were taken at grazing incidence.

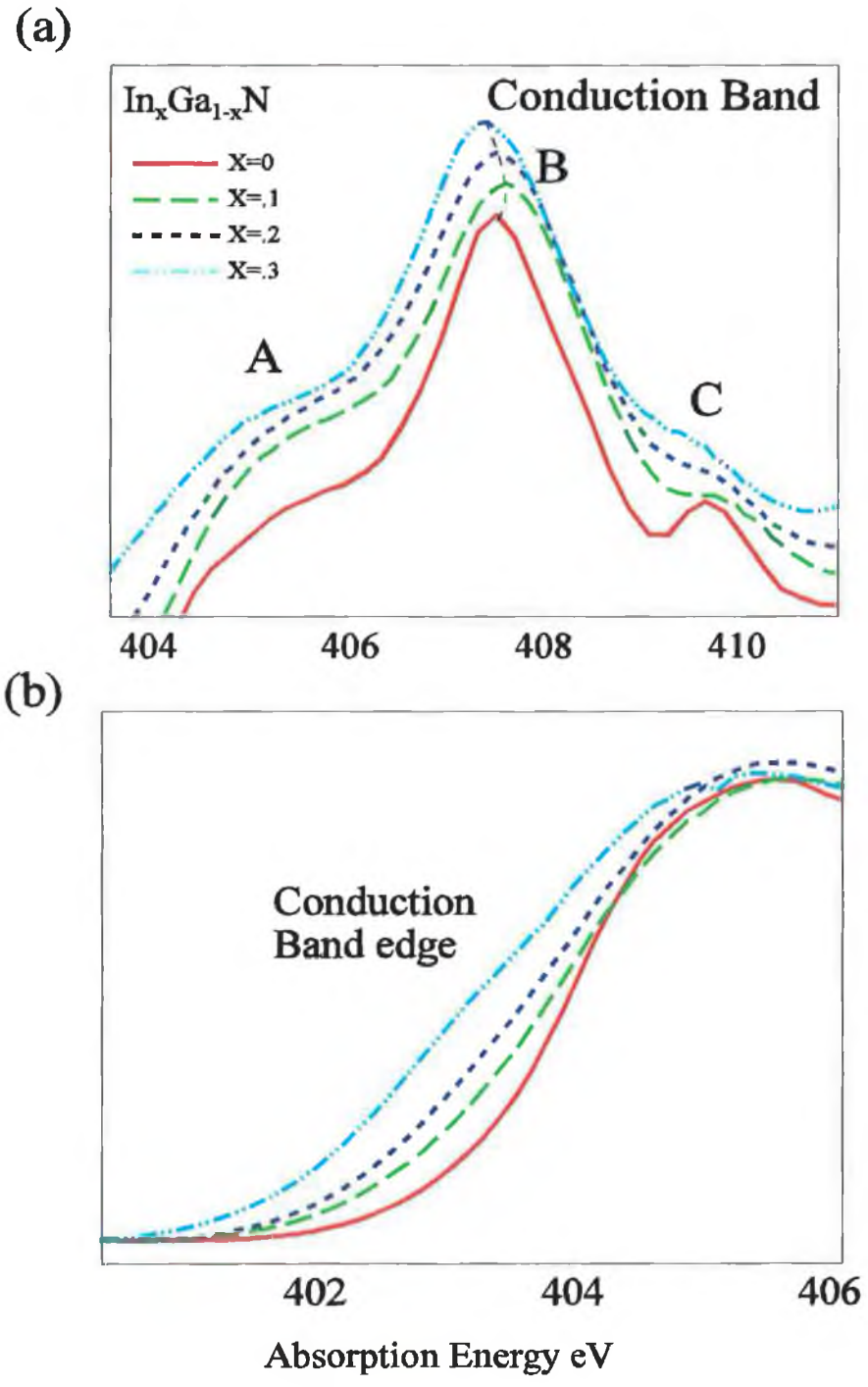

Figure 5.4 : On closer inspection of the N 2p derived conduction band states, (a) shows a dynamic shifting of the absorption features. The relative intensities have been shifted as to indicate the movement of the spectral features (b) The conduction band minimum edge shifts to lower energies closing the gap with increasing indium content. The absorption spectra shown were taken at normal incidence.

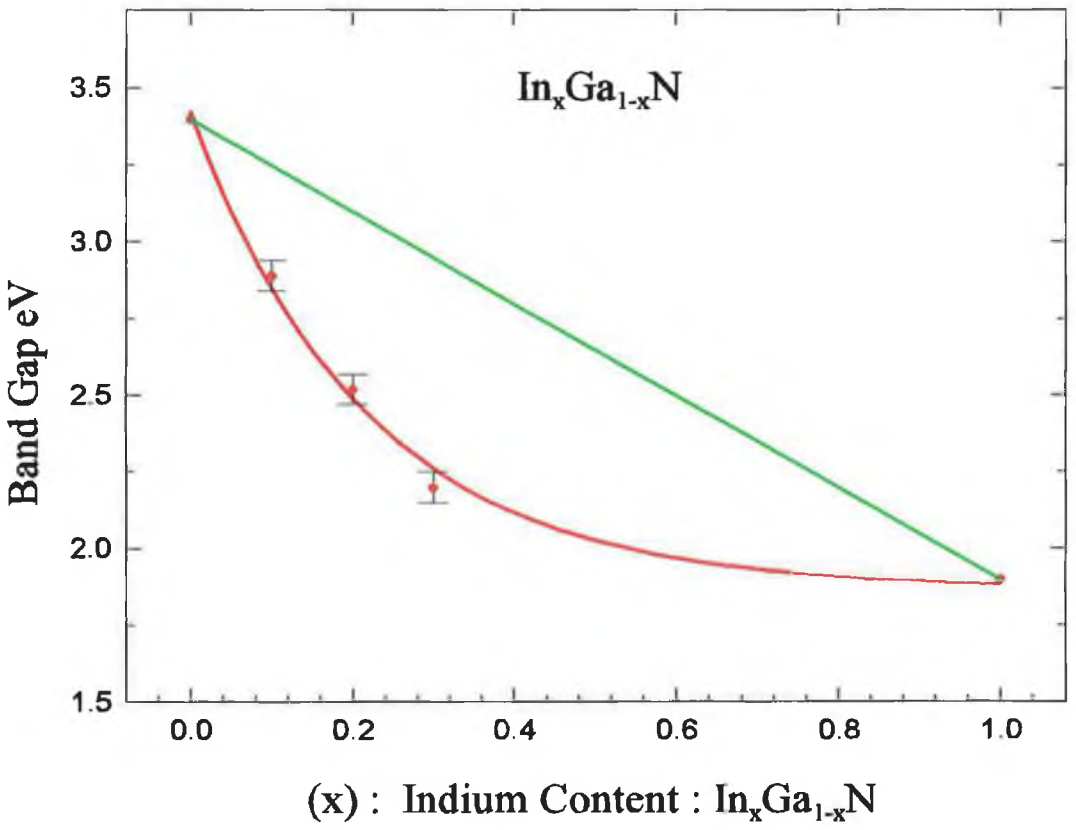

Figure 5.5 : This illustration shows the band gap evolution by measuring the band edge shifts of the emission and absorption spectra. The green line shows a straight line between the known band gaps of both GaN (3.4eV) and InN (1.9eV). The red line is a best fit line of the data including both GaN and InN band gaps.

The previous studies of the AlGaN alloy system indicated the gap evolution process differed from that of the InGaN system [9]. Figure 5.6 illustrates a series of emission spectra showing the valence band evolution as the alloy tends from GaN to AlN. The valence band edge movement is used to measure the net band gap change. In complete contrast to the $In_xGa_{1-x}N$ series the absorption spectra of the $Al_xGa_{1-x}N$ showed no energy movement through the series. The valence band shifts through the AlGaN system was, within experimental error, linear and as such the band evolution with respect to Vegaard's

law would have a zero bowing parameter.

While N 2p states dominate the top of the valence band, the bottom of the conduction band is a mixture of both Ga 4s and N 2p states. Ga 3d and Ga 4s states both contribute to the overall electronic band structure of the system. Figure 5.7 (a) shows the x-ray emission results of the Ga Lα line, resulting in the de-excitation from Ga 3d and 4s states to the 2p3/2 and 5.7(b) Ga L absorption of 2p3/2 to both Ga 3d and 4s states. The main feature in 5.7 (a) indicates the Ga 3d contribution and the inset shows the Ga 4s density of states. The absorption spectra also result from both Ga 3d and 4s density of states and were obtained using the total flourescent mode. The Ga 3d is regarded as a quasi-valent state [10, 22] as it has a relatively large binding energy, 18.8eV. Table 1 notes the FWHM of the Ga Lα feature which remains constant between GaN and $In_{.1}Ga_{.9}N$, indicating no change in the Ga atomic localisation. With further indium content, a sharp increase in FWHM occurs. The Ga 4s also has a minor contribution to the valence band structure and appears with a low density of states at lower binding energy. The Ga 4s emission spectra show a valence band maximum shift but the intensity is very low and the movement is difficult to ascertain. The absorption spectra show a clear and gradual loss of feature definition indicating consistent broadening as the indium content increases, this compares with the Ga 3d emission broadening, which was not gradual with respect to the indium content.

Table 1 : Ga Lα

Sample	GaN	$In_{.1}Ga_{.9}N$	$In_{.2}Ga_{.8}N$	$In_{.3}Ga_{.7}N$
FWHM	**3.13eV**	**3.13eV**	**3.59eV**	**3.71eV**

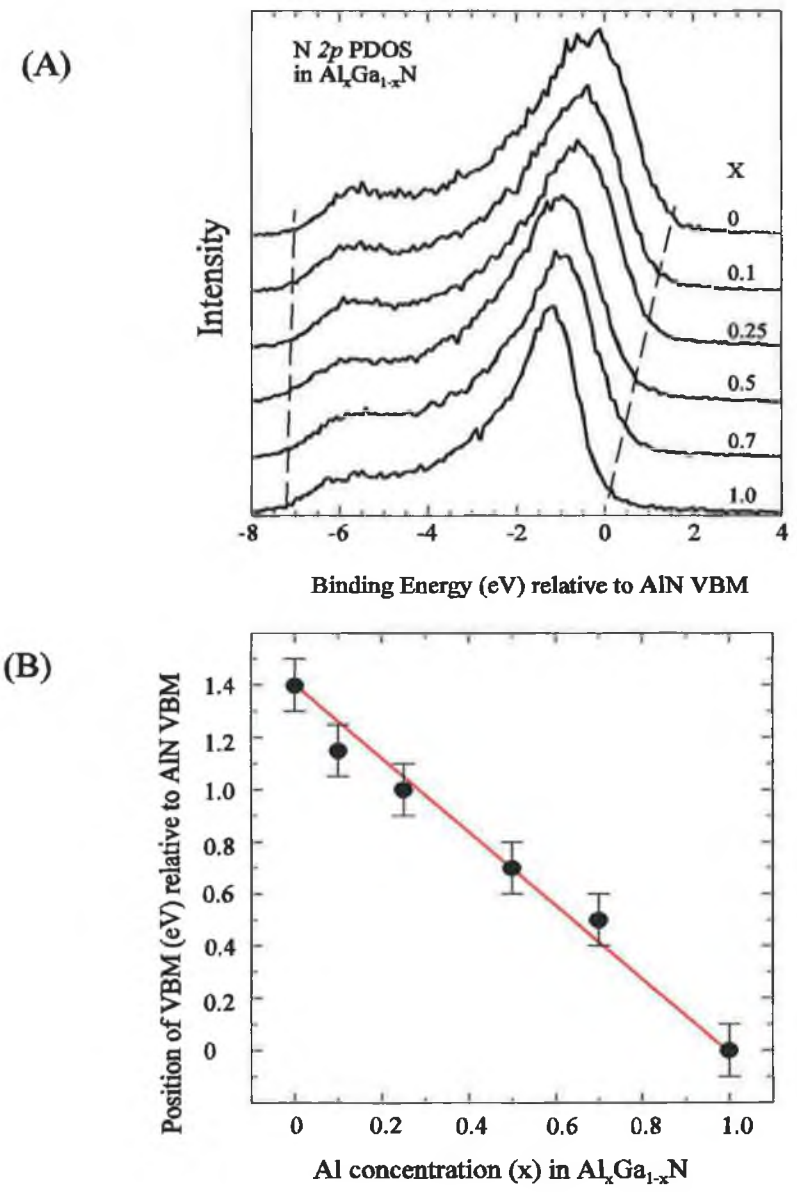

Figure 5.6 : (A) N K emission spectra from $AlxGa_{1-x}N$. Only the valence band is shown. The spectra are plotted relative to the binding energy of the valence band maximum(VBM) of pure ALN. (B) Data points indicate the position of the experimentally determined VBM of the N 2p PDOS as a function of x. The straight line is the gap evolution with a zero bowing factor.

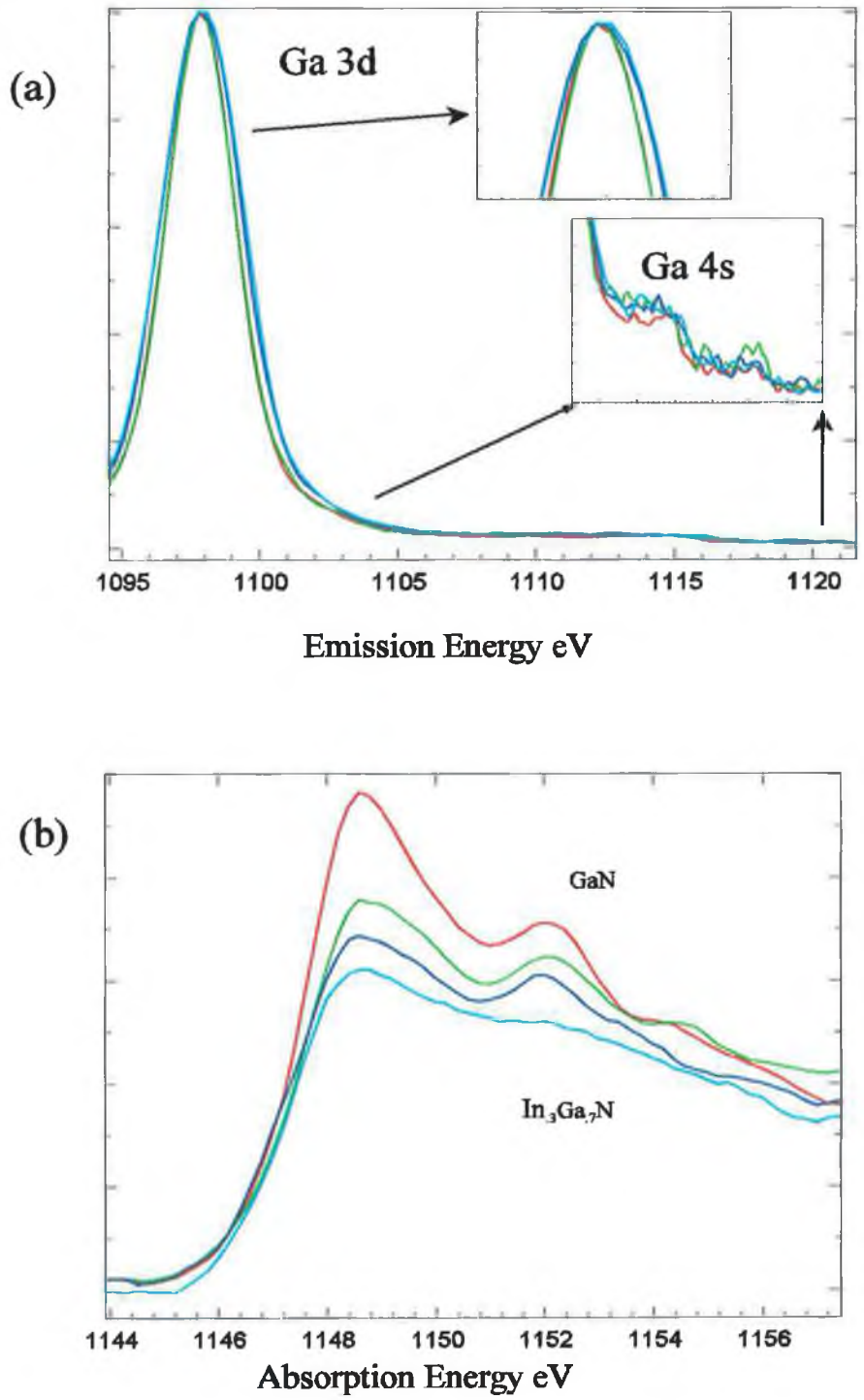

Figure 5.7 : (A) Ga Lα Emission of the InGaN series. Insets showing, Ga 4s shelf towards VBM, and Ga 3d PDOS valence band edge. (B) Total flourescent yield absorption spectra of the same series, indicating the Ga 4s and 3d partial density of states.

5.5.2 : Angle Dependent XAS spectra

The absorption spectra correspond to the interdependence of incident light polarisation direction and the electron core level orientation. This is due to the scalar multiplication in the matrix element of the absorption cross-section between the polarisation vector of the incident photon e and the position vector of the core level r [23],

$$M = \langle \varphi_f | \, e.r \, | \varphi_i \rangle$$

Figure 5.8 shows N K absorption for AlN, clearly showing the orientation dependence of peak B. The spectra have been normalised by equating the background on either side of the absorption edge. A simultaneous mesh current of the incident beam taken with the absorption spectra is subtracted to remove the energy dependent incident photon intensity resulting from the undulator transmission characteristics.

The absorption spectra are not only element and orbital symmetry specific but also orientation dependent when the source is linearly polarised. The films under investigation are wurtzite (hexagonal) and the c-axis coincides with the sample normal. Consequently transitions between the N 1s and N $2p_z$ (out of plane (0001) orbitals) are forbidden when the polarisation vector of the source (e) is perpendicular to the c-axis, and the transition from N 1s to N $2p_{x,y}$ or in plane orbitals are forbidden when e is parallel to the c-axis [23, 24].

Figure 5.9 shows the angular dependence of the absorption spectra, comparing both GaN and $In._3Ga._7N$ acquired in this study. Katsikini et al [25, 26] reported near edge absorption studies of several phases of GaN. The changing feature intensities helped attribute specific orbital characteristics to the absorption features, as indicated in the figure caption.

It is noted that the energy position of the spectral features shift with changing incidence angle. This is particularly noticeable with feature C, as the incidence angle approaches the surface normal, the energy position increases.

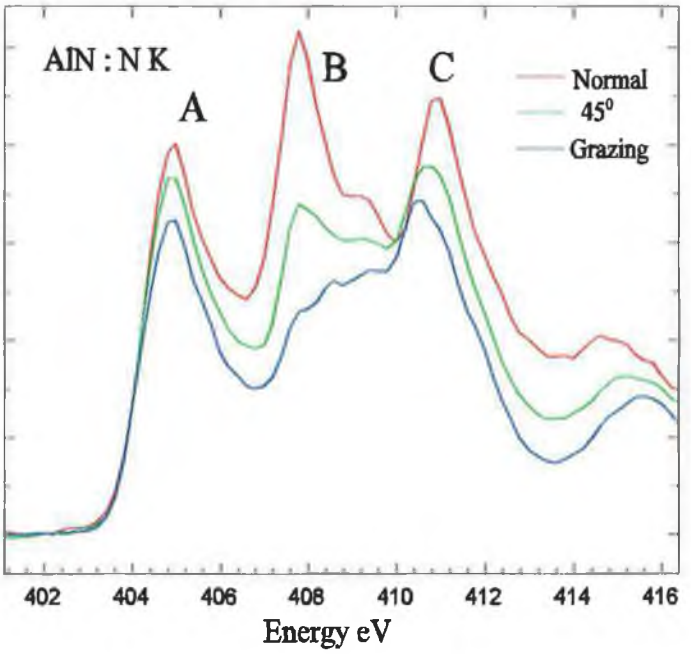

Figure 5.8 : N K absorption spectra of AlN showing the incident angular dependence of the spectral intensity.

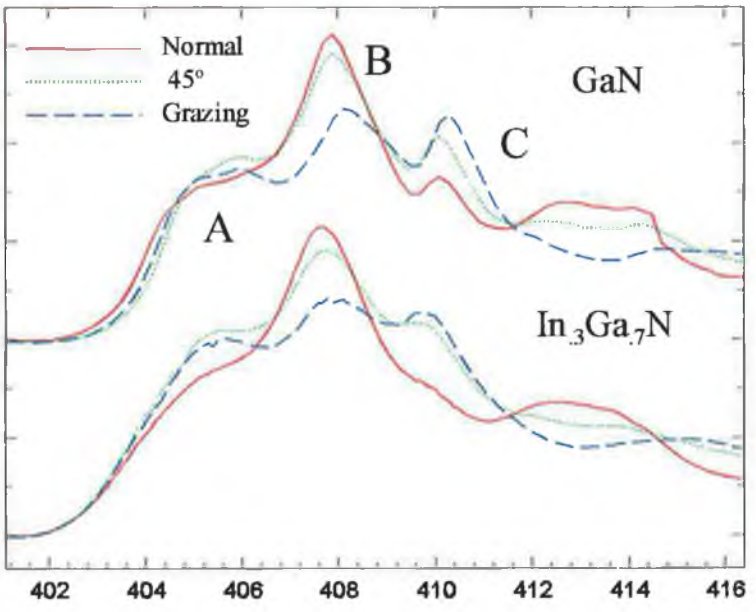

Figure 5.9 : Changing incident angles, helps to indicate the orbital nature of the absorption features. Katsikini et al [25] noted the same features with EXAFS and had ascertained the following orbital characteristics for the three main features :

$A = (s+p_z)$: $B = (p_x+p_y)$ $C = (s+p_z)$

Lawniczak-Jablonska et al [23] investigated the polarisation dependence of InN, AlN, and GaN, of both cubic and hexagonal structures. While the cubic structures indicated little polarisation dependence, the hexagonal structures showed a cation dependent angular distribution. Even though all three nitride compounds have the same tetrahedral structure, the angular dependence differs greatly between them. While GaN shows qualitative spectral changes, the overall spectral area remains relatively constant. For InN on the other hand, the total spectral intensity depends heavily on the angle of incidence. This dependence indicates the relative energy distribution of the nitrogen antibonding states and also indicates the ratios of 'in plane' (0001) and 'out of plane' orbitals, where there is expected to be a higher density of in plane bonds than out of plane. Although the ability to change the polarisation direction of the source was not available, but by rotating the sample, the incident beam could be varied between surface grazing and surface normal, in doing, the polarisation switches from parallel to perpendicular to the c-axis of the sample. Lawniczak-Jablonska et al [23] reported that GaN displayed weak anisotropic behavior but a strong effect was seen for InN. It is evident that there is a cation dependent anisotropic effect. Figure 5.9 shows qualitative angular changes for the GaN sample but the total spectral area remains relatively constant as reported by Lawniczak-Jablonska et al [23]. The $In_{.3}Ga_{.7}N$ sample showed an identical angular dependence. Thus the structure seems to retain the weak anisotropic character typical of GaN and does not obtain any of the strong anisotropic nature of InN. A disadvantage of rotating the sample to control the polarisation rather than changing the polarisation of the incident beam is that the spot size on the sample considerably increases with incident grazing angle, therefore the count rate may be increased and thus the total intensity of the spectra. This effect may cancel out any expected intensity decreases.

5.5.3 : Hybridisation

Stagarescu et al [10] first reported an emission feature ~18eV below the valence band maximum of the N K emission of MBE grown GaN thin films. This feature was weak but reproducible. It was suggested to be a quasi-valent Ga 3d - N 2p hybridised state, thus allowing the de-excitation from Ga 3d to the N 1s core level. The hybridisation effect identifies the mixture of different electronic orbitals which subsequently obtain the characteristics of the orbitals with which they overlap.

Figure 5.10 shows an overlay of the Ga Lα and N K emission results. The spectra have been aligned along the VBM of both spectra. The weak resonant feature is measured at ~19-20eV from the N 2p valence band maximum, this compares with the binding energy of Ga 3d of 18.7eV and when overlapped with the Ga emission spectra, the resonant feature matches the Ga 3d binding energy relative to the Ga valence band maximum.

Duda et al [9], confirmed this feature to originate as a result of Ga 3d - N 2p hybridisation. Figure 5.11 presents a series of emission spectra of AlGaN alloys from AlN to GaN. As the gallium content decreases so too does the signature of the resonant feature.

Figure 5.12 also shows a clear indication of the Ga 3d - N 2p resonant feature at ~19eV. At $In._2Ga._8N$ the hybridisation feature broadens and shows a tail on the lower binding energy side of the peak. The binding energy of Ga 3d is 18.8eV, and the spin orbit splitting is very small, thus the associated resonant hybrid state is a relatively sharp peak. With increasing In content the feature broadens and may be explained by an In 4d - N 2p hybridisation state. It is noted that the binding energy of In 4d which is spin orbit split by 1.3eV at 17.7eV and 16.4eV for $4d_{3/2}$ and $4d_{5/2}$ respectively, both these features along with the remaining Ga 3d resonant peak results in the emergence of a relatively broad feature. This is the first reported evidence of In 4d - N 2p hybridisation noted with this technique.

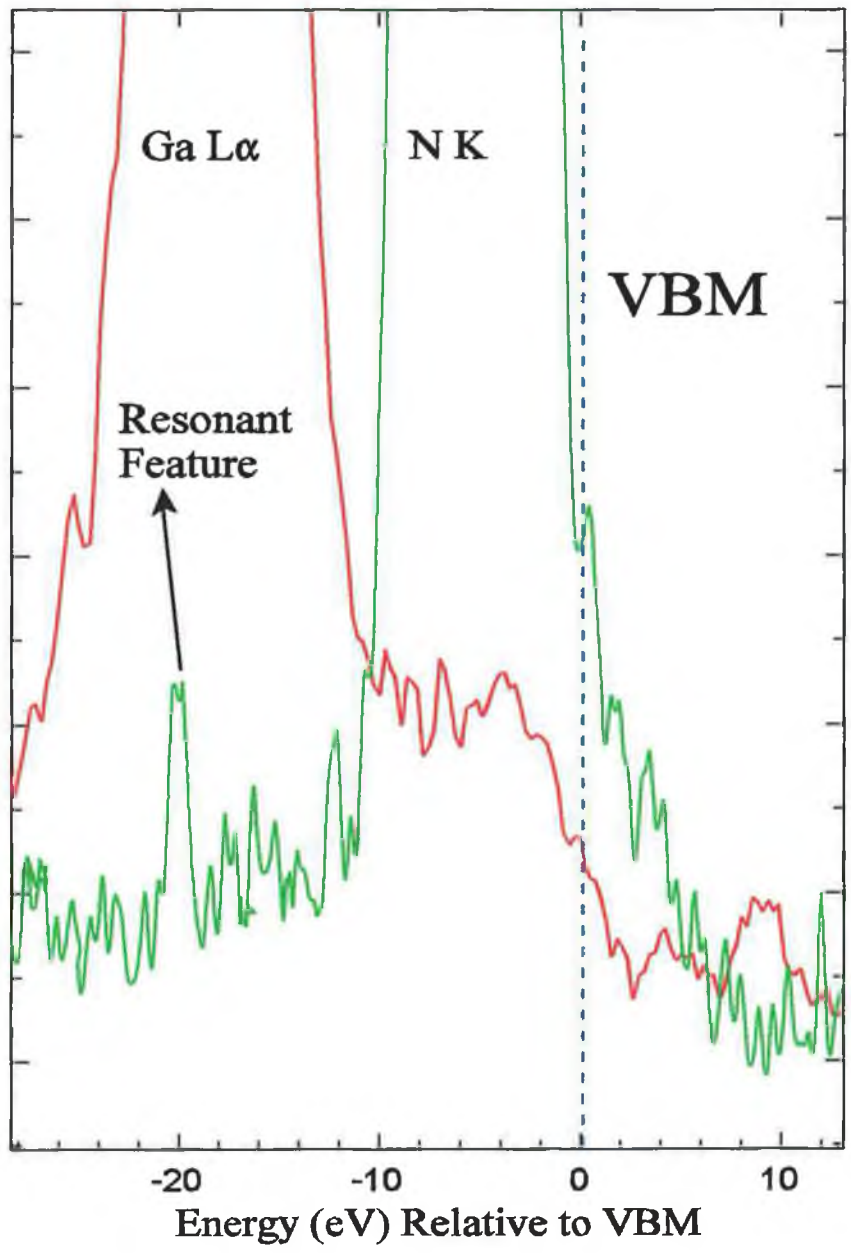

Figure 5.10 : An overlay of Ga Lα and N K emission spectra from $In_{.1}Ga_{.9}N$ sample, showing the resonant feature indicating the hybridisation between the Ga 3d and N 2p states.

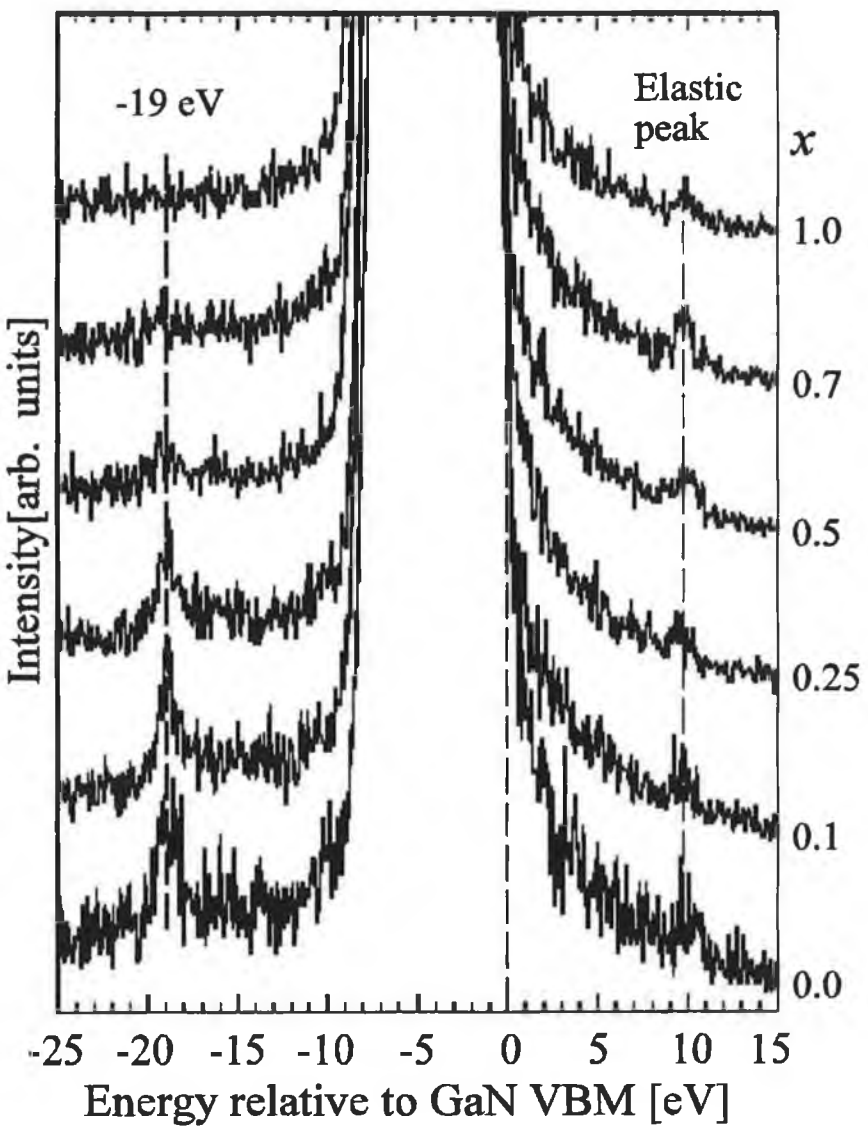

Figure 5.11 : N K emission spectra from $Al_xGa_{1-x}N$ series. The resonant hybridisation feature at ~19eV below the GaN VBM gets weaker and disappears as the Ga content is reduced, thus signifying its origin as N 2p states hybridised with Ga 3d states [9].

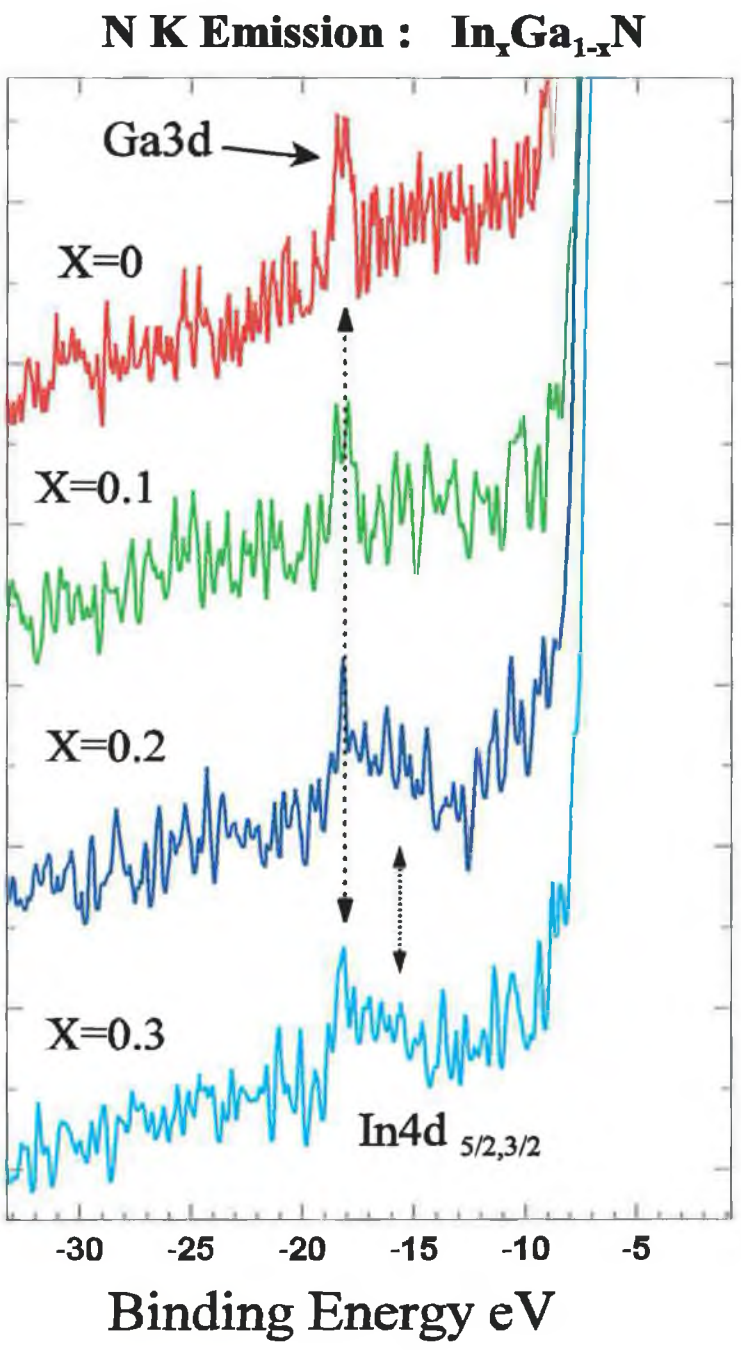

Figure 5.12 : The first indication using XES of hybridisation between In 4d and N 2p states, also showing hybridisation between Ga 3d and N 2p.

5.5.4 : Thermal stability of the bands

Wide band gap nitride alloys are known to have a high structural stability at elevated temperatures, and therefore have the potential for high temperature optoelectronic device applications. Although InGaN has a propensity to phase separate, particularly at high indium content [4-6]. A growth phase diagram formulated by Ho et al [27] illustrates the growth stability of the InN-GaN quasi-binary system with respect to indium content and growth temperatures. From this formulation the stability of the grown crystal may be predicted. Doppalapudi et al [6] grew samples both in the stable and unstable regions of the phase diagram and verified the predictions using x-ray diffraction measurements. Within this study the samples were also annealed at ~725°C for 20 hours, and found further phase separation of the 'unstable' crystals, while the 'stable' samples remained structurally intact. This annealing procedure was performed at atmospheric pressure in nitrogen ambient conditions to replenish any preferential loss of nitrogen.

The effect of high temperatures on the density of states of the bands of a known 'stable' (i.e. grown in the stable region of the InGaN system) was studied. An ECR-MBE grown $In_{.11}Ga_{.89}N$ sample was electron beam heated to 610°C, just below its growth temperature of ~700°C-750°C, then to 780°C, just above the growth temperature and then 980°C, well beyond the growth temperature. The sample was heated for an hour at each temperature and then cooled to room temperature and both x-ray emission and absorption spectra were taken. The annealing procedure was performed in vacuum at $\sim 1 \times 10^{-8}$T without a nitrogen atmosphere, so any nitrogen loss would be accentuated.

Figure 5.13 shows both emission and absorption spectra of the N 2p valence and conduction band density of states through the annealing series. The qualitative features of the spectra are unaffected with almost no broadening effects, and as such the features loose none of their clarity or resolution.

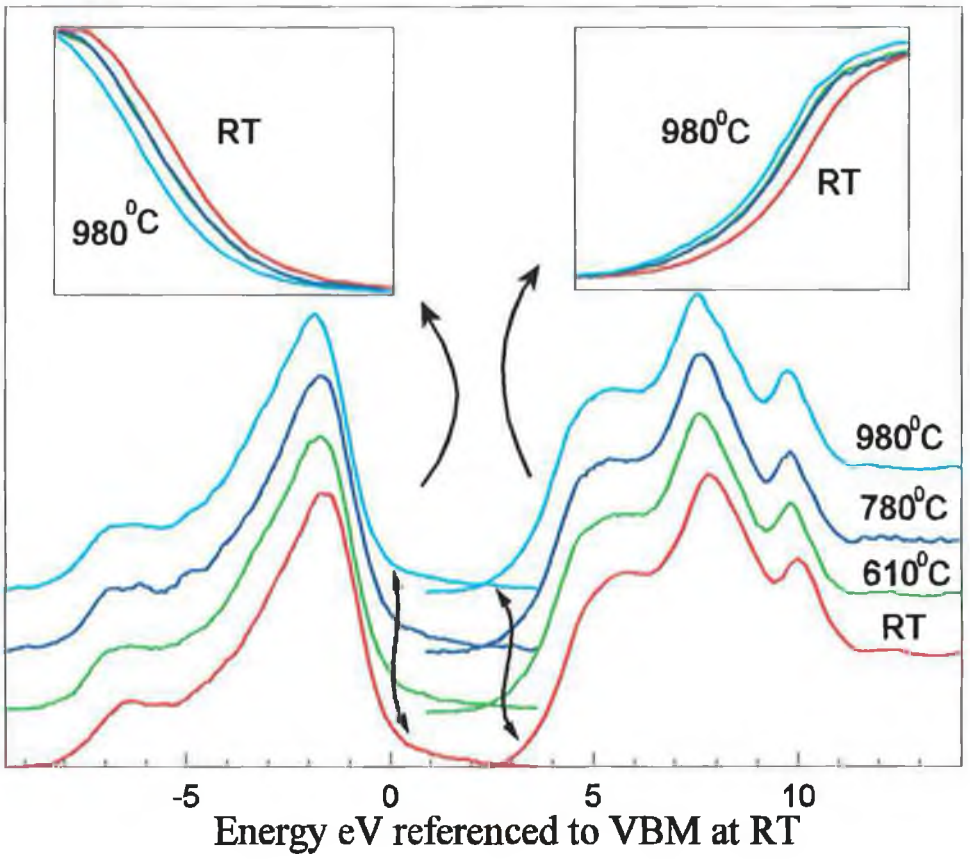

Figure 5.13 : N 2p PDOS of both the valence and conduction bands, of an $In._{11}Ga._{89}N$ sample annealed to several temperatures to investigate the thermal stability of the bands.

Both spectral series follow an almost identical shifting sequence. The insets show a comparison of the N 2p valence band maximum and conduction band minimum at the different temperatures. After annealing to 610°C both spectra exhibit a decrease in energy. Annealing to 780°C indicated no spectral shift. But another similar shift (to a lesser extent in the absorption spectra) is evident after annealing to 980°C. The stability of the bands at high temperatures is evident from the consistent spectral shape. The band shifting sequence is not understood but as each technique is independent, the shift sequence is real. The two most likely effects which may occur due to annealing are InN evaporation and preferential nitrogen loss. The loss of InN would require phase separation, and as the sample was

selected to avoid this, it seems unlikely. It is assumed that there was a certain loss of nitrogen, and if the subsequent structural change causes the spectral energy shifts, the physical process is not clear.

5.6 : Conclusion

The evolution of the partial density of states from the N 2p derived conduction and valence bands of an $In_xGa_{1-x}N$ ($0 \leq x \leq .3$) series has been investigated. The valence band shows very little change with increasing indium content. A shift of 0.15eV at $x = 0.1$, with no significant movement thereafter. The absorption spectra indicated a high degree of broadening, this effect indicates a decrease in the atomic nitrogen localisation, primarily caused by the random alloying in the crystal with increasing indium content. What is not understood is the absence of broadening within the N K emission spectra, and the lack of movement through the series. The Ga Lα emission feature did show a degree of broadening, although only when the indium content increased to $x = 0.1$, and the Ga absorption spectra indicated a gradual broadening through the series.

The N 2p band gap evolution process of both AlGaN and InGaN systems differ dramatically. The emission spectral series (figure 5.6) shows the expected linear movement following the band gap evolution through the $Al_xGa_{1-x}N$ ($0 \leq x \leq 1$) alloy series, while no shift of the absorption edge was recorded. The valence band of the InGaN series did not show the expected spectral shift, but the conduction band edge shifted depicting the gap evolution process.

The thermal stability of an $In_{.11}Ga_{.89}N$ sample grown within the stable parameters depicted by the growth phase diagram of Ho et al [27] was investigated and indicated remarkable stability at elevated temperatures beyond the growth temperature of the crystal. Although a temperature dependent shift of both the emission and absorption spectra was noted, the physical reason is not understood.

It is interesting to note that as far back as 1972 [28] optical absorption studies were

performed, investigating the band gap evolution of polycrystalline $In_xGa_{1-x}N$ samples. Figure 5.14 indicates band gap measurements by noting the edge of optical absorption measurements through the $In_xGa_{1-x}N$ alloy series. There is clear evidence of a downward band bowing factor as described by Vegaards law. The improved crystal quality of the MBE grown samples may introduce effects such as strain induced by the previously mentioned random alloying effects which a polycrystalline sample would not experience, and may be the reason for the band evolutions non-compliance with Vegaards law.

The introduction of the indium and the corresponding level of 'alloy disorder' indicated by the broadening of the absorption spectra suggests a degree of spatial dependent variation of the conduction band minimum throughout the crystal. The broadening of the PL emission in figure 5.2 indicates the result of this effect to the band gap of the material i.e. a broadening of the luminescence signature.

The origin of the luminesce quality of InGaN crystals is still unclear [15], particularly the successful InGaN based multi quantum well devices [2] and its apparent indifference to the very high density of structural defects [29]. More recently Stoke shifts between optical emission and absorption measurements of InGaN quantum well based devices have indicated an obscure source of luminescence. It is suggested that both spontaneous and stimulated emission originates from deep localised energy states induced by indium rich InGaN assembled nano sized particles [1]. Using high resolution transition electron microscopy, a periodic indium composition fluctuation was observed [30]. It is thus suggested that the main radiative recombination is attributed to excitons localised at deep traps originating from the indium rich regions forming quantum well dots [30]. This situation is analogous to porous silicon [31] where the luminescent characteristics are attributed to the assembly of free standing Si quantum wires.

Many studies have reported the phase separation of InGaN into InN and GaN [3, 5-7]. At the typical growth temperatures for GaN ~750^{0}C, the equilibrium vapour pressure

of InN is more than ten orders of magnitude greater than GaN [6].This results in the indium having a very low sticking coefficient at these growth temperatures, which therefore have to be reduced to prevent dissociation of InN. At lower temperatures there is a higher risk of In droplets forming and acting as seeds for InN crystals. The lower temperature may also reduce the mobility of ad-atoms on the surface and inhibiting the proper growth of three dimensional crystals. These growth factors are most likely important reasons leading to the possible growth of InN nano crystals.

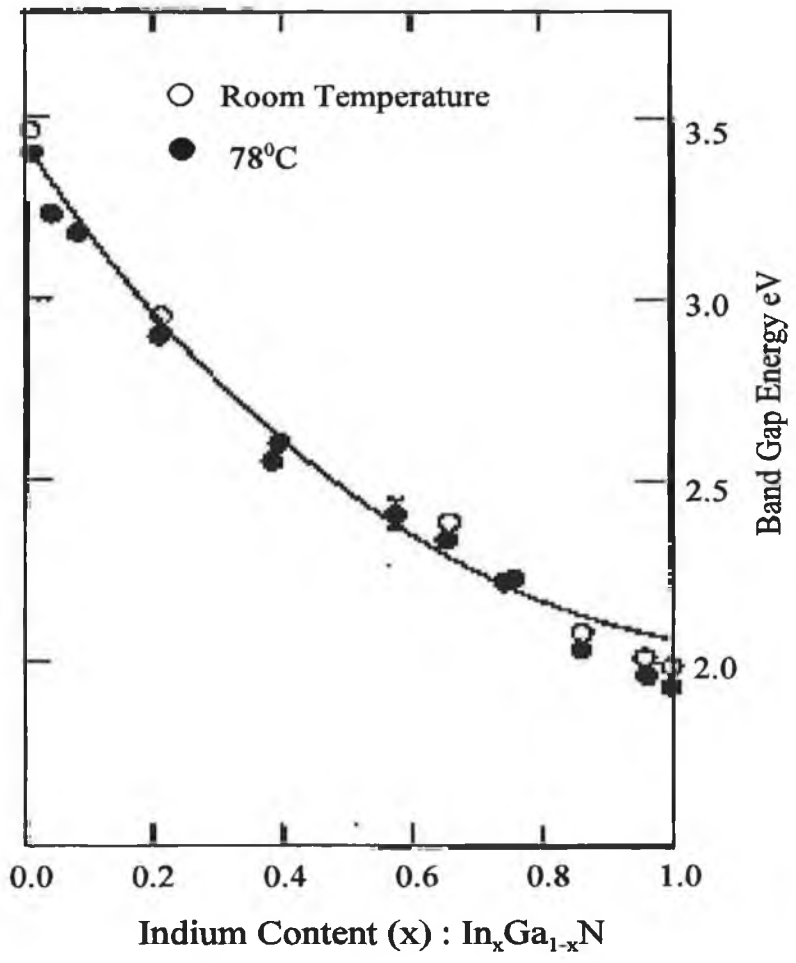

Figure 5.14 :This plot indicates the band gap evolution of polycrystalline $In_xGa_{1-x}N$ by noting the absorption edge from optical absorption measurements [28].

5.7 : References

1. Nakamura, S. and G. Fasol, *The Blue LED*. 1997, Berlin-Heidelberg: Springer.
2. Nakamura, S., *et al.*, *Blue InGaN based laser diodes with an emission wavelength of 450nm.* Appl. Phys. Lett., 1999. **76**(1): p. 22.
3. Singh, R., D. Doppalapudi, and T.D. Moustakas, *Phase separation in InGaN thick films and formation of InGaN/GaN double heterostructures in the entire alloy composition.* Appl. Phys. Lett, 1997. **70**(9): p. 1089.
4. El-Masry, N.A., E.L. Piner, and S.X. Liu, *Phase Separation in InGaN grown by metalorganic chemical vapor deposition.* Appl. Phys. Lett., 1998. **72**(1): p. 40.
5. Doppalapudi, D., *et al.*, *Phase separation and ordering in InGaN alloys grown by molecular beam epitaxy.* J. Appl. Phys, 1998. **84**(3): p. 1389.
6. Saito, T. and Y. Arakawa, *Atomic structure and phase stability of InxGa1-xN random alloys calculated using a valance force field method.* Phys. Rev. B, 1999. **60**(3): p. 1701.
7. Doppalapudi, D., S.N. Basu, and T.D. Moustakas, *Domain structure in chemically ordered InxGa1-xN alloys grown by molecular beam epitaxy.* Jrnl. Appl. Phys, 1999. **85**(2): p. 883.
8. Yoshimoto, N., *et al.*, *Photoluminescence of InGaN films grown at high temperature by metalorganic vapour phase epitaxy.* Appl. Phys. Lett, 1991. **59**: p. 2251.
9. Duda, L.-C., *et al.*, *Density of States, Hybridization, and Bandgap Evolution in $Al_xGa_{1-x}N$ Alloys.* Physical Review B, 1998. **58**: p. 1928.
10. Stagarescu, C.B., *et al.*, *Bulk Electronic Structure of GaN measured using Soft X-ray Emission and Absorption.* Physical Review B, 1996. **54**: p. 17335.
11. Ponce, F.A. and D.P. Bour, *nitride-based semiconductors for blue and green light-emitting devices.* Nature, 1997. **386**(6623): p. 351-359.

12. Ponce, F.A., *et al.*, eds. *III-V Nitrides.* Materials Research Society Symosium Proceedings. Vol. 449. 1997, Materials Research Society: Pittsburg.

13. Morkoc, H., *et al.*, *Large-Band-Gap Sic, Iii-V Nitride, and Ii-Vi Znse-Based Semiconductor-Device Technologies.* Journal of Applied Physics, 1994. **76**: p. 1363.

14. Morkoc, H. and S.N. Mohammad, *High-Luminosity Blue and Blue-Green Gallium Nitride Light- Emitting-Diodes.* Science, 1995. **267**: p. 51.

15. O'Donnell, K.P., R.W. Martin, and P.G. Middleton, *Origin of luminescence from InGaN Diodes.* Physical Rev. Lett, 1999. **82**(1): p. 237.

16. Nordgren, J., *Soft X-ray Emission.* Journal of Electron Spectroscopy and Related Phenomena, 2000. **110-111**.

17. Nordgren, J., *et al.*, *Soft-X-Ray Emission-Spectroscopy Using Monochromatized Synchrotron Radiation.* Review of Scientific Instruments, 1989. **60**(7): p. 1690-1696.

18. Lambrecht, W.R.L., *et al.*, *X-ray photoelectron spectroscopy and theory of the valence band and semicore Ga 3d states in GaN.* Phys. Rev. B, 1994. **50**(14155).

19. Albanesi, E.A., W.R.L. Lambrecht, and B. Segall, *Electronic structure and equilibrium properties of AlGaN alloys.* Physical Review B, 1993. **48**: p. 17841.

20. Wright, A.F. and J.S. Nelson, *Bowing parameters for zinc-blende AlGaN and InGaN.* Appl. Phys. Lett., 1995. **66**(22): p. 3051.

21. McCluskey, M.D., *et al.*, *Large band gap bowing of InGaN.* Appl. Phys. Lett, 1998. **72**(21): p. 2725.

22. Kalashnikov, E.V. and V.I. Nikolaev, *Temperature-Composition Dependence of the Bandgap and Possible Non-Planar Structures in GaN-AlN, GaN-InN and-AlN Mixed Crystal.* MRS Internet Journal of Nitride Semiconductor Research, 1997. **2**(3).

23. Lawniczak-Jablonska, K., *et al.*, *Anisotropy of the nitrogen conduction states in the group III nitrides studied by polarized x-ray absorption.* Applied Physics Letters, 1997. **70**: p. 2711.

24. Katsikini, M., E.C. Paloura, and T.D. Moustakas, *Application of near-edge X-ray absorption fine structure for the identification of hexagonal and cubic polytypes in epitaxial GaN.* Applied Physics Letters, 1996. **69**(27): p. 4206-8.

25. Katsikini, M., *et al.*, *N K-edge X-ray-absorption study of heteroepitaxial GaN films.* Physical Review B (Condensed Matter), 1997. **56**(20): p. 13380-6.

26. Moustakas, T.D., J.I. Pankove, and Y. Hamakawa, *Wide Band Semiconductors*. MRS Symp. Proc. 242. 1992.

27. Ho, I.H. and G.B. Stringfellow, *Compositional modulation and ordering in semiconductors.* MRS Proc., 1997. **449**: p. 871.

28. Osamura, K., *et al.*, *Fundamental absorption edge in GaN, InN and their alloys.* Solid State Communications, 1972. **11**(5): p. 617-21.

29. Lester, S.D., *et al.*, *High Dislocation Densities in high efficiency GaN-based light emitting diodes.* Appl. Phys. Lett., 1995. **66**: p. 1249.

30. Narukawa, Y., *et al.*, *Role of self-formed InGaN quantum dots for exciton localization in the purple laser diode emitting at 420nm.* Appl. Phys. Lett., 1996. **70**: p. 981-983.

31. Canham, L.T., *Silicon quantum wire array fabrication by electrochemical and chemical dissolution of wafers.* Appl. Phys. Lett., 1990. **57**(57): p. 1046.

Chapter 6

6.1 : Principle Results

The principle scientific outcomes emerging from this thesis are:

1. Core level photoemission studies of the deposition of transition metals on the sulphur terminated InP(100) surface reveal the complex nature of interface formation. The results called into question the conventional interpretation of equating Fermi level shifts with surface electronic passivation
2. ARP studies were used to identify and characterise surface electronic states of clean GaN. Several states not previously seen are presented. The work has lead to improved surface preparation procedures necessary to produce a highly ordered surface attributed by surface state dispersion.
3. XES, XAS reports studied the bulk electronic structure of the ternary alloy InGaN. These bulk sensitive probes were used to investigate the band gap evolution as a function of indium content. The first evidence of In 4d-N 2p hybridisation within this material is also presented.

6.2 : Final thoughts

The core level photoemission study of Mn and Fe deposition on S-terminated InP(100), revealed a better understanding of the difficulties associated with growing abrupt interface devices to III-V(100) surfaces. Although improved Fe overlayer growth on S terminated GaAs was reported by Anderson et al [1, 2], the aim of those studies was to grow a relatively thick metal overlayer where the Fe would display its bulk magnetic characteristics rather than looking at ultra-thin layers. The S termination may be the reason for the improved growth but this does not indicate an abrupt interface or directly show the suppression of Fe-As interaction as suggested by Anderson et al [1, 2]. Chapter 3 takes a

closer look at a similar interface, with a much smaller overlayer thickness. One would expect in a similar manner, a suppression of Fe-P interaction, but there was evidence of a high level of chemical interaction between both Mn and Fe with the InP substrate. With increased overlayer thickness there may be other effects from S termination of the surface which helps to promote epitaxial growth, but it does not help in forming an abrupt interface. The chemical interactions across the interface dictate the electronic properties and any electronic passivation resulting from sulphur termination is subsequently lost. It is apparent that the Fe overlayer in the work of Anderson et al [1, 2] acquired bulk magnetic characteristics at a lower Fe coverage than would be the case without the sulphur termination. Further analysis of thicker overlayers may contribute to a better understanding of this phenomena.

Chapter 4 was a continuation of work investigating the electronic structure of wide band gap materials. Because of the surface sensitive nature of photoemission, one of the primary concerns was the preparation of clean surfaces. The surface electronic structure of both MOCVD and MBE grown samples was investigated. Several discrete surface states were identified and characterised. Of these, the most interesting feature found was on an MBE grown p-GaN sample. This surface state clearly dispersed into the bulk band gap, with the potential of acting as an optical recombination centre, and it is suggested that it originates from Ga adlayer bonding. Angle resolved inverse photoemission experiments on MBE grown n-GaN samples [3] performed in conjunction with ARP experiments by Dhesi et al [4] revealed no surface detail in the unoccupied conduction band with similarly prepared samples. I believe further inverse photoemission studies investigating the unoccupied conduction band surface features of samples prepared with the improved preparation procedures and higher quality samples may clarify many outstanding issues regarding the electronic structure of these surfaces.

The disparity between the surface electronic structure of MBE and MOCVD grown

samples indicates very different residual surface structures. This may indicate a different sample polarity, as apart from the surface state dispersion the remaining spectral features were very similar. Even though the bulk symmetry lines were not mapped, it is believed that the bulk electronic structures were similar for the different growth methods and doping types. A consistency was found with the MBE grown samples, particularly through the evidence of the non-dispersing surface feature, state B, as indicated on the MBE grown p-type GaN sample which was also reported by Dhesi et al [4] on MBE n-GaN samples.

During the course of these studies investigations of more complicated nitride systems were carried out, however, the surface preparation procedures for alloys such as the InGaN ternary alloy need to be improved before high quality photoemission based studies of the electronic structure will be successful. Photoemission electron microscopy (PEEM) experiments were carried out in an attempt to investigate different in-situ surface preparation techniques [5]. The results of these studies are encouraging and indicate that angle resolved photoemission investigations of these surfaces may yield more significant results.

The primary advantage of characterising these materials by soft x-ray emission and absorption studies are that being bulk sensitive probes they do not demand the same surface conditions as photoemission. Chapter 5 presented an investigation of the bulk electronic structure of the ternary alloy InGaN. The results showed that there is quite a difference between the band evolution through the AlGaN series and the InGaN series. The valence band edge indicated a linear shift with respect to Al content with no indication of movement of the conduction band edge. In contrast, the InGaN series displayed almost no movement of the valence band edge and considerable movement of the conduction band. The primary reason for the discrepancy is believed to be the large lattice mismatch between the alloys, 2.4% for GaN/AlN and 10.6% for GaN/InN [6].

The highly successful application of InGaN as the optically active layer in multi

quantum well laser diodes is considered to be as a result of the self assembly of quantum dots of InN rich regions [7, 8]. Nakamura makes reference to the concept of nanostructure self assembly growth which has been introduced as far back as 1985 with the growth of InAs on GaAs [9], where the InAs forms As rich quantum dots depending on the growth parameters. But, the In content of these InGaN optically active layers is lower than any of the samples used in this study, indicating that phase separation is unlikely. The concept of alloy disorder which inevitably leads to complete phase separation may however be a factor. Nakamura [7] also considers the idea that if an overlayer system develops a periodicity perhaps originating from the alloy disorder, growing a thin buffer layer on this, followed by a second layer, the periodicity of the second layer may improve over the first. And in the form of multi-quantum well structures, this may be repeated several times. Nakamuras' [7] laser diode design has a similar system of many alternating layers of InGaN with different In/Ga ratios, one of which may act as a buffer layer to the next promoting the periodicity of the quantum dots.

The future of nitrides is most definitely device oriented, there are many potential devices other than LEDs and laser diodes, such as UV detectors, solar cells, FETs and high electron mobility transistors (HEMT). The engineering process of trial and error at the moment far outstrips the scientific understanding of the physical processes involved, but there will be physical limits which will require a more comprehensive understanding to overcome them. From a growth perspective, crystal quality improvements will happen by either developments in conventional techniques or by more novel methods such as pulsed laser deposition which may offer the ability to grow more complex and possibly higher quality devices.

From a scientific point of view, so many complex devices often utilizing intricate physical phenomena offers the scientific community an array of opportunities to investigate and understand these physical processes which would otherwise not be available.

6.3 : References

1. Anderson, G.W., *et al.*, *Epitaxial Growth of Fe on Sulphur -Passivated GaAs(100) a method for preventing As interdiffusion.* Surface Science, 1995. **346**: p. 145.
2. Anderson, G.W., M.C. Hanf, and P.R. Norton, *Growth and Magnetic Properties of Epitaxial Fe (100) on S-Passivated GaAs (100).* Phys. Rev. Lett., 1995. **74**(14): p. 2764.
3. Valla, T., *et al.*, *Unoccupied band structure of wurtzite GaN(0001).* Physical Review B-Condensed Matter, 1999. **59**(7): p. 5003-5007.
4. Dhesi, S.S., *et al.*, *Surface and Bulk Electronic Structure of Thin Film Wurtzite GaN.* Physical Review B, 1997. **56**: p. 10271 - 10275.
5. Downes, J.E., *Private Communication*, . 2001.
6. Ponce, F.A., *Structural defects and performance of the III-V nitrides*, in *Group III Nitride semiconductor compounds*, B. Gil, Editor. 1998, Oxford Science Publications.
7. Nakamura, S. and G. Fasol, *The Blue LED*. 1997, Berlin-Heidelberg: Springer.
8. O'Donnell, K.P., R.W. Martin, and P.G. Middleton, *Origin of luminescence from InGaN Diodes.* Physical Rev. Lett, 1999. **82**(1): p. 237.
9. Goldstein, L., *et al.*, *Growth by molecular beam epitaxy and characterization of InAs/GaAs strained-layer superlattices.* Appl. Phys. Lett., 1985. **47**(10): p. 1099.

Appendix A : Grating Physics

Both the beamline and the x-ray emission spectrometer gratings have the same function, that of monochromating incoming photons. The basic physical concepts are introduced here.

A.1 : Rowland Optics

H. A. Rowland [1, 2] introduced the concept of combining a diffraction grating and the focusing ability of a concave spherical mirror. A typical Rowland 'mounting' of a concave spherical grating is illustrated in figure A.1 [3]. The Rowland circle is described by a circle normal to the grooves containing the normal to the grating and the centre of the grating and has a diameter which is equal to grating radius of curvature. The image of a point like source situated on the circle reflected from the grating will form on the same circle.

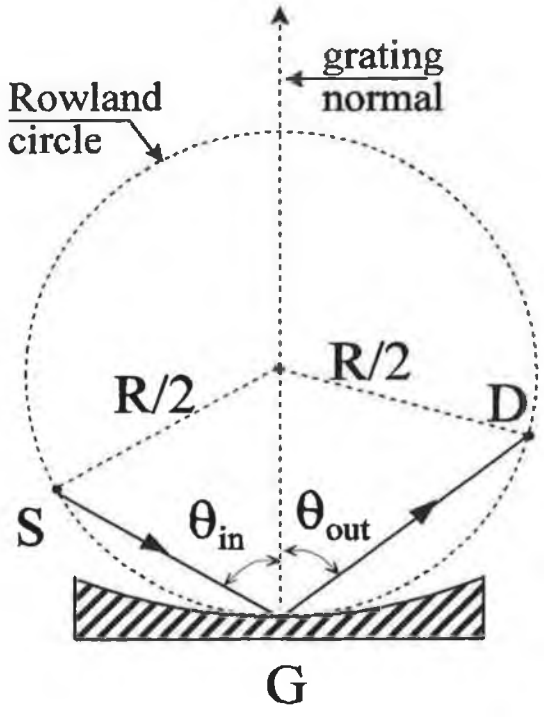

Figure A.1 : Illustrates the basic Rowland circle geometry of a concave spherical grating. The circle plane is normal to the grooves of the grating, containing the centre of the spherical grating surface (G) and the normal of the grating through G. The light source (entrance slit, S) and the image formed on the detector, D, are all on the Rowland circle.

A.2 : Dispersion

The image of the entrance slit will form on the Rowland circle where the angle of reflection equals the angle of incidence, $\theta in = \theta out$. The grating diffraction equation for a concave spherical grating is given as [3]:

$$(1) \qquad \pm m\lambda = d_0(\sin\theta_{in} + \sin\theta_{out}),$$

where θin is the angle formed by the slit image on the grating with respect to the grating normal (angle of incidence), 'm' is the order of diffraction and d_0 is the groove separation. From figure A.2, the angular dispersion of the grating can be found from the diffraction equation[3]:

$$(2) \qquad \frac{d\theta_o}{d\lambda} = \frac{m}{d_o \cos\theta_o}$$

The linear dispersion dx/dy, expressing the angle $\Delta\theta_0$, describing the linear displacement Δx along the Rowland circle. The reciprocal of which actually measures the number of angstroms per mm dispersion along the Rowland circle which is called the plate factor. From figure A.2, the plate factor may be expressed as [3]:

$$(3) \qquad \frac{d\lambda}{dx} = \frac{\cos\theta_o}{mR\left(1/d_o\right)} x10^4 \qquad \text{Å/mm}$$

A.3 : Resolution

The resolution of a spherical concave grating spectrometer is primarily defined by both the width of the entrance slit and the area illuminated on the grating surface, which are interdependent.

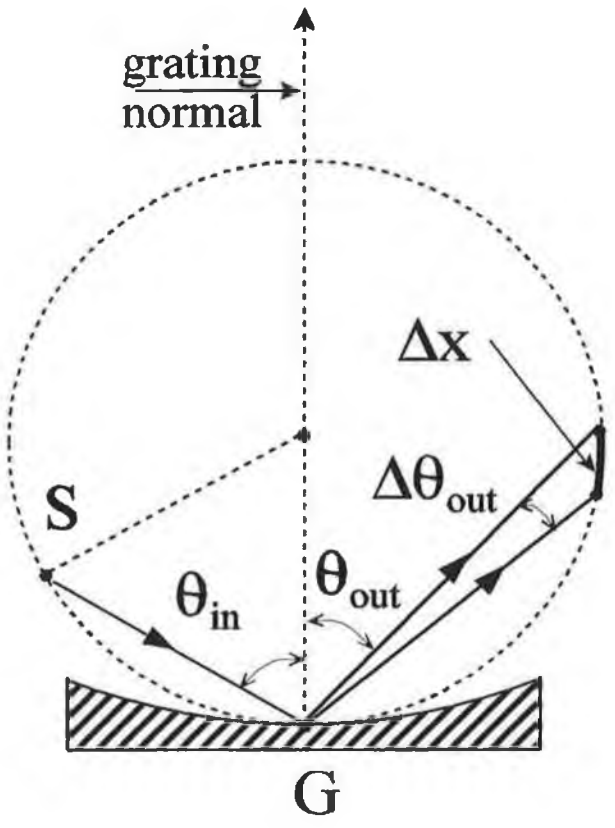

Figure A.2 : Diffracted light from two slightly different wavelengths ($\lambda + \Delta\lambda$) focused at two points separated by an angle ($\Delta\theta_{out}$). The linear separation along the Rowland circle is Δx.

The finite slit width 'w' affects the resolving power two ways. First, the images of the two beams from both edges of the slit will be separated by (4) $\Delta x = w/\cos\theta_0$ on the detector. An expression for the dispersion due to this geometrical separation is derived by using equation (3).

$$(5) \qquad \nabla\lambda_{slit}^{geom} = \frac{w}{\cos\theta_0}\left(\frac{d\lambda}{dx}\right) = \frac{wd_o}{Rm}$$

The slit width also forms a diffraction pattern which gives an additional term to the resolving power.[4]The net result for the slit resolving power is:

$$(6) \qquad R_{slit} = \frac{\lambda\left[\mathring{A}\right]}{\Delta\lambda\left[\mathring{A}\right]} = 0.91\frac{mR[m]\left(\frac{1}{d_o}\right)\left[mm^{-1}\right]\lambda\left[\mathring{A}\right]}{w[\mu m]}$$

For the grating illumination resolution effect, we note that the resolving power for a plane grating is (7) $R_{(plane)} = mN$, where N is the number of illuminated grooves, which depends on the width of illumination. For a concave grating operated at grazing incidence, taking into account image aberrations, it is found that the resolving power does not increase linearly with the increase in illumination width but has a maximum at specific illumination width [4]. The grating resolution is the lower of either the slit width or the width of illumination resolution limits.

A.4 : Refences

1. Rowland, H.A., *On concave gratings for optical purposes.* Phil. Mag., 1882. **16**: p. 197 and 210.
2. Rowland, H.A., *Preliminary nature of the results accomplished in the manufacture and theory of gratings for optical purposes.* Phil. Mag., 1882. **13**: p. 469.
3. R.Samson, J.A., *Techniques of Vacuum Ultraviolet.* 1980: Pied Publications.
4. Stagarescu, C.B., *Soft X-ray Emission and Absorption Studies of Semiconductors and Organic Molecular Solids*, in *Physics Department*. 1999, Boston University: Boston.

List of Publications and Conference Proceedings

Publications :

(1) Philip Ryan, Y.C. Chao, James E. Downes, Cormac McGuinness, Kevin E. Smith, Anand V. Sampath, Theodore D. Moustakes, *"Surface electronic structure of p-type GaN (0001)"*,Surface Science Letters, 467, (2000) L827-L833

(2) Y.C. Chao, C. B. Stagarescu, J. E. Downes, P. Ryan, K.E. Smith, D. Doppalapudi, R. Singh, T.D. Moustakas. *"Highly dispersive surface states on thin film wurtzite GaN"*, Physical Review B, 59, 24, R15586.

(3) Hughes G.J., Ryan P., Quinn P., Cafolla, A.A. *"Core-level photoemission study of the deposition of thin manganese layers on sulphur-terminated InP(100) surfaces"* , Surface Science, Volume: 431, Issue: 1-3,July 1, 1999, pp. 1-7.

(4) Hughes G.J., Ryan P., Cafolla A.A., Quinn P., *"Core level photoemission study of the deposition of thin iron layers on sulphur terminated InP(100) surfaces"*, Applied Surface Science, Volume: 147, Issue: 1-4, May, 1999, pp. 201-206.

(5) Hughes G.J. Ryan P. Quinn P., Cafolla A.A,. *"The deposition of transition metal layers on sulphur-terminated InP(100) surfaces studies by core level photoemission spectroscopy"*, Vacuum, Volume: 57, Issue: 2, May, 2000, pp. 131-138.

(6) J. Roche, P. Ryan, G. Hughes. *"Core level photoemission of sulphur terminated Si (110)"* Surface Science,465 (2000), 115-119.

(7) J. Roche, P. Ryan, G. Hughes. *"Core level photoemission of sulphur terminated Ge (110)"* Accepted for publication, Surface Science, 2001.

Conferences :

(1) American Physical Society, March Meeting, Seattle, 2001, contributed talk.

(2) Materials Research Society, Fall Meeting, Boston, MA, 2000, poster.

(3) National Synchrotron Light Source, Annual Users Meeting, Upton, NY, '99, '00.

Presentation given at APS, Argonne National Lab, Chicago, 2000.